THESIS FOR THE DEGREE OF DOCTOR OF PHILOSOPHY

Additive manufacturing and joints:

Design and methods

by

Mattia Frascio

UNIVERSITÀ DEGLI STUDI
DI GENOVA

Supervisor:

Massimiliano Avalle

Co-supervisor:

Lucas Filipe Martins da Silva

February 2021

Abstract

The industrialization of the Additive Manufacturing (AM) processes is enabling the use of AM components as final product in several applications. These processes are particularly relevant for manufacturing components with optimized custom-tailored geometries. However, to fully exploit the potentiality of AM, the development of knowledge aimed to produce dedicated design methods is needed. Indeed, even if AM enables the manufacturing of new kinds of structures, e.g. 3D lattice structures, it introduces process-specific design input and limitations that needs design methods different to from the ones for subtractive manufacturing.

Design for AM (DfAM) is a design methodology that aims to take advantage of new buildable geometries but taking into account also AM processed materials anisotropy and 3D printing constraints.

Recent literature focused on the assembly of AM components and on the AM components joining to a main structure. The conclusion was that adhesive bonding is a promising joining process, especially considering its improved stress distribution compared to fastening, but at the time of writing a method that combines DfAM and adhesive bonding knowledge is not available.

The work presented in this thesis focused on developing knowledge on design for AM and bonded joints. First step was evaluating testing methods for AM and producing data on materials properties.

Secondly, the early works on tailoring approaches for AM joints, published recently in scientific literature, were analyzed. Then AM dedicated designs, modifications and testing methods were proposed both for the adherends (in the thickness and on the surfaces) and the joints. Specifically, an innovative joint design concept was introduced, i.e. using the 3D printing parameters as bonded joint design factors.

Eventually, feasibility of performing joints using multi-material AM with conductive polymer to embed heating elements was assessed. The 3D printed through the thickness circuits is a cutting-edge approach to enable new solutions for joints structural monitoring and self-healing.

List of Acronyms

1D	One dimensional
2D	Two dimensional
3D	Three-dimensional
ABS	Acrylonitrile Butadiene Styrene
AM	Additive Manufacturing
ANOVA	Analysis of Variance
APP	Atmospheric Pressure Plasma
ASA	Acrylonitrile styrene acrylate
ASTM	American Society for Testing and Materials
BJ	Binder Jetting
CATT	Centrifugal Adhesion Testing Technology
CFRP	Carbon Fiber-Reinforced Polymer
CLIP	Continuous Liquid Interface Production
CLSM	Confocal Laser Scanning Microscopy
CZM	Cohesive zone model
CT	Computed Tomography
DC	Direct Current
DCB	Double Cantilever Beam
DED	Direct Energy Deposition
DfAM	Design for Additive Manufacturing
DIC	Digital Image Correlation
DIN	Deutsches Institut für Normung
DM	Digital Material
DoE	Design of Experiment
DOF	Degrees Of Freedom
ENF	End-Notched Flexure

FDM	Fused Deposition Modeling
FEA	Finite element analysis
FEM	Finite Element Method
FFF	Fused Filament Fabrication
FGA	Functionally Graded Adhesive
FGAM	Functionally Graded Additive Manufacturing
FGM	Functionally Graded Material
FPZ	Fracture process zone
ISO	International Organization for Standardization
LDM	Liquid Deposit Modeling
LOM	Laminated Object Manufacturing
LPP	Low Pressure Plasma
MJ	Material Jetting
MMAM	Multi Material Additive Manufacturing
OA	Orthogonal Array
NIST	National Institute of Standards and Technology
PA	Polyamide
PC	Polycarbonate
PEI	Polyetherimide
PEEK	Polyether ether ketone
PLA	Polylactic Acid
PTFE	Polytetrafluoroethylene
SEM	Scanning Electron Microscope
SiC	Silicon Carbide
SLA	Photopolymerization
SLJ	Single lap joint
SLM	Selective Laser Melting

STL	Stereolithography
UV	Ultraviolet light
VCCT	Virtual Crack Closure Technique
XPS	X-ray photoelectron spectroscopy

List of Notations

Δa	Crack opening along the load line
δ	Point-load displacement
σ_a	Average stress
τ_{ave}	Average shear strength
Θ	Contact angle
A+	Edgewise stacking direction, notch on top layers
A-	Edgewise stacking direction, notch in bottom layers
A_0	Overlap area
a	Crack length
AC	Alternating Current
a_e	Equivalent crack length
B	Flatwise stacking direction
C	Adherends compliance
E11	Young 'Modulus obtained with single lamina dogbone, material deposition 0°
E22	Young 'Modulus obtained with single lamina dogbone, material deposition 90°
E45	Young 'Modulus obtained with single lamina dogbone, material deposition 45°
E_f	Flexural modulus
e_f	Strain at failure
F_{MAX}	Maximum load recorded prior to failure
G12	Shear Modulus
G_I	Strain energy release rate
G_{Ic}	Fracture Toughness
H	Layer height
h	Adherend height
Ls	Span length
P	Load

PWM	Pulse-Width Modulation
R	Stress ratio
Ra	Surface roughness
Rm	Average ultimate tensile strength
Sa	Average (2D) Surface roughness
Ssk	Surface skewness
S_{ut}	Ultimate stress
T	Temperature
v_c	Volumetric percentage
V	Speed
±V	Voltage

x

Contents

Introduction

Introduction

The industry is currently adopting AM processes to manufacture highly optimized components, where the designer can exploit the AM enabled complex geometries to embed the component functionalities in the shape.
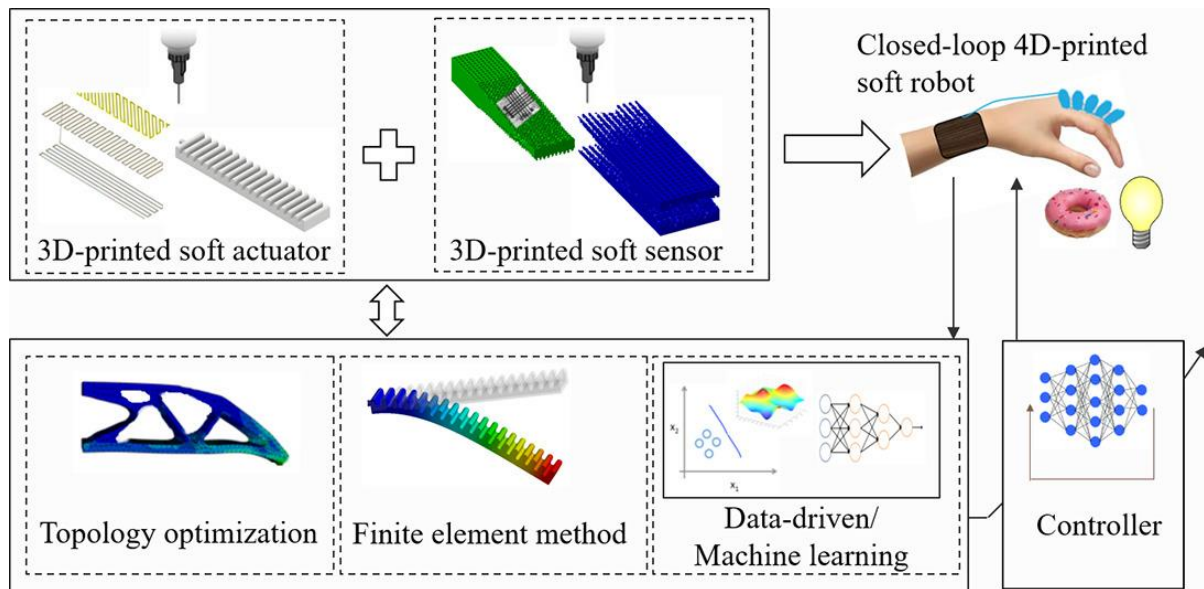
Figure 1: Example of DfAM applied to a robotic end effector with embedded 3D printed sensors, from [1].

Relevant applications can be found in robotic field, e.g. AM is used to realize the end effector for collaborative robot (Figure 1) [1,2], in automotive and in aerospace fields in the search of structural weight reduction or crashworthiness improvement and medical field, e.g. patient-specific orthosis or customized remote health monitoring devices (Figure 2) [3–5].

Figure 2: On the left, 3d printed patient specific orthosis, from [4]. On the right, sensorized 3D printed glassed for neurodegenerative diseases monitoring, from [5].

Recently, the interest in the adhesive bonding solutions for the assembly of the AM components themselves, or for the optimized AM components on a main structure, is increasing because it offers several advantages with respect to other joining solutions. However, the prediction of the behaviour of these structures is not trivial and represent a challenge for the engineers.

Regarding the adhesive bonding, the joints design with polymeric adherends under several working conditions, like humidity or fatigue, were investigated by researchers for the automotive industry [6] and adhesive behaviour can be reasonably well understood. However, the peculiar material structures generated by the AM processes introduce new design variables that have to be taken in account (Figure 3).
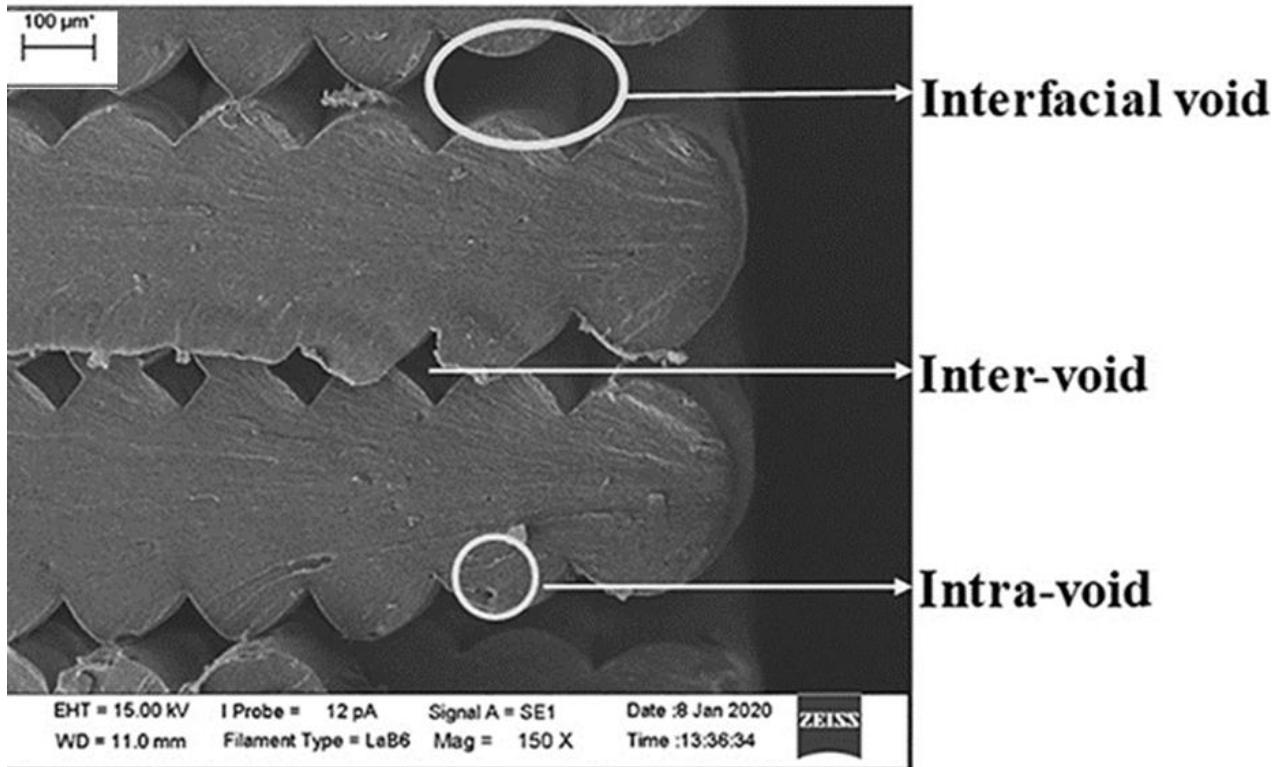
Figure 3: Example of AM typical microstructure and defects due to the material stacking, from [7].

One of the main goals of this work is, therefore, also to provide experimental data and dedicated testing approaches for the AM adherends characterization.

Another aspect of great importance is the focus on Design for Additive Manufacturing (DfAM) to develop highly advanced joints designs and joining techniques that take advantage of AM processes, new AM materials and local control on the material properties. Optimized multi-material AM components, designed to take advantage of the AM tailored material structures, can outperform the components designed according to the current at time of writing best practice knowledge. AM improved adhesive bonding technique can be an integral paradigm shift serving as a tool to faster innovation.

This work focused on developing knowledge on design for AM and bonded joints by creating a cooperation between four host institutions (main: UNIGE, FEUP and secondary: UNIPR, UNICAL, Figure 4).

Figure 4: Representation of the local of the institutions involved.

Objectives

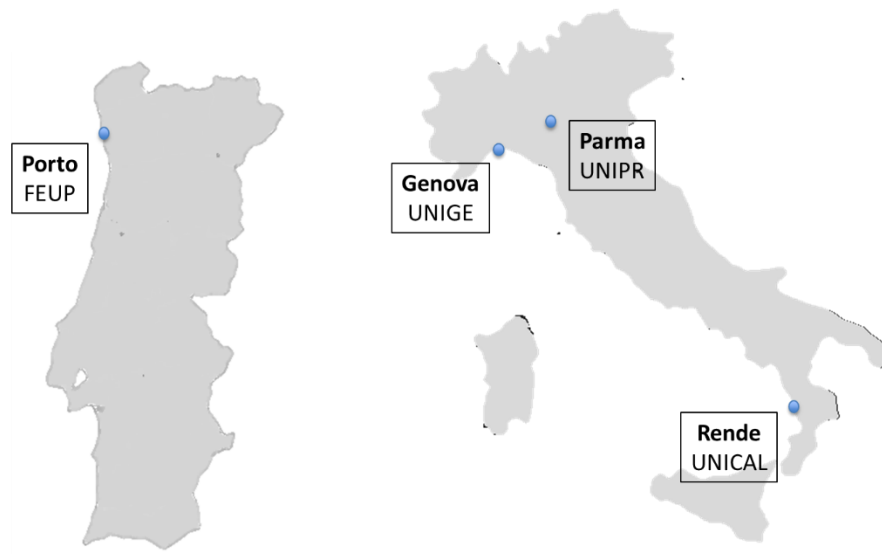The main objective of this thesis is to contribute to the knowledge on the design for additive manufacturing and, in particular, on the joining processes. A defined methodology for this purpose does not currently exist at time of writing. A validated procedure will enable the manufacturing of optimized components with improved stress distribution and durability without constraints on the placement for printability. It is worth noting that the placement is of great importance processing reinforced materials and performing 3D print using multiple materials at the same time. Advancing in the knowledge on the joining processed is relevant for the industrial production using AM also related to the building volumes. By splitting a big component in sub-components it is possible to divide the production in several smaller 3D printers (3D printer farms) with benefit on overall built time and production-stops safety compared to using a single bigger 3D printer (Figure 5).
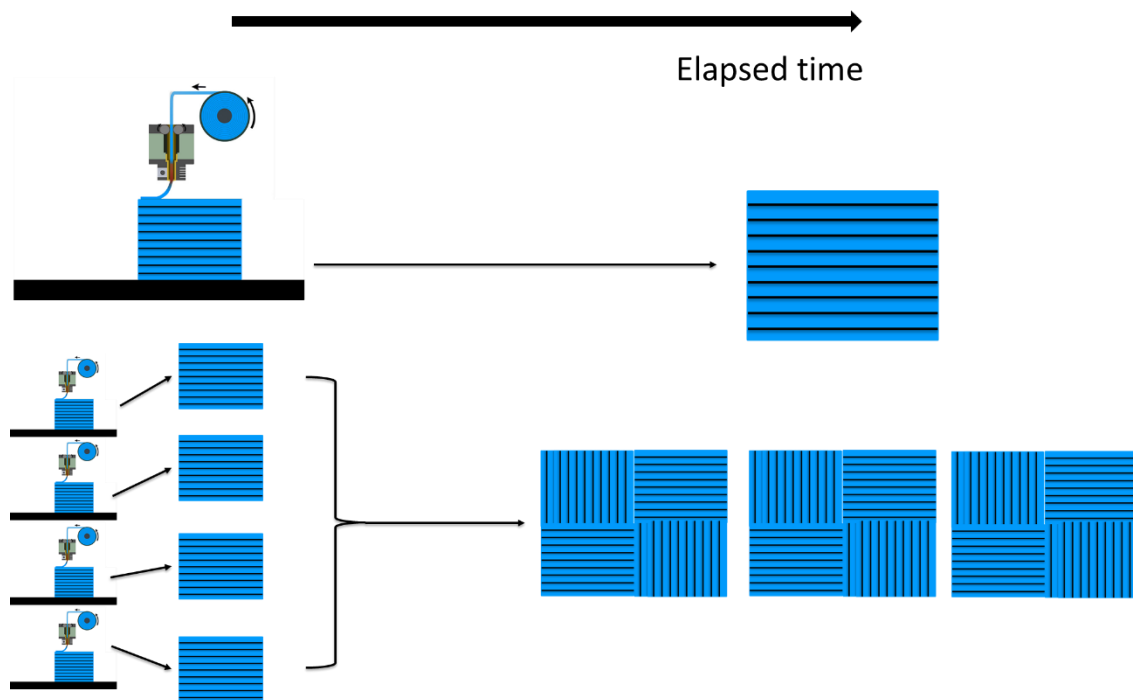
Figure 5: Schematic of the benefits of 3D printer farms for components production The productivity of many smaller 3D printers is generally higher than a single larger machine. Parts can be 3D printed with material stacking directions optimized with respect to service loading.

Another relevant challenge of the design for additive manufacturing applied to joining is the aim of obtaining components ready to be assembled from the manufacturing process, reducing the need to perform costly secondary machining and surface preparations. While avoiding secondary machining is

relatively straightforward carefully adding dedicated features modelling the geometries, surface preparations could be avoided using the 3D printing parameters to affect the surface properties, adding a new concept to the DfAM.

Lastly, the work will explore the feasibility of innovative joining methods for AM, based on the combination of multi-material process and new commercially available materials. Conductive polymers indeed allow to 3D print embedded circuits that can be used to cure the adhesives or to obtain welding through joule heating.

Research methodology

To address the challenges presented in the previous sections, several tasks were defined to improve the current knowledge on joints designed for AM components. A representation of the research methodology adopted in this work is shown in the schematic in Figure 6.
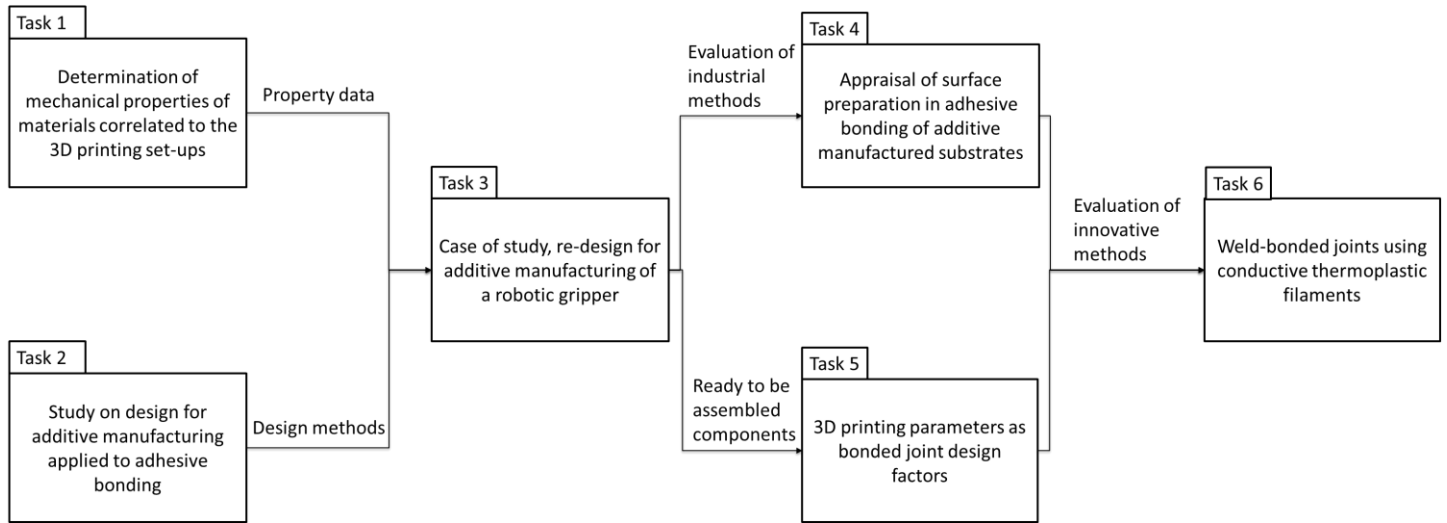
Figure 6: Schematic representation of the workflow of this work.

A detailed description of each task is performed subsequently.

Task 1 - Determination of mechanical properties of materials correlated to the 3D printing set-ups

The objective of this task was to determine which existing standardized testing methods can be applied to characterize polymeric AM processed materials. The aim is to obtain relevant data for the design of AM components, data which are representative also of the typical anisotropy of these manufacts. Experiments were carried out on ABS, a polymer used often for AM components both in bulk and reinforced compound. Plane-bending fatigue testing procedure that uses miniaturized polymeric specimens was proposed and used to produce original data on the anisotropic fatigue behavior of ABS AM processed. The miniaturization of the specimens eases the multiple specimen production, especially characterizing multiple build direction.

Milestone 1: Collection on information on testing methods to define the validated methods to characterize the AM materials, production and collection of the relevant data for the DfAM.

Task 2 - Study on design for additive manufacturing applied to adhesive bonding

The objective of this task was to collect, synthetize and catalog the different joining design approaches investigated for AM in the recent scientific literature. Aim was to produce useful information to establish a starting point for the DfAM applied to the joining procedure. The design approaches to maximize joints performance were organized according to the proposed design philosophy, namely, to use the AM enabled localized control on the material properties to tailor the adherend, the adhesive or the interface in between.

Milestone 2: Production of an organized collection of the current knowledge on DfAM applied to adhesive bonding. Identification of the new design solutions enabled by the combination of the innovative materials coupled to the AM locally controlled properties.

Task 3 - Case of study, re-design for additive manufacturing of a robotic gripper

This task objective was to explore the actual potentiality of AM components. The DfAM was applied to develop an innovative robotic end effector. Through adhesive bonding, it was possible to realize a highly optimized solution with significant reduction in weight, size and components number.

Milestone 3: DfAM coupled to adhesive bonding was successfully applied to obtain an improved design of a robotic end effector.

Task 4 - Appraisal of surface preparation in adhesive bonding of additive manufactured substrates

The objective of this task was to address the lack of information on the surface modifications effective on AM adherends. Indeed, after **Task 2,** it was not possible to draw up a guideline for surface preparation of the AM adherends. Also, it was pointed out that the peculiar material morphology can play a relevant role alongside to the materials' chemical affinity for the performance of the joints. Moreover, in **Task 3** plasma treatment was necessary to switch the failure location from interface to the adherends. Several adhesives and industrial surface modifications were investigated using AM ABS adherends and single lap joints.

Milestone 4: Original information on industrial surface treatments efficacy on AM adherends coupled to several adhesives were produced.

Task 5 - 3D printing parameters as bonded joint design factors

The objective of this task was to assess the feasibility of embedded-in-the-AM-build surface modifications to obtain components ready-to-be-assembled. The activities were organized in two steps. At first full characterization of the effect of the AM process was performed using Taguchi methods. Then experiments on double cantilever beam specimens were performed using 3D printed adherends with dedicated parameters settings. Thus, it was possible to obtain the following surface conditions and material properties: minimum roughness, maximum roughness, minimum wettability, maximum wettability, minimum stiffness, maximum stiffness. At last, using dedicated data reduction, the effect of using the 3D printing parameters as bonded joint design factors was quantified by fracture toughness comparison.

Milestone 5: An innovative approach to joints design was proposed giving the foundations for a new method based on the DfAM.

Task 6 - Weld-bonded joints using conductive thermoplastic filaments

This task required a more complex experimental procedure and it can be divided into two main steps: the first was regarding a DfAM based welding process, being the second to its integration into hybrid weld-bonded joining process. Initially, a thermal characterization of the 3D printed polymeric conductive pads, heated by joule effect, was performed aiming to obtain a prediction of the behavior of the pads in the adherends thickness. After a first assessment of welding process feasibility, single lap joints design was performed based on the methods identified in **Task 2** and **Task 4**. The adherends' 3D printing parameters were carefully set according to the data obtained in **Task 5.** The performance of three different configurations were evaluated, namely bonded, welded and hybrid weld-bonded single lap joints. Materials characterization was also performed to produce data to feed the numerical models, created to achieve a better understanding of the joints' behavior.

Milestone 6: Feasibility of joining AM components using embedded 3D printed circuits was assessed and original data for joints design and joining process produced.

Chapters

This thesis consists of six chapters and an introduction, each chapter of the thesis being based on one or more papers. Special care and effort were taken to provide the readers with necessary experimental details and to avoid repetition of information from a chapter to another.

The following list details the papers used to write the chapters of this thesis:

Chapter 1: Frascio M, Avalle M, Monti M. **Fatigue strength of plastics components made in additive manufacturing: First experimental results.** *Procedia Struct. Integr.*, vol. 12, 2018, p. 32–43. DOI: 10.1016/j.prostr.2018.11.109 (Task 1).

Chapter 2: Frascio M, Marques EA de S, Carbas RJC, da Silva LFM, Monti M, Avalle M. **Review of Tailoring Methods for Joints with Additively Manufactured Adherends and Adhesives**. *Materials*, 2020; vol. 13, p. 39-49. DOI: 10.3390/ma13183949 (Task 2).

Chapter 3: Jilich M, Frascio M, Avalle M, Zoppi M. **Development of a gripper for garment handling designed for additive manufacturing.** *Proc Inst Mech Eng Part C J Mech Eng Sci,* 2019; p. 1–12. DOI: 10.1177/0954406219857763; Frascio M; Jilich M; Pizzorni M; Monti M; Avalle M; Zoppi M **The use of low-pressure plasma surface modification for bonded joints to assembly a robotic gripper designed to be additive manufactured.** *Procedia Struct. Integr.,* 2019, vol. 24, p. 204–212. DOI: 10.1016/j.prostr.2020.02.017 (Task 3, Task 4).

Chapter 4: Frascio M, Bergonzi L, Jilich M, Moroni F, Avalle M, Pirondi A, Monti M, Vettori M, **Additive manufacturing process parameter influence on mechanical strength of adhesive joints, preliminary activities.** *Acta Polytech CTU Proc.,* 2019; vol. 25, p. 41–47. DOI: 10.14311/APP.2091.25.0041; Bergonzi L, Pirondi A, Moroni F, Frascio M, Avalle M. **A study on Fused Filament Fabrication (FFF) parameters as bonded joint design factors.** *J Adhe*s., 2021, DOI 10.1080/00218464.2020.1862655 (Task 5).

Chapter 5: Frascio M, Mandolfino C, Moroni F, Jilich M, Lagazzo A, Pizzorni M, Bergonzi L, Morano C, Alfano M, Avalle M, **Appraisal of surface preparation in adhesive bonding of additive manufactured substrates**. *International Journal of Adhesion and Adhesives*, vol. 106, 2021, p. 108. DOI: 10.1016/j.ijadhadh.2020.102802 (Task 4).

Chapter 6: Frascio M, Moroni F, Marques E, Carbas R, Reis M, Monti M, Avalle M, da Silva L, **Feasibility study on hybrid weld-bonded joints using additive manufacturing and conductive thermoplastic filament.** *Journal of Advanced Joining Processes*, 2021, DOI: 10.1016/j.jajp.2021.100046 (Task 6).

Thesis background

Thesis background

Additive manufacturing is a manufacturing process able to produce components adding the material instead of subtracting it, as it happens for example during milling operations.

According to ISO/ASTM 52900:2017, AM processes can be classified according to the material deposition process. These processes are binder jetting, directed energy deposition, material extrusion, material jetting, powder bed fusion, sheet lamination and vat photo-polymerization (Figure 7).
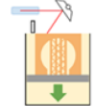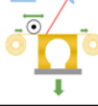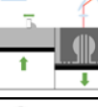
	Process	Acronyms	Feedstock	Material	Bonding and join
	Extrusion (or fused filament fabrication or fused deposition modeling)	FFF, FDM	Filament, rod, pellets	Polymer	Fused with heat
	Photopolymerization (or stereolithography)	SLA	Liquid	Photopolymer, metal, ceramics, composite	Cured with laser, projector, UV light
	Material Jetting (or Binder Jetting)	MJ (BJ)	Powder, liquid	Ceramic, wax, polymer, metal, sand	Cured with UV light, heat
	Laminated Object Manufacturing (or Sheet Lamination)	LOM	Sheet	Paper, metal, polymer	Joined with agent, heat and pressure
	Selective Laser Melting	SLM	Powder	Metal	Fused with laser and electron beam
	Directed Energy Deposition	DED, EBM	Wire, powder	Metal	Fused with laser and electron beam

Figure 7: Scheme of additive manufacturing (AM) processes, from [8].

A macro-sorting of the AM processes can be made on the processed materials, the works during the doctorate activities was carried out using polymeric materials.

A filament extrusion thermoplastic polymer-based process, the Fused Filament Fabrication (FFF), was selected for the experimental part of this work. FFF is of particular interest for the scientific community and industrial applications because able to process different materials, bulk and reinforced, at the same time, tailoring the material properties not only on a voxel design approach, but also by the filament deposition pattern.

Those process features permit to rethink the design of the components embedding the functions in the shapes and in the materials properties' gradients.

The industrialization of the AM processes is enabling in several fields the use of AM components as final product [9]. Relevant applications are, for example, robotic end-effectors designed for specific collaborative tasks [10], customized medical devices for healthcare [11], light-weighting for aerospace vehicles [12,13] or enhanced energy absorption for automotive components [14,15]. As the design for additive manufacturing and the AM component optimization are experiencing a fast improvement as well the needs of assembly methods for AM components is growing. Traditional fastening methods such as bolts, pins, nuts and screws create variable stress distributions with considerable stress concentration. Adhesive bonding can be used to solve those issues [16,17], enabling the joining of the complex geometries typically built using the AM processes. Moreover, the DfAM coupled to the current knowledge on the adhesive joining process offers opportunity of new tailoring methods to optimize the AM component-adherend, e.g. interlocked parts bonded by adhesive smearing or infiltration [18].

The aim of this section is to focus on the AM processes (Figure 8) used in conjunction with bonded joints, in an effort to identify the features and capabilities which are most relevant for joint tailoring. Readers who wish to obtain more detailed information on AM processes are referred to dedicated reference works on AM processes such as those published by Gibson et al. [19] or Ali et al. [20], that are the source of some of the information shown in the section.
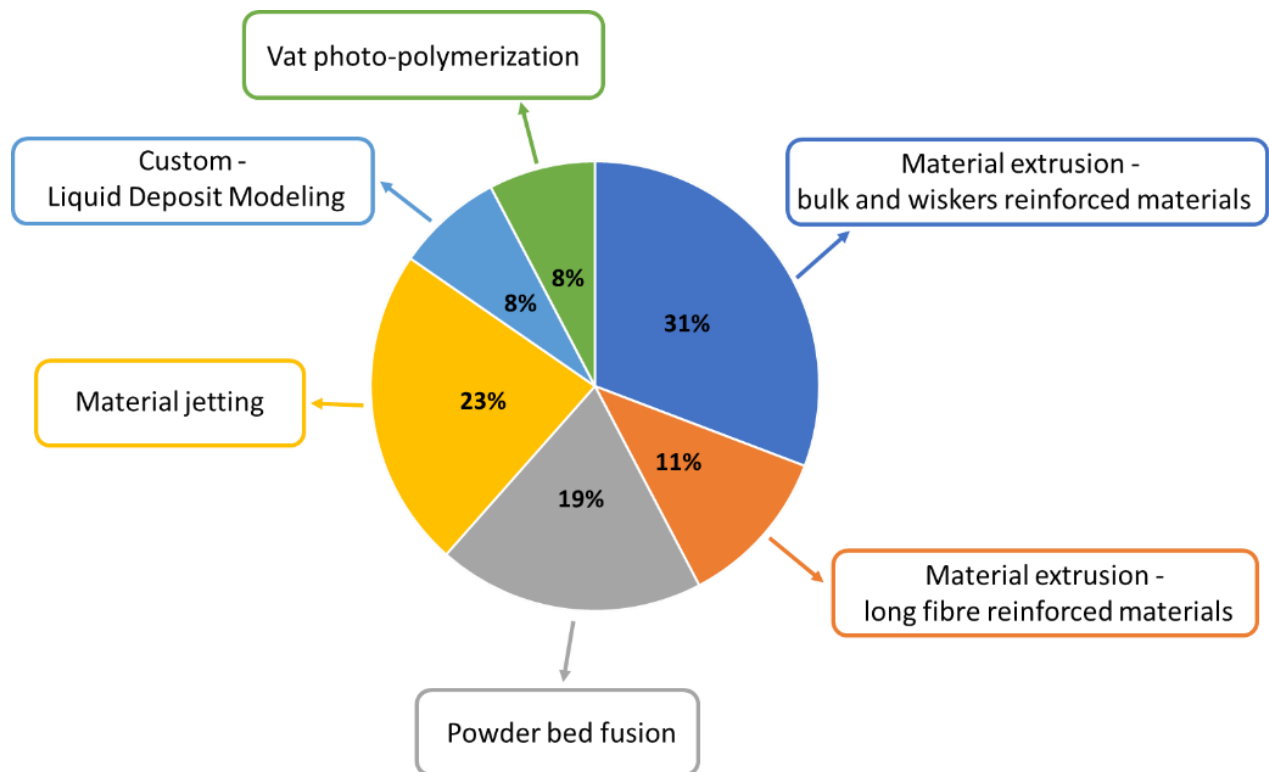
Figure 8: AM process used for AM tailoring of bonded joints (summary based on the literature analysis carried out for the thesis work).

Material extrusion processes are based on the principle of a thermoplastic filament being pushed through a heated nozzle. Geometrical features are created by deposing the material while moving the nozzle in the stacking direction and the bed in the plane orthogonal to it (Figure 9).
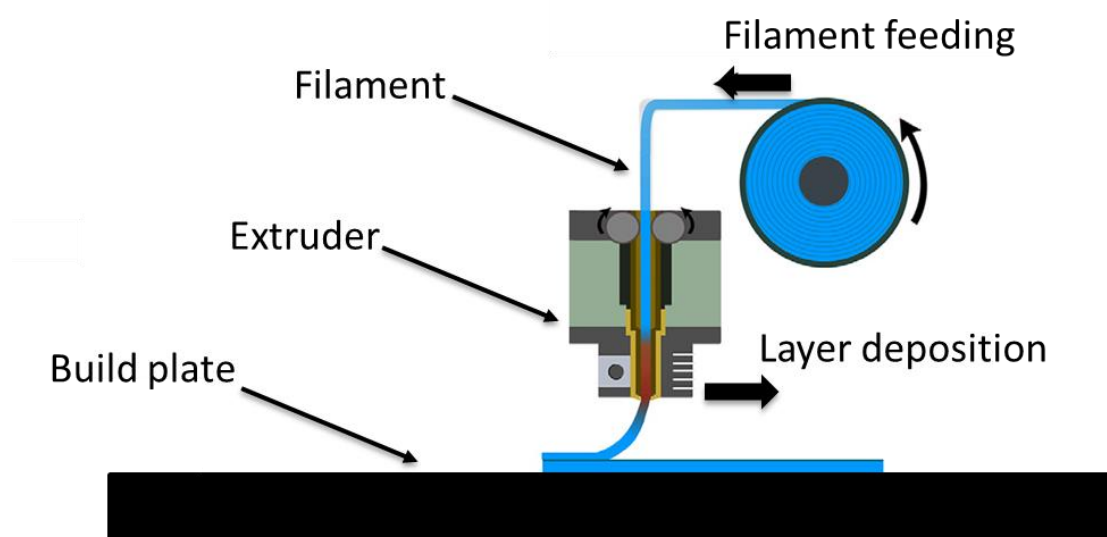
Figure 9: Schematic of material extrusion processes.

This process is one of the most widespread and two commercial configurations have been successfully used for improving the performance of bonded joints. These are the patented Stratasys (Rehovot, Israel) Fused Deposition Modelling (FDM), used by Spaggiari et al. [21], Garcia et al. [22], Bürenhaus et al [23], and the open source FFF, used by Cavalcanti et al. [24], Li et al. [25], Kovan et al. [26,27], Kariz et al. [28]. FDM has the advantage of being a process optimized for reproducibility with a closed and heated 3D printing volume, standardized printing setup and controlled materials, while FFF has the advantage of being more freely customizable for a given application. Minimum process resolution is dependent on the nozzle diameter and layer height slicing parameters. Older commercial solutions were limited to a single extruder in order to process bulk materials or short reinforced thermoplastic composites. Newer 3D printers are equipped with multiple nozzles for multi material builds.

The growing interest in using AM for industrial applications has eventually led to the development of 3D printers capable of processing long fibre reinforced thermoplastic composites. These 3D printers were used by Dugbenoo et al. [29], Garcia-Guzman et al. [30], Yap et al. [31] in their works on adhesive bonding. The authors note that this process, due to is relative novelty, is still affected by technical problems, such as porosity in the components, susceptibility to fibre pull out, component warping during manufacturing and a limited number of standardized materials available for use. Despite these drawbacks and geometrical constraints due to fibre stiffness, this is still a highly promising process as the Young's modulus of the materials can increase from around 1 GPa for bulk materials to around 30 GPa for long fibre reinforced materials. Currently, the process resolution can be as low as 6.25 µm in the layer and 100 µm in the layer stacking direction.

Authors that used material extrusion-based processes also pointed out that slicing parameters and build placement of the components can change the adherends mechanical and surface properties, leading to high performance bonded joints.

Customization of FFF 3D printer allowed the engineering of a new process, the Liquid Deposit Modeling (LDM). LDM consists in adapting the feeding system in order to extrude liquid materials. This approach was used by Schmidt et al. [32] and Sekiguchi et al. [33] to tailor the adhesive, for example to control the adhesive stiffness along the overlap coordinate. This method is novel and demonstrated to have high potential in adhesive tailoring applications, but at moment of writing it is only available as a custom designed equipment and requires the development of dedicated 3D set ups.

A polymeric powder bed fusion process was used by Morano et al.[55, 56], Alfano et al. [36], Leicht et al. [37], and Fieger et al. [38] with EOS 3D printers (Munich, Germany). This process is based on dabbed

16

powder on a build plate moving in the stacking direction and a laser that sinters the powder in the orthogonal direction to the stacking direction (Figure 10).
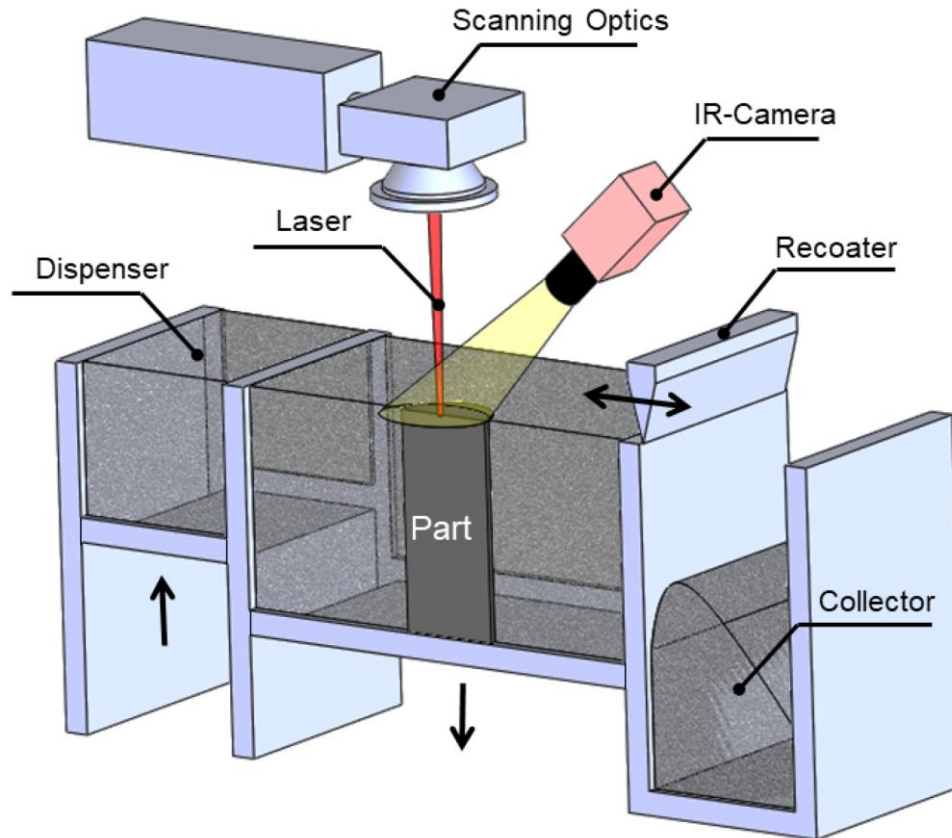
Figure 10: Schematic of powder bed fusion process principle, from [8].

One of the advantages of this process is that the non-sintered powder is a natural support allowing the manufacture of complex geometries. The main drawback is that paths for the removal of non-sintered powder must be considered in design and adds a step to the manufacture process. In addition, in the context of joining, the authors pointed out that partially sintered particles on the surface can cause joint failure due to weak adhesion of these particles to the adherend. The process resolution depends on laser scatter, z-step of the build plate and the granulometry of the polymeric powder.

Material jetting process was used by Vijayanand et al. [39], Kumar et al. [40,41], Khan et al. [63, 64] and Ubaid et al. [44]. This process is implemented with an inkjet 2D printer scheme (Figure 11).
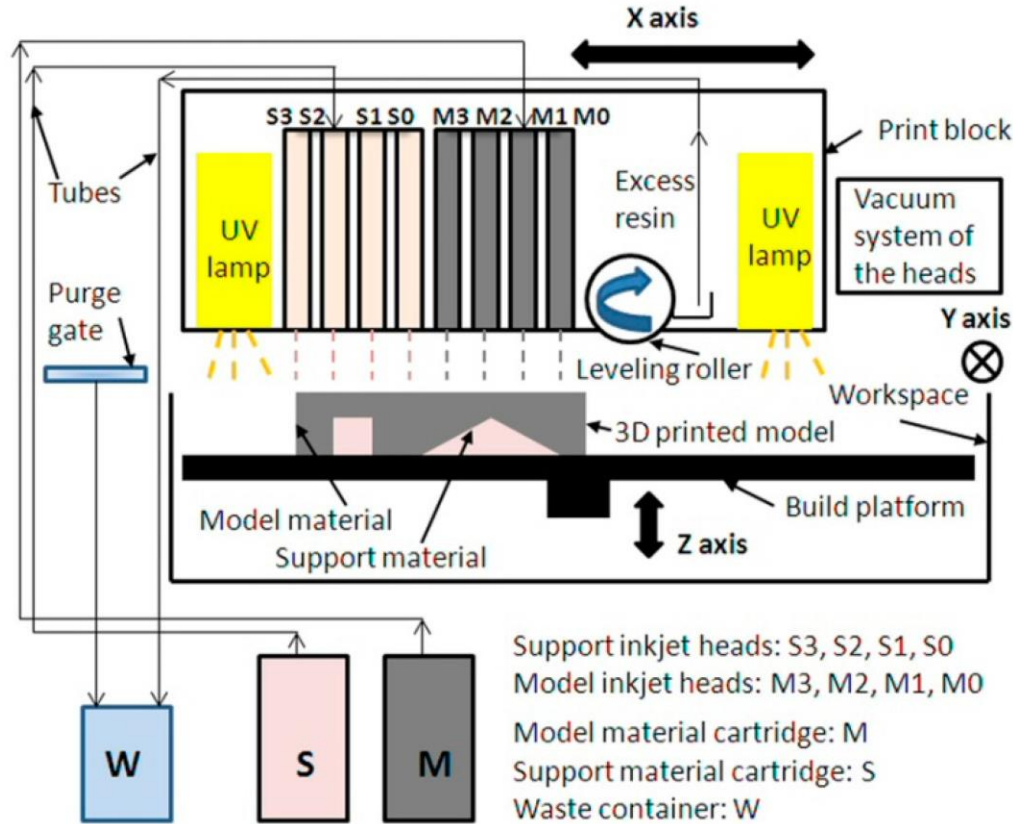
Figure 11: Example of material jetting 3d printer scheme, from [45].

Photopolymer droplets are jetted on the build plate by a moving nozzle to form a 3D shape and the polymer is then UV cured. The authors took advantage of the high process resolution, nominally 16 μm in the stacking direction and 42 μm in the orthogonal plane, and of the multi material printing capabilities, to create digital materials (DMs) [46]. These DMs are obtained by volumetric mixing of two or more photopolymer droplets at voxel size and allows a precise control over the mechanical properties. This process has a higher productivity with respect to the other processes and can manufacture components with mitigated layer effect and/or functionally graded materials (FGM). However, it is not suitable for use with reinforced materials.

Vat photo-polymerization was used by Redmann et al. [47] and Dahmen et al. [48] to manufacture joints in a two-step process. In the first step, a green part is shaped using stereolithography (STL), then in the second step the components are assembled using a thermal curing cycle. The process resolution is dependent on the viscosity of the liquid resin that affects the minimum layer height. Quality inspection demonstrated that these joints have lower porosity and higher geometrical accuracy than those manually

18

assembled, while the major limitation of the process is the limited compatibility of different materials curing cycles.

It is worth noting that neither the promising 3D printing set-ups that combine the mentioned processes with the pattern freedom of 6 DOF robotic arms [49] or the use of slicer software able to create 3D tool patterns [50] were investigated in works combining joining methods with AM.

To better understand current research trends, a study was made on the materials typically used when AM is used in conjunction to bonding (Figure 12). The nature of the materials used is an extremely relevant information because the physical properties that govern adhesion [51], for example surface energy compatibility between adherend and adhesive, are material dependent.
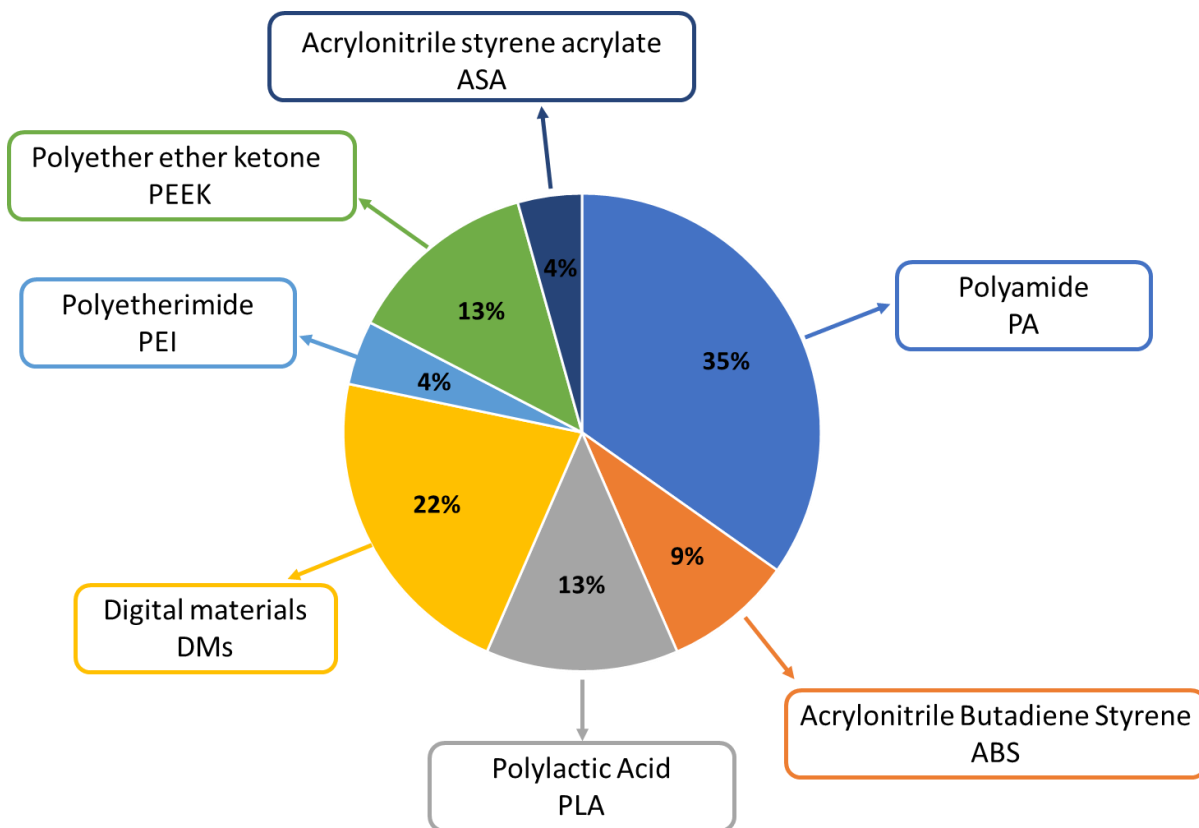
Figure 12: Materials used to build adherends with AM (summary based on the literature analysis carried out for the thesis work).

Polyamide (PA) is used as thermoplastic matrix for long fibre reinforced AM composites. It is difficult to process and suffers of water absorption problems. Polyetherimide (PEI) and Polyether Ether Ketone (PEEK) are techno-polymers and require a dedicated 3D printer. Acrylonitrile Styrene Acrylate (ASA) is

often used as Acrylonitrile Butadiene Styrene (ABS) replacement due to lower warpage, while Polylactic Acid (PLA) has a relatively low strength, but it is an inexpensive biodegradable polymer that finds extensive use in biomedical 3D printing applications.

Chapter 1

Characterization of AM processed materials

This chapter is based on paper [52] and focus on material testing approaches for additively manufactured components. Aim is to produce material data for the AM components and joints design. The focus of the work is on taking in account the anisotropy of the materials generated by the AM manufacturing processes.

1.1 Background and motivations

Additive Manufacturing is growing ever more interesting in engineering due to its advantages in freedom of design. At the same time, costs have dropped especially for low-weight low-cost materials such as plastics. In the 3D-printing of plastics, FFF has demonstrated its ability to produce polymers with performances comparable to conventional manufacturing processes [53]. So, there is an increasing interest in proposing innovative solutions in many engineering applications. However, for technical applications it is of paramount importance to be able to design the new components and to predict their performance in any possible conditions, taking into account various environmental and loading conditions, to avoid any possible premature failure. This process, almost obvious for components made of conventional materials with conventional technologies, is still not completely established in components made of innovative materials (e.g. conductive plastics) and, for different but equally obvious reasons, even less with innovative technologies like additive manufacturing. The reasons for this lack of effective design methodologies lies not only in subjective insufficient know-how of the designers in this field and, sometimes, underestimated possible criticalities if not wrong assumption on some design approach, but also in the objective deficiencies of information and data in this area.

AM is a relatively young family of production technologies having the greatest flexibility and allowing the highest complexity due to the freedom from many technical constraints of conventional methods, and also enables optimization tools to be used at full potential, a remarkable e.g. by Primo et al. [54]. Actually, this freedom and complexity at no costs are not absolute and physical limitations together with new technological constraints still stand. First of all, strength of materials still dictates dimensional constraints together with other shape requirements. The problem in evaluating the strength of additively manufactured components lies in the intrinsic inhomogeneity and discontinuity of the material, whatever the used technology: whether starting from powders or filament, the layer-by-layer construction leaves a structure with countless microscopic defects. In addition, fatigue data for AM polymers are scattered, which further makes analysis difficult due to the manufacturing defects and uncertainty in AM process.

Characterization of AM processed materials

1.2 Quasi-static testing for additive manufacturing

This section summarizes the materials and joints characterization methods employed in the published works on polymeric AM for adherends and bonded joints.

The definition and selection of adequate characterization methods is a relevant topic due to a lack of specific test standards for polymeric AM. As remarked by Dizon et al. [55] in a recent review paper on mechanical characterization of polymeric AM components, at the moment, there are still no dedicated standard test methods. There are several reasons behind this standardization deficiency. For example, the heterogeneity of polymeric AM methods, the 3D printer type and the dependence of the final component properties on the print parameters, are all major issues. In addition, it is often difficult to correlate the effect of the build parameters on the final output [56–59]. Even if these observations are confirmed by the works cited in [55], it must be also considered that the interest in using thermoplastic polymers for structural applications is still relatively recent and similar problems have been overcome for metal AM [60]. In industrial applications, thermoplastic reinforced polymers became relevant due to sustainability concerns, with these materials being used to replace thermosetting non-recyclable polymers. The use of reinforcement is important to ensure greater stability and better mechanical properties than unreinforced thermoplastics [61]. Exploring the advantages of AM features in an industrial manufacturing context is the next step, as AM can be used to add locally controlled properties to the final product, such as variable reinforcement orientation, leading to improved high specific strength and stiffness [62] typical of the long fibre reinforced polymers. To aid in the design of bonded joints with AM construction, it is essential that characterization methods for polymeric AM adherends and joints are well defined and available.

Regarding the characterization of AM thermoplastic bulk materials, one of the most relevant works is the report by Forster [63] published by the National Institute of Standards and Technology (NIST). It is worth noting that, even if all major quasi static and dynamic mechanical characterizations methods are considered, the existing standards are designated as non-applicable or applicable only with modifications. This is because it is necessary to consider the unique anisotropy, microstructure and mesostructure in the material due to the AM processes. Moreover, AM is often used to create components with tailored through-the-thickness structures to control the overall behaviour under loading. For example, the Poisson's ratio [64] or the absorbed energy under compression [65] or impact [66] can change during the test, which means that the application of standards developed for isotropic material could be non-feasible.

24

For these reasons, many authors suggest rethinking the AM component design and validation testing, using an approach similar to that of composite materials. It consists in considering the structure as a build-up of material and geometrical properties, starting from the micromechanics all the way up to the whole structure. This approach appears to be the most promising as there are works pointing out that models developed for composites can be used to predict the behaviour under load of AM specimens, although calibrations are necessary to take into account aspects such as the porosity and crystallinity of AM microstructures [67–71].

Orthotropic mechanical properties of FDM/FFF parts have been investigated by several works experimentally, e.g. studying the effects of bed orientation, Cantrell et al.[72], infill percentage and infill typology, Fernandez-Vincente et al.[73], layer thickness and extrusion width, Corbett et al. [74], extruder temperature, print speed, and layer height, Abbott et al. [75]. There are also interesting numerical, Sheth et al. [76], and analytical, Casavola et al. [77], approaches that correlate the orthotropic mechanical properties to the raster settings.
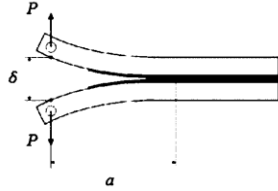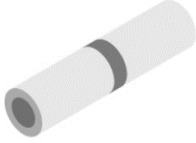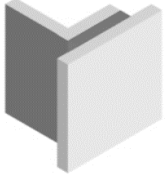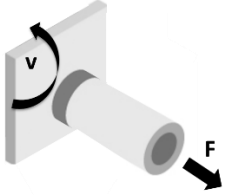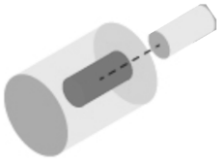
Furthermore, the constant development of new AM process features, in particular the Multi Material Additive Manufacturing (MMAM), both at macro scale and at voxel size, with the DMs to obtain FGM [46], highlights that current standards are not adequate.

A review of the literature allows to identify a set of testing solutions, which can be standard or modified, and to understand their relative advantages. To analyse physical effects, for example the surface energy resultant from a different crystallinity level, standard characterization methods are quite appropriate, and no new methods are necessary. For MMAM critical aspects exist, which are the chemical compatibility of heterogeneous materials and the stacking sequence. The first can be addressed using indirect mechanical evaluation, for example with modified tensile specimens [78–80] or the butt joint test [81,82], while the latter is AM resolution dependent. Using a finer process, such as polijet, it is possible to achieve seamless boundaries between different materials [83], while coarse resolutions, typical of FFF, can lead to adhesion failure and delamination [82]. However, geometrical methods can be used to prevent MMAM delamination [39].

To characterize the macro behaviour that results from material or geometrical AM tailoring optical methods, i.e. digital image correlation (DIC), have been shown to be an effective tool. In many works, optical methods were used to tune the joint design or experimentally confirm data obtained from models by extracting a plot of the full field strain.

25

Table 1 summarizes the methods used in the literature to investigate AM joint performance. It can be used as reference to quickly identify which characterization methods were validated for use with AM bonded joints.

Table 1: Overview of the joint configuration and characterization methods validated for AM.

Joint configuration	Reference
Double cantilever beam	Morano et al. [55, 56], Alfano et al.[36], Garcia-Guzman et al. [30].
Single lap joint	Dugbenoo et al. [29], Spaggiari et al. [21], Garcia et al. [22], Garcia-Guzman et al. [30], Cavalcanti et al. [24], Fieger et al. [38], Kumar et al. [40,41], Sekiguchi et al. [33], Redmann et al. [47], Dahmen et al. [48], Bürenhaus et al. [23], Li et al. [25], Yap et al. [31], Kovan et al. [27], Ubaid et al. [44], Kariz et al. [28].
Butt-joint	Kovan et al. [26].
T-joint	Dahmen et al. [48].
Centrifugal Adhesion Testing Technology	Leicht et al. [37].
Shaft-tube joint	Khan et al. [63, 64].

Finally, it is worth noting that new opportunities for joint characterization and monitoring during testing are created by the use of conductive thermoplastic materials, modified by metallic whiskers or carbon nanotubes reinforcements, which allow the direct manufacture of embedded sensors by direct printing [84–87].

1.3 Fatigue testing for additive manufacturing

Despite the relatively small age of AM there is a number of studies dedicated to fatigue. The fatigue of additively manufactured metal parts and components has been extensively analyzed and, among the others, the works from Nicoletto [88–90] offer an extensive set of interesting and useful results showing the effects of manufacturing details.

Fatigue behavior of plastics has been studied almost since the beginning of the polymer age: many references and data already from the '60 and '70 of the twentieth century can be found. Specimen made with FDM/FFF were also manufactured to be examined in fatigue by Gomez-Gras et al. [91], Letcher et al. [92], and Senatov et al. [93] with PLA; Moore et al. [94] with elastomeric polymers; Fischer et al. [95] with PEI. ABS specimen built by FDM/FFF have also been examined by several authors: Carutasu et al. [96] examined the tension/compression characteristics of ABS specimens made by FFF; Dawoud et al.[97] compared FDM with traditional molding techniques; Torrado et al. [98] and Ziemian et al. [99] examined the anisotropic behavior due to manufacturing and additives; Hart et al. [100] studied the fracture behavior; Gribbins et al. [101] examined even a component, a living-hinge manufactured by FDM. Fatigue behavior of the ABS when manufactured in FDM has been also already examined: Ziemian et al. [102] examined stiffness degradation caused by fatigue damage considering different mesostructures at various deposition angle, in cyclic tensile tests with a stress-ratio R = 0.1; Padzi et al. [103] with similar loading conditions compared different forming methods, that is traditional molding and FFF; Lee et al. [104] also examined the deposition angle and direction; Zhang et al.[105] instead considered alternate loading.

1.3.1 AM fatigue strength evaluation

In this section, fatigue testing on polymeric AM specimens with loading in plane bending was investigated. Plane bending loading mode was demonstrated to be very convenient for metal AM components, as shown in several works by Nicoletto [88–90]. An extensive test campaign, considering the effect of deposition was performed on polymeric AM specimens. Also, the effect of different stress-ratio R was considered. The analysis of the effects of these different parameters give a deep insight into the evaluation of the fatigue behavior of additively manufactured components made of ABS, and it will be a basis for the design of components made of this material in FFF.

In this study, the specimen geometry developed by Nicoletto [88–90] for additive manufacturing was used after scaling by 2:1 to be adapted for polymeric materials (Figure 13). The original specimen would have been too small and the forces too little for a proper measurement.

Characterization of AM processed materials

This specimen is designed to be tested with plane cyclic bending loading. It is essentially prismatic, 46 mm in length, 10×10 mm^2 minimum cross section, 10×14 mm^2 cross section with a lateral semi-circular notch 4 mm radius.

The advantages of this miniaturized geometry are the reduction of material, the absence of supports need, required and mostly the remarkable reduction of production time, and a relevant issue for fatigue qualification.
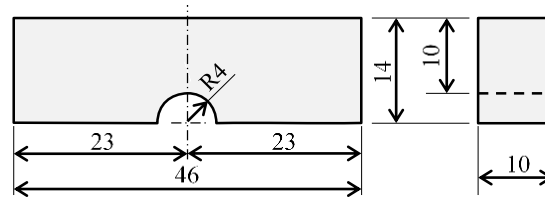
Figure 13: Specimen geometry.

The 3D print of the specimens was carried out using a Prusa i3 mK2s, placing the specimens near the zero, long dimension parallel to x-axis, with a nozzle temperature of 250 °C and bed plate temperature of 100 °C. After fabrication, the specimens were cooled down to room temperature on the bed plate in order to minimize swelling. In FFF there are many building parameters. A standard construction, with the aim of reducing manufacturing time but with sufficient strength and dimensional stability, corresponds typically up to 50% infill density. In this work, to obtain a structure able of the highest mechanical strength, possibly comparable to the base material, parameters with a reduced 0.1 mm layer height, maximum nominal infill density (100%), and raster orientation ±45° (criss-cross along the layers relative to the longer dimension) were used.

Standard tensile specimen, built with the same parameter used for fatigue specimens, were tested and to produce the material characterization data of the AM processed ABS (Table 2).

Table 2: Tensile tests results, data obtained using ISO 527, specimen 1BA.

Results	Tensile modulus E (MPa)	Yield strength σ_y (MPa)	Yield strain ε_y (%)	Elongation at break ε_b (%)
Average	2470	44.8	2.5	5.6
Standard deviation	19.4	0.652	0.23	2.0
Coefficient of variation %	0.79	1.46	9.27	36.24

Three build directions were investigated in order to study the directionality fatigue behaviour under the same nominal bending stress. Figure 14 shows the placement on the build plate and respective denomination of the AM FFF specimens.
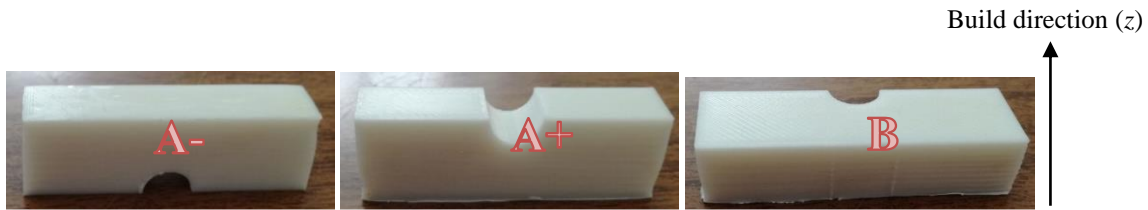
Build direction (*z*)

Figure 14: Specimens used in the experimental program, oriented according to the build direction.

Fatigue experiments were performed using a Schenk PK103 fatigue testing machine modified to apply plane bending load to flat specimen. A load cell was added to the system to continuously monitor the load applied to the specimen during cycling. Due to the characteristics of the machine, the bending load was applied in displacement control, at 25 Hz frequency. Specimens temperature was monitored using a thermographic camera Fluke Ti25 Thermal Imager (Fluke Ibérica, S.L., Madrid, Spain), no relevant temperature gradient was assessed. Consequently, the load being monitored was applied with stress amplitude in a range between 4 MPa and 33 MPa, according to the material properties evaluated with quasi-static characterization (Table 2). As it is well known, in displacement control the fracture does not occur explicitly: as soon as the fatigue crack nucleate and propagate the specimen compliance will increase. Crack propagation can even no longer continue and, to detect fatigue failure, compliance measurement must be done. For this reason, the load was continuously monitored, and failure was considered as soon as the stiffness decreased of 10% with respect to the initial value.

Six sets of specimens were tested, two for each build direction (Figure 14), one under bending moment with $R = 0$ and one under bending moment with $R = -1$ (Table 3): Figure 15 two examples of the signal acquired during 1 s is shown. The shown stress is the nominal stress computed with the simpler linear stress distribution of the bending of beams: the curves reported in Figure 15 meant to verify the correct load application to the specimen.

31
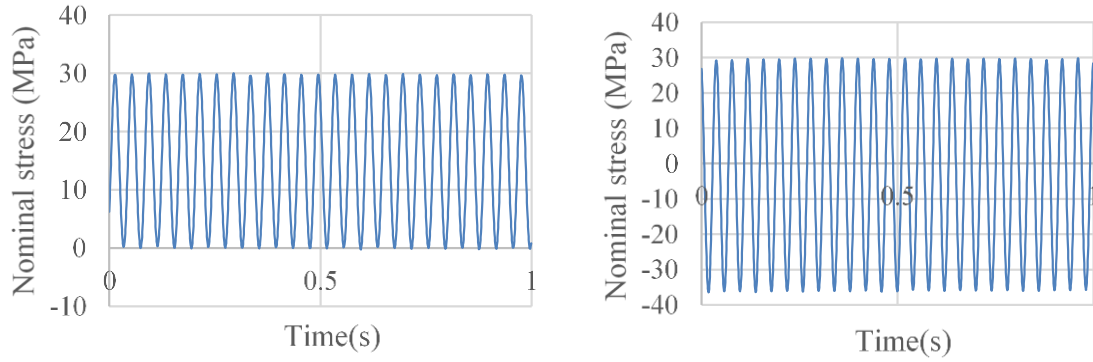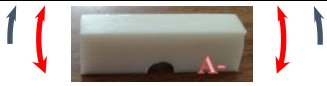
Figure 15: Two examples of the load signal acquired during tests: (a) σ_a = 15 MPa, R = 0; (b) σ_a = 30 MPa, R = −1.

Table 3: Experimental plan.

Load		Stress ratio	Characterization stress range MPa
		$R = 0$	4 - 16.5
		$R = -1$	8 - 33
		$R = 0$	4 - 16.5
		$R = -1$	8 - 33
		$R = 0$	4 - 16.5
		$R = -1$	8 - 33

As also shown by Nicoletto [90], the specimen geometry introduces a non-linearity in the distribution of the stresses through the thickness. The notch creates a stress increase evaluated as 1.56 in the cited work. For comparison the stress-ratio between the actual maximum stress and the nominal maximum stress calculated for a rectangular section under bending moment can be estimated equal to 1.597 with ANSYS 17.2 and only 1.497 with Altair OptiStruct 2017 (Figure 16). The average value of 1.55 very near the value proposed by Nicoletto [90] will be adopted. The current model also considers a linear elastic material model since, from the material characterization results, for the level of maximum stress reached during fatigue testing the material still behaves as perfectly elastic.
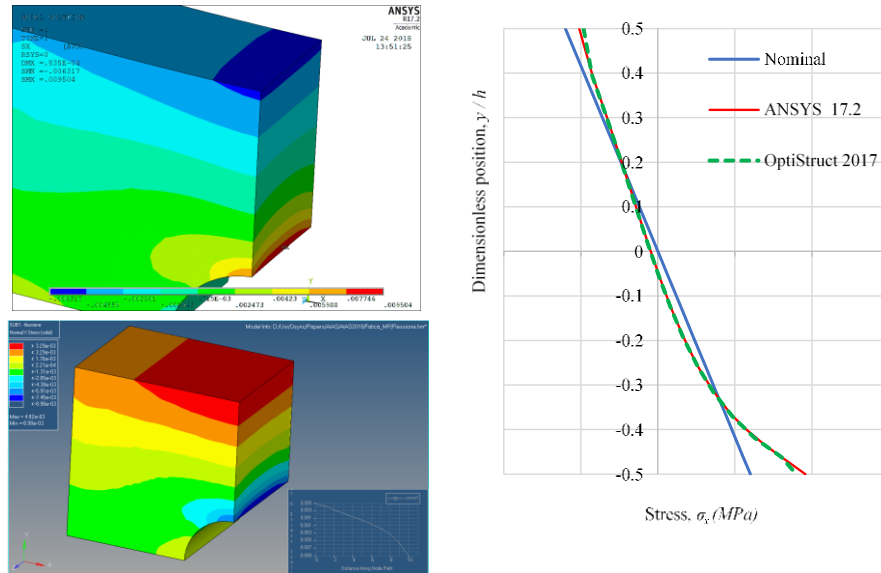
Figure 16: Stress distribution through the section calculated by two FE codes: ANSYS 17.2 (top) and Altair OptiStruct 2017 (bottom). On the right the comparison along the transverse mid-section.

1.3.2 Fatigue results for additively manufactured ABS

The fatigue of ABS has been examined in several works already mentioned in the introduction [90-105]. Figure 17 compares some recent results in terms of S-N curves for apparently equivalent ABS specimens, loaded in similar conditions, that is all loaded with a stress-ratio R = 0.1. At a first glance, it appears that large variations, expected with polymers, are observed: in some cases, a ratio of approximately two is found between the largest and smallest value of strength for the same endurance. The slope of the S-N curve is similar in most cases but there are different trends in some published data.

Another similar comparison is given in Figure 18 where results of tests on ABS specimens made with AM technologies are compared are not reported since they excessively deviate [106], of around one order of magnitude, from all the other literature results. In this case also, significant differences are found. By comparing Figure 17 and Figure 18, it can be noticed that the AM values are only slightly different to the values obtained testing injection molding specimens (for equal endurance).

33
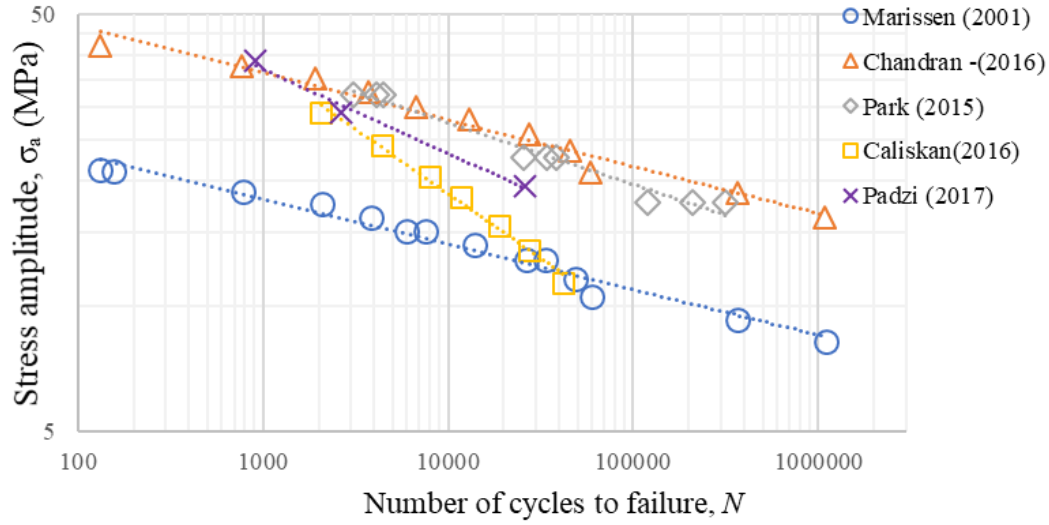
Figure 17: Comparison of the S-N curves for ABS polymer from various literature sources.
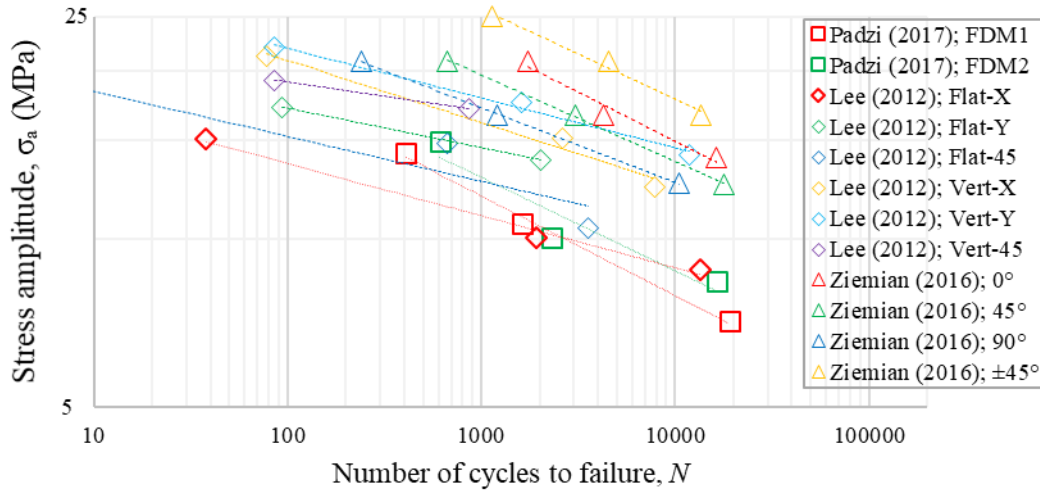
Figure 18: Comparison of the S-N curves for ABS polymer processed with FDM/FFF from various literature sources.

Results from fatigue tests gave interesting information: the scatter was relatively contained despite the various sources of uncertainties due to the unavoidable manufacturing defects including poor surface finish (each specimen was tested *as is,* i.e. without surface modifications) and the typical internal defects of FDM/FFF. However, the S-N curves showed defined trends that will be discussed.

In Figure 19 a comparison between the S-N curves obtained experimentally from the A specimens in the two deposition orientations is reported. From a first observation, there is a clear influence of the stress-

ratio. The influence is not the same and A- specimens were much more affected by the different stress-ratio, especially in the low range of endurance. This difference can be related to the build direction, with the notch faced down, that is critical for geometry accuracy.
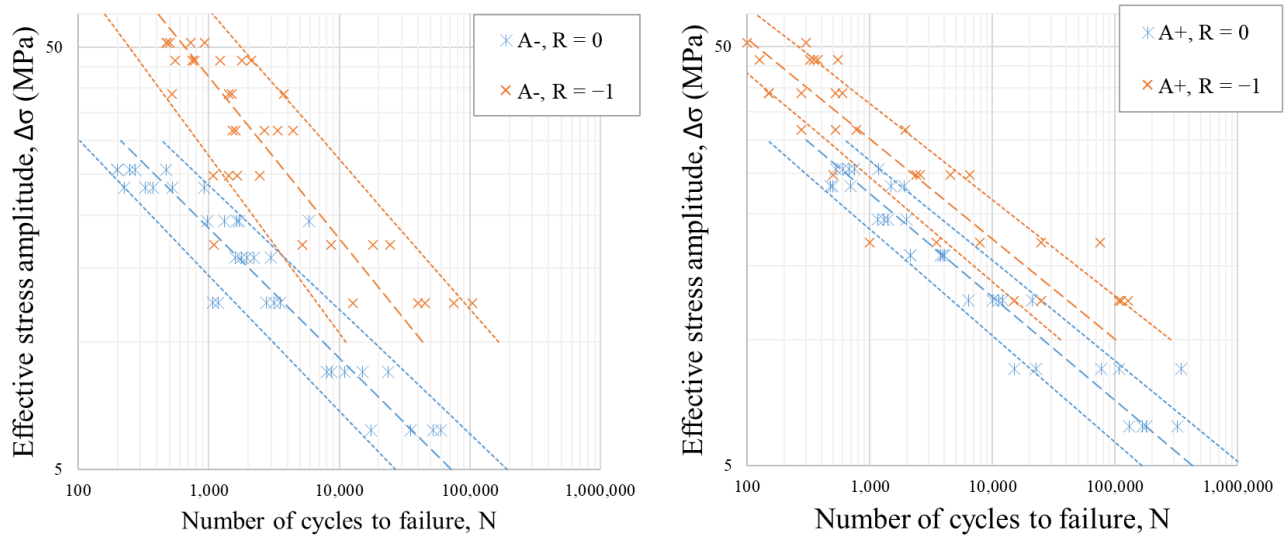
Figure 19: Comparison of the experimental S-N curves (peak-to-peak stress) for the A orientation specimens: effect of the stress-ratio.

The second comparison is, for the same stress-ratio, between the two deposition directions for specimen A (Figure 20). In this case, the difference appears less significant especially for stress-ratio equal to −1: the two samples seem from a same population meaning that the direction has a limited impact for some values of the endurance.
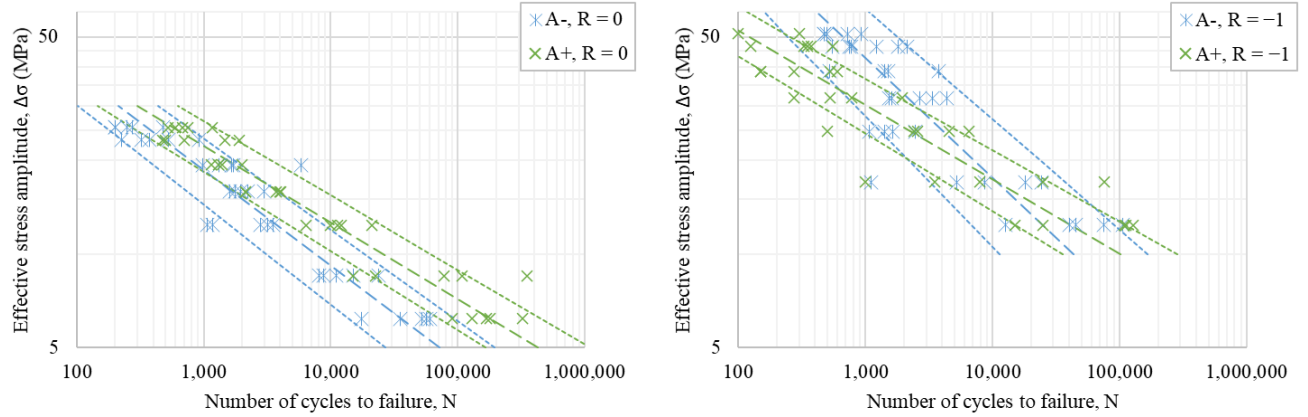
Figure 20: Comparison of the experimental S-N curves (peak-to-peak stress) for the A orientation specimens: effect of the deposition direction.

Last, the same comparison as in Figure 19 is reported for the B specimens (Figure 21). Similar conclusions can be drawn, and a clear effect of the stress-ratio occurs, almost independent of the number of cycles to failure.
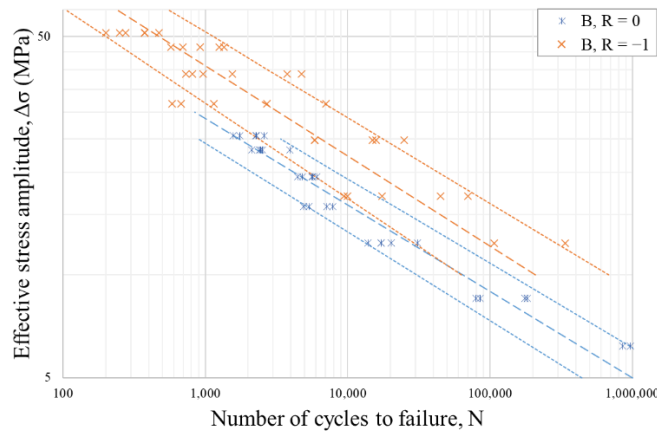
Figure 21: Comparison of the experimental S-N curves (peak-to-peak stress) for the B orientation specimens: effect of the deposition direction.

Apparently, deposition, as in the case of the B specimens, gives slightly superior fatigue strength. For example, if reporting the estimated average fatigue strength corresponding to values of the endurance of 5×10^3 and 5×10^5 cycles (Figure 22), its value is around 20-25% higher. It is interesting to note that, as observed from Figure 20, the effect of the deposition direction is different depending on the endurance: strength is nearly the same at lower number of cycles and diverges at higher duration. This aspect, worth

36

of further investigation, is apparently not of statistical nature since a large number of specimens was evaluated at the stress level of interest. Some discussion is also added in the next section.

(a)

(b)
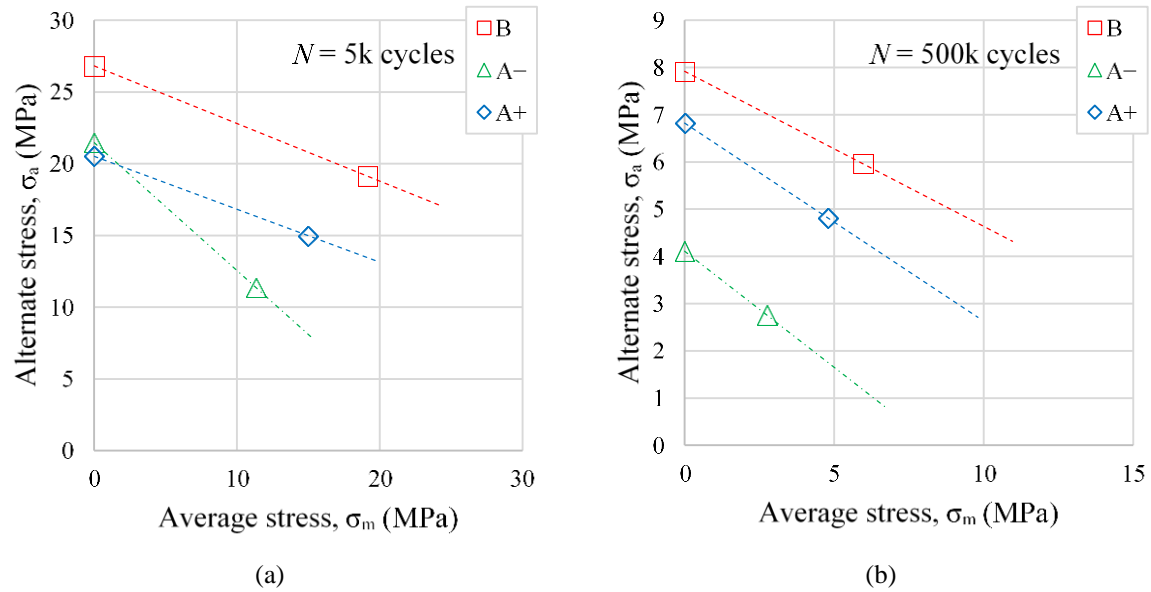
Figure 22: Effect of the stress-ratio on the fatigue strength of the examined ABS produced by AM: estimated average values for two level of endurance: (a) 5×10^3 cycles to failure; (b) 5×10^5 cycles to failure.

1.4 Discussion and general remarks

Observing data in the previous sub-section, a certain scatter can be noticed. This is worth to be more investigated because, from the studies on components build with traditional process, it is well known that fatigue failure at high stress level are due to defects, but at low stress level failures should be mostly function of the specific material. It is also known that a certain level of internal defects is intrinsic to the FDM/FFF process that use a continuous filament (void and approximation at curvatures) and as trade-off between geometry precision and adhesion, as shown in Figure 23.

(a)   (b)
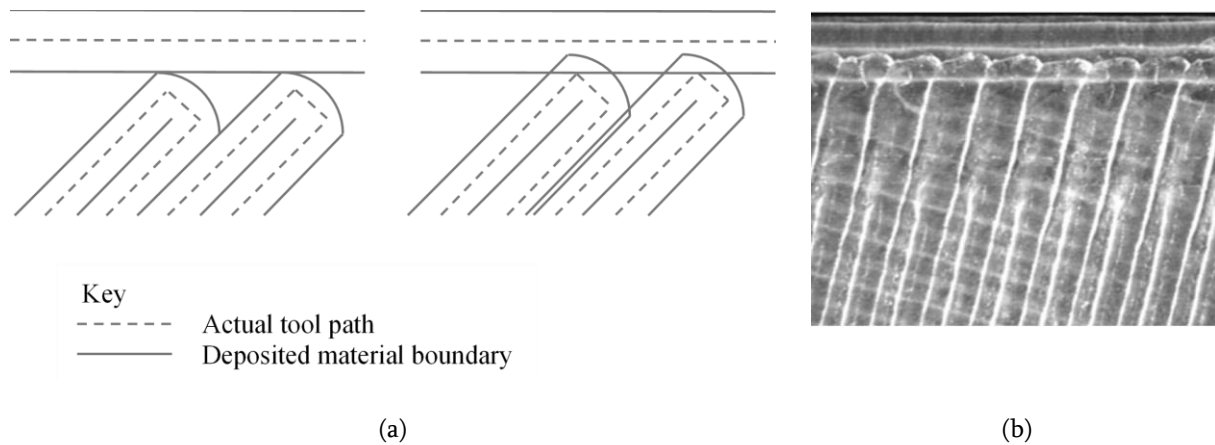
Figure 23: (a) Schematic of different possible tool path and the effects on the geometry, adhesion and voids, by Gibson et al.[19] and (b) Example of FFF processed material.

The specimens to be investigated were selected at lower and upper range of cycle life at failure for each stress level.

Observing the magnified surfaces of the specimens, it was possible to draw some conclusions. The specimens at the lower end present two characteristic situations (Figure 24):

- Incorrect control of the deposition temperature of the filament: a temperature lower than the optimal prevents the correct adhesion between layers and the sides of the filament along the pattern in the raster. This is a critical problem because its effect is a decrease of the actual section of the component. In Figure 24(a) a critical configuration is shown: the load is carried almost only by one filament at some joined points. The signs of crack propagation on the fracture surface remarks the inhomogeneous mechanical properties of the material. On the other hand, setting the temperature too high can cause local degradation of the polymeric materials.

Characterization of AM processed materials

- Inaccuracy in the position of the filament: it is attributable to the open loop control or to an imperfect hardware configuration. In this case, the filaments and the layers are well bonded, but the deposition errors create critical points that can start the crack propagation (Figure 25). This problem is solvable by improving the machine calibration.
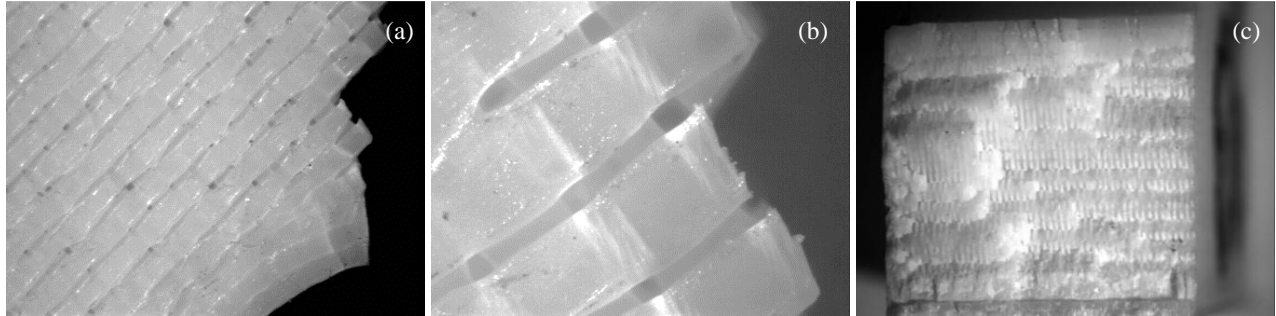
Figure 24: Observed defects: (a) inaccuracy on temperature of deposition; 12×; (b) detail of the fracture, 50×; (c) fracture surface, 6×.
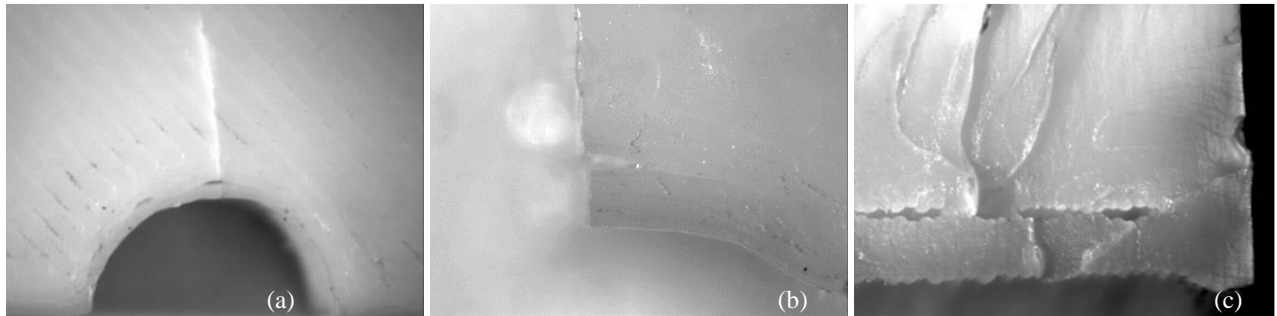
Figure 25: Observed problems: (a) inaccuracy on filament placement, 6×; (b) Detail of the fracture surface, 25×, (c) fracture surface, 25×.

While investigating the specimens with the longest endurance at each tested stress level, it is apparent that they have both external surface and cross section smooth and well packed: this is a confirmation of a more accurate deposition temperature and filament placement. By comparing Figure 24 and Figure 26, it is remarkable that on the fracture surface it is almost impossible to distinguish the cross section of the filament.
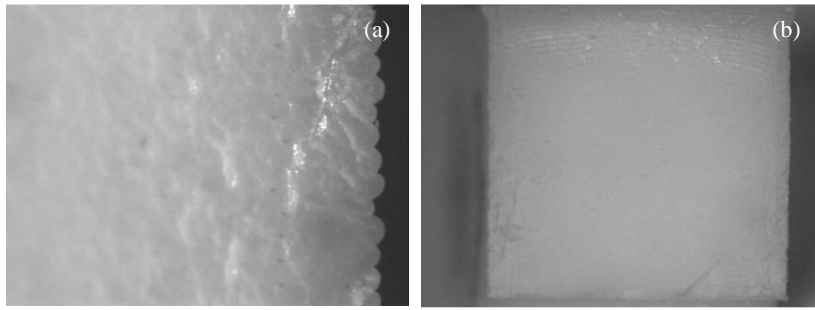
Figure 26: Detail of the fracture surface of the specimens, in the upper range of life: (a) 50× magnification; (b) 6×.

Comparing the original experimental results with data found in the literature, it can be noticed that they stay within the average if not at the upper limits: a direct comparison is hard to perform seen the uncertainties in the actual type of material, technology and manufacturing parameters, and the different type of specimen. However, the presented data are compatible with others and add some additional insight into some important influencing factor as the presence of a constant stress added to the alternate component.

Finally, in this section, some experimental results about the fatigue strength of additively manufactured specimens of ABS were presented. The experiments were performed in plane stress conditions with two different values of the stress-ratio. S-N curves were obtained loading at different levels of stress amplitude to obtain values of the endurance from around 10^3 to 10^6 cycles to failure. An innovative type of specimen, equivalent to the type used by Nicoletto [88–90], was used: this type of specimen is nearly prismatic with a central notch. The main difference was the size, doubled along all directions, to be more suitable to the lower strength of the plastic material used.

The obtained results confirm the known effect of the stress-ratio and show limited scattering despite the, almost unavoidable, presence of defects in the AM parts. On the contrary, less important effect has been observed due to the manufacturing details, especially the different deposition directions.

The obtained results, even with the limitations of the limited number of tests and stress-ratios examined, give some interesting insights on the fatigue strength of components realized in additive manufacturing and add knowledge to this still not completely explored field

Chapter 2

Joints designed for Additive Manufacturing

This chapter is based on paper [107], the aim is to assess the current modelling and experimental achievements in the design for additive manufacturing of bonded joints, providing a summary of the current state of the art. To limit its scope, the chapter is focused only on polymeric additive manufacturing processes. As a result, this chapter contains a structured collection of the tailoring methods adopted for additively manufactured adherends and adhesives with the aim of maximizing bonded joint performance. The intent is, setting the state of the art, to produce an overview useful to identify the new opportunities provided by recent progresses in the design for additive manufacturing, additive manufacturing processes and materials developments.

2.1 Background and motivations

The industrial interest in AM has been a driving factor behind the development of modern 3D printer machines [20] and their novel features, such as MMAM simultaneous processing [83]. This interest has led to increased process standardization [108] besides the adoption of new design approaches for additive manufacturing (DfAM) [109], and new materials. DfAM urges to rethink component design by taking into account both the specific constraints and new opportunities created by the AM processes. Many studies have analysed these constraints, demonstrating that placement for printability, printing parameters and printing setups can affect the surface finish, geometrical accuracy and the mechanical properties of the resultant components [109–112]. Therefore, the nominally limitless geometrical freedom of AM is in fact restricted by an important set of design parameters.

As the knowledge in DfAM increases, so it does the potential of AM. Although still limited by a relatively modest production rate, if compared to traditional manufacturing processes, AM finds practical use in the production of highly optimized components of limited size to be assembled in larger structures [113]. Moreover, this approach addresses the exponential relationship between building volume and printer cost and allows to improve productivity using several 3D printers working in parallel, avoiding complete stoppages of production during maintenance [23]. However, the design approach that focuses on splitting the components in order to overcome current AM processes limitations introduced above, requires the use of an effective joining procedure to create a larger final product from the smaller subassemblies.

One of the earliest works on joining AM components was carried out by Espalin et al. [114], in which the authors identified the techniques suitable for assembling polymeric AM components, which include ultrasonic spot welding, hot air welding, solvent joining and adhesive joining, and another was carried out by Arenas et al. [115], in which a method was proposed to select structural adhesives for AM.

Subsequent studies explored joint performance improvements using AM as a joining tool, the AddJoining process [116,117] with or without co-curing, and a voxel-oriented design [118] approach. A hybrid approach combining the first two solutions was also considered. The AddJoining process consists in 3D printing the substrates and the joint simultaneously, using the structure as the build plate. The voxel-oriented design approach consists of exploring the local material control enabled by AM with previously acquired know how on adhesive bonding [17] to develop new joint design solutions.

After this introduction, the existing literature is sorted according to the design strategy used by the authors and details are given for each of these techniques. In the last section, the advantages and disadvantages of the proposed techniques are summarized, and some general remarks are drawn.

43

2.2 Joint Design Strategies for Additive Manufacturing

The process of optimizing the design of bonded joints can be briefly described as maximizing the load carrying capacity of assembled components in order to withstand higher service loads. Initially, joint design strategies were based on selecting materials with better material properties and on maximizing the bonding area. Later, with the growing need for developing lightweight structures, the investigations on the physics of the adhesion and the advances in modelling techniques enabled the development of alternative joint design strategies [119]. These design strategies are based on a better understanding of stresses acting on the adhesive layer, on the adhesive and of the effect of adherends material properties. This knowledge is implemented in novel geometrical configurations in order to lower peel and cleavage stresses [120]. Even if the overall joint design is a compromise between an optimal geometrical configuration and constraints on component sizes, more localized solutions can be implemented in order to change the stress distribution in the bondline. Adhesive stiffness is a major factor that affects the stress distribution along the overlap [121], thus a locally modified adhesive [122] can improve the strain tolerance of the joint and delay failure. Another option to improve the stress distribution in the adhesive can be to locally modify the adherend geometry [123]; for example, by tapering the adherends at the overlap ends to lower the stiffness, and thus stress in these critical locations. Another approach that can be used to improve the level of adhesion [51] is the use of chemical or mechanical treatments, to modify the bonding surfaces. All of these design concepts can be taken to an extreme by exploiting the material properties and geometrical AM controlled at the voxel resolution [118]. In this section, the use of AM to improve joint design is discussed in detail, sorting the works as detailed in Figure 27.
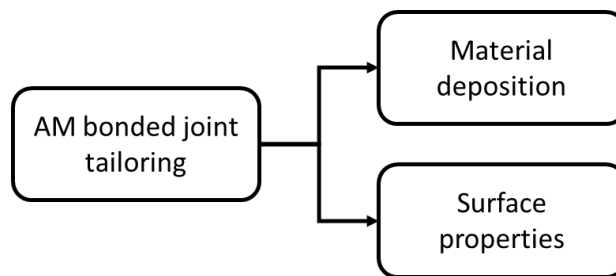
Figure 27: Macro sorting of the design strategies for additive manufacturing (AM) bonded joints.

The first design strategy discussed is the use of AM to locally change the material properties in the joint. This approach can be implemented by simultaneous deposition of different materials, for example with MMAM [83] in order to obtain functionally graded adherends and adhesives. This is a design concept that

44

has already been investigated for other manufacturing processes [122,124]. Another option can be using AM to create complex structures in the thickness direction, such as a lattice, cellular or auxetic structures, which will guide the deformation under load of the joint and affect the modulus by introducing controlled porosity.

In the following sub sections, the works concerning AM tailored materials and joints shown in Figure 28 are presented.
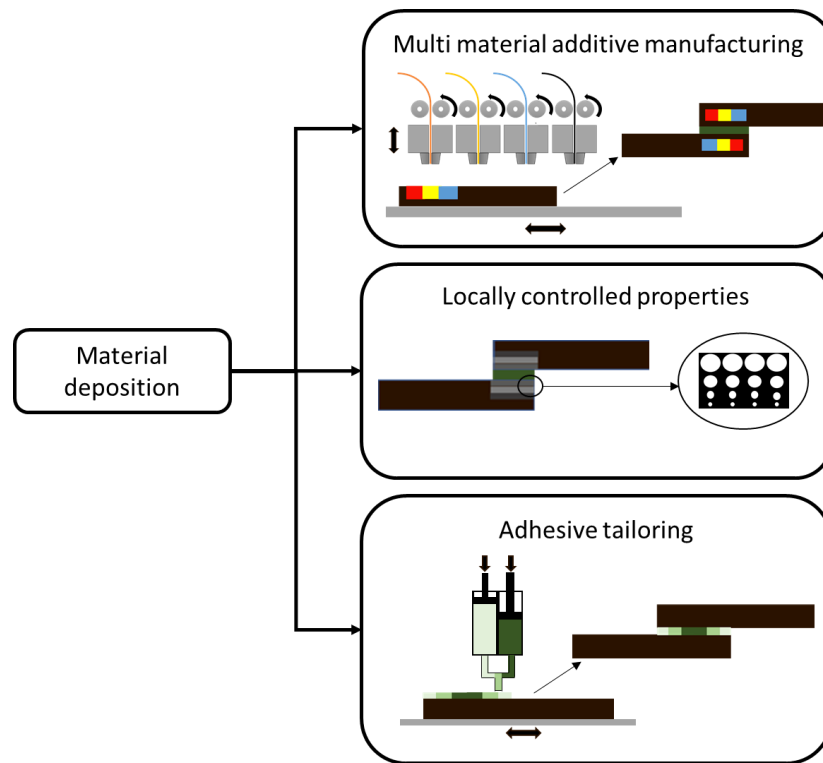
Figure 28: Voxel oriented material deposition design strategies for AM bonded joints.

2.2.1 Multi Material Additive Manufacturing to optimize the stress distribution in the bondline

Kumar et al. [40,41] and Khan et al. [42,43] used AM to create single lap joint (SLJ) geometries with tailored modulus in the bondline layer without additional joining, a process conceptually similar to that of AddJoining [116].

In a preliminary study, Khan et al. [125] implemented an analytical model to investigate the effect of tailoring the elastic modulus along the full length of SLJs. The aim was to evaluate the effect of introducing the additional design variable of material compliance using the MMAM processes. A general approach applicable to adherend and adhesive has been developed, based on the Euler-Bernoulli and Timoshenko

45

beam theories, to obtain a sandwich structure representative of an SLJ. From a parametric analysis, carried out using the analytical model, the authors were able to show several configurations in which, using MMAM elastic modulus tailoring, stress peaks at the overlap ends were reduced and, therefore, the overall load carrying capacity of the joints was enhanced. In subsequent works, authors used the general analytical model applied to several joint configurations and then experimentally assessed the effect of the proposed stiffness tailoring approach.

Kumar et al. [41] first explored the effect of using a material with a lower elastic modulus at the overlap ends with a step wise pattern (Figure 29). The focus was on the optimization of the overlap stress distribution using the volumetric percentage v_c of low-stiffness material of the total material in the bondline as a design parameter. Taking advantage of the photopolymerization process resolution, the authors were able to obtain two digital materials with hybrid characteristics with respect to the bulk materials [126], with an elastic modulus ratio between the high-stiffness material and the low-stiffness material around 2. A first investigation using the finite element method (FEM) of the SLJs indicated a beneficial effect of the material tailoring on the shear and peel stresses distributions at the overlap ends, with minimum stress values being achieved for v_c values in between 0.1 and 0.2. However, a detrimental effect at the material interface was also reported, due to a stiffness mismatch. Experimental tests were carried out on SLJs for v_c values between 0 and 1 for a discrete step increase of 0.2. Results confirmed that the best configuration is for v_c equal to 0.2 with joint performance improvement of 23% on ultimate load and 37% on toughness with respect to the solution with only the stiffer material.
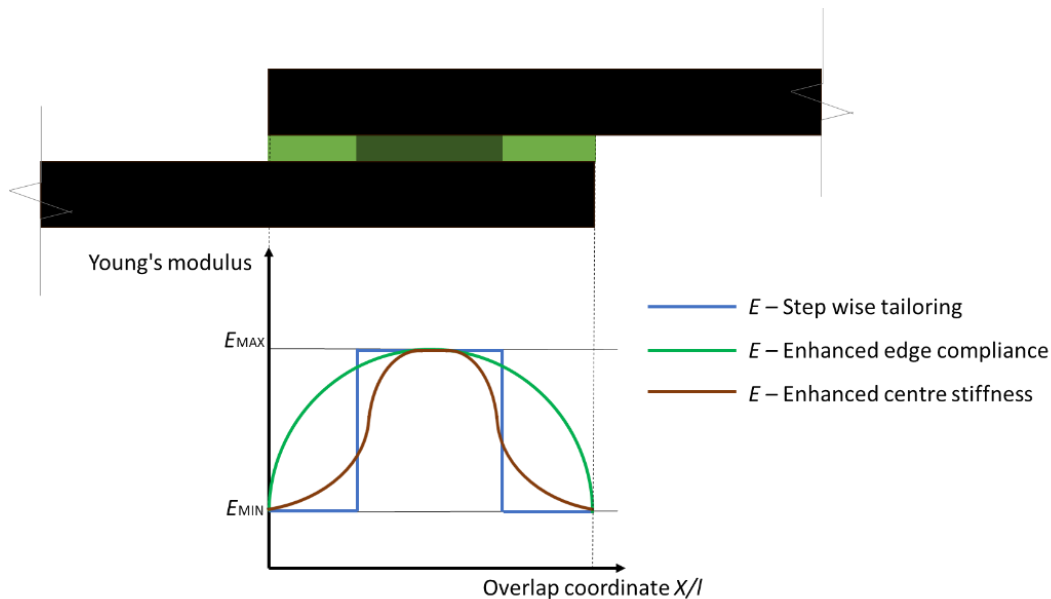
Figure 29: Bond line modulus tailoring using digital materials for single lap joints [40,41].

In a following work [40], the authors improved the design of the modulus tailoring, seeking a gradual variation along the overlap (Figure 29) mimicking with the DMs the structure of a second phase dispersion in the adhesive. Reference SLJs were fabricated with neat homogeneous material, in order to assess the effect of the modulus tailoring, and with the spheres of the dissimilar material evenly distributed over the overlap zone. Experimental results were similar for both tailored configurations, with a maximum load increment of about 100% and a joint toughness increment of 169% with respect to the standard configuration. The results also demonstrated that modulus tailoring can change the failure mode, from adhesive to cohesive due to the reduction in peel stresses. It is worth noting that the presence of spheres has a beneficial crack arresting effect even if the interface between the different material can be considered as a flaw in the adhesive. Moreover, even if the process resolution in the layer was about 50 μm, authors had to use geometrical features at least 10 times larger than the minimum resolution in order to respect design tolerances. This technical constraint led to the use of thicknesses larger than usual in SLJ manufacture.

The works of Khan et al. [42,43] focused on the compliance tailoring of joints in cylindrical configurations using three different strategies for the gradation of the elastic modulus of the adhesive layer. These were the use of power law, exponential law and trapezoidal law (Figure 30). The authors developed a dedicated specimen geometry to test shaft tube joints under axial tensile loads with dimensions compatible with the resolution of the photopolymerization process. Tailoring strategies were based on spherical inclusions of DMs. At first, numerical and analytical analyses were carried out in order to investigate the best gradation coefficients for each elastic modulus design law [127]. In [43], authors observed that stress peaks at the tube end are greater than at the shaft ends, thus implemented monotonic elastic modulus variations using a power law and an exponential law. The bond layer elastic modulus at the overlap was tailored as a function of the axial coordinate between is the lowest elastic modulus (E_{MIN} = 280 MPa) and the highest elastic modulus (E_{MAX} = 2700 MPa). Numerical and analytical models pointed out different optimal configurations for the different gradation laws. Experiments confirmed the model results, showing a 40% increment in the failure load and a 25% increment of toughness with respect to the non-tailored configuration.
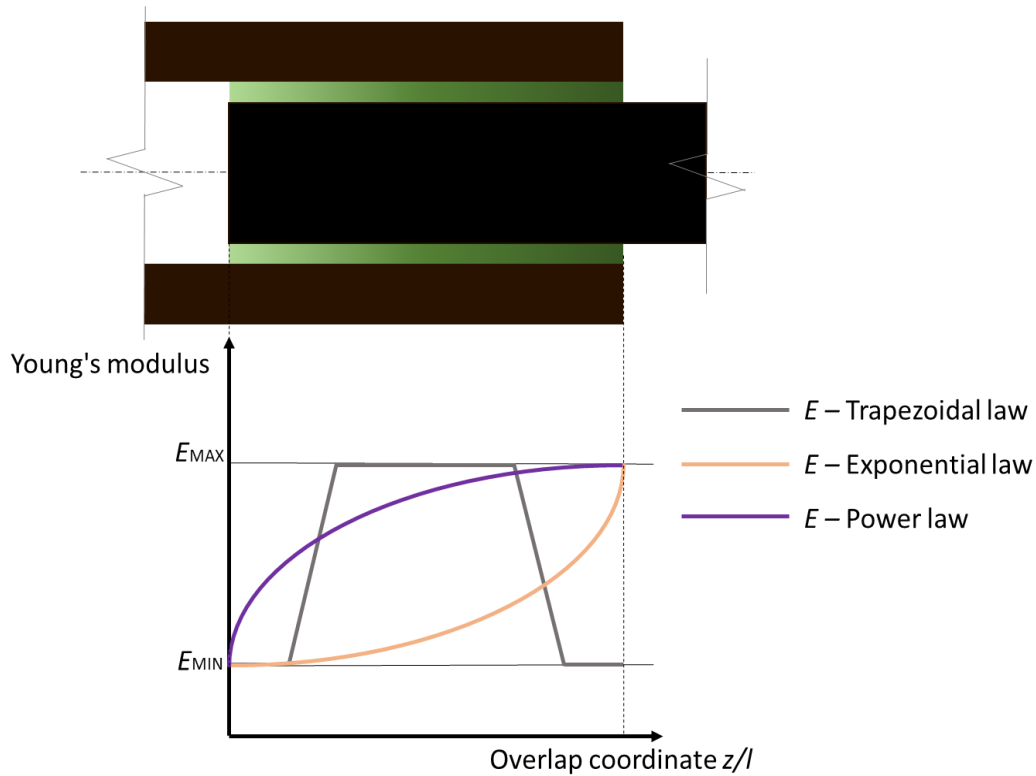
Figure 30: Seamless bond line modulus tailoring using DMs for tube-shaft joint [42,43].

In [42], authors investigated the effect of two-sided linearly varying elastic modulus profiles created using a trapezoidal law. The model output gives best results for adhesive gradation normalized on the overlap length equal to 0.25. Experiments on this configuration were compared to baseline solutions with homogeneous bond layers with elastic modulus E_{MIN} and E_{MAX}, which confirmed model previsions as tensile load increments up to 100% and toughness increments up to 69%. Comparing the results from [43] and [42] it can be observed that symmetrical elastic modulus bond layer tailoring is more effective than monotonic tailoring. This is true even for geometries that have non-symmetrical stress distributions under tensile loading due to the geometrical configuration of the joint.

Ubaid et al. [44] focused on the use of stiffness tailoring of the adherend to affect the stress distribution in the bond line and improve the overall joint carrying capacity. Authors took advantage of the DMs to control the material properties of the adherends. The 2D FEM models were implemented in order to investigate different tailoring configurations in the x and y directions for the SLJ geometry, as shown in Figure 31. The results of 1D tailoring showed that this design strategy led to an increase of secondary bending under load with consequent peel stress increases. With 2D tailoring it was possible to optimize

the material stiffness and improve the stress distribution and minimize the bending. The best configuration was found to be the one with non-monotonic tailoring as shown in Figure 31, with a reduction of peak peel stress by 57% and an almost constant shear stress distribution. Experimental tests on standard and tailored SLJs demonstrated the effectiveness of this configuration, with an improvement of 13% of the failure load, 20% of displacement at failure and 50% of the joint toughness confirming that 2D elastic modulus tailoring can be used to control the bending in the joint.
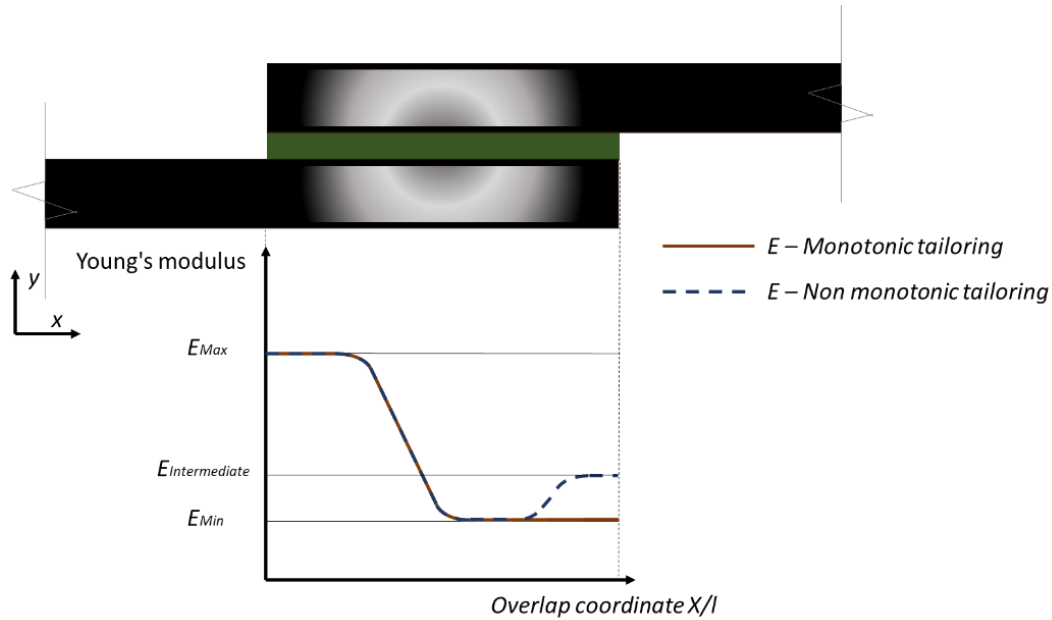
Figure 31: Adherend Young's modulus tailoring using digital materials SLJs [44].

2.2.2 Locally Controlled Properties using sub-surface structures to enhance damage tolerance of the joints

This subsection presents works that use, as design strategies, the introduction of tailored porosities, macro voids or cavities in the adherends to locally modify their mechanical properties. This allows, for example, to locally vary the material density [128] and thus to modify the overall joint response under loading. These design approaches can be considered an extension of the concept of varied densification from functionally graded additive manufacturing (FGAM) [129], in which the voxel oriented material modelling shifts the design focus from the geometrical dimensions to through-the-thickness structures in order to maximize the performance of the components.

A first feasibility study on crack trapping using AM for bonded joints was made by Alfano et al. [36]. In this work, the authors used simplified 2D sub-surface structures (Figure 32) bio-inspired by the *Balanus Amphitrite* in order to obtain a toughening effect. The aim was to improve the reliability and the damage

49

tolerance of AM layered materials as these are relevant factors for use with AM components in structural applications. The authors used the powder bed fusion process and PA to manufacture adherends with square and circular cross section structures through-the-thickness. Double cantilever beam (DCB) specimens were produced by bonding the resulting adherends with the Hysol 9466 epoxy adhesive (Henkel, Düsseldorf, Germany) without any surface modification. Experimental testing to assess the effect of the sub-surface channels on the energy dissipated by the joint were carried out. A global increment in load-displacement values were registered for the DCBs tailored with channels with respect to standard DCB adherends. The magnitude of the increment was distinct for the different investigated shapes using the DIC technique.
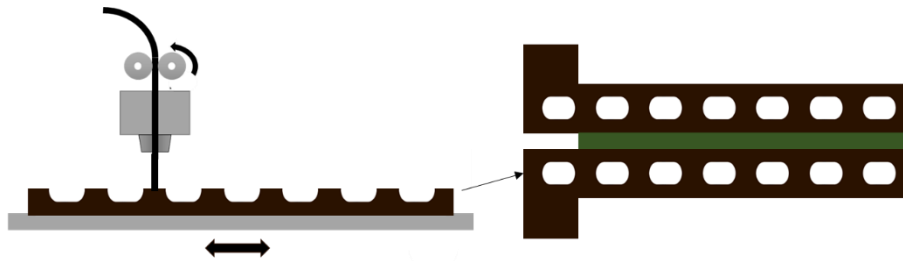
Figure 32: Adherend bio-inspired stiffness tailoring using a sub-surface geometry as proposed in [34–36].

These first promising results led to further investigation carried out by Morano et al. [34]. At first, FEM models for three different channel shapes were proposed and validated with experimental data in order to correlate the sub-surface geometry with the crack propagation behaviour under mode I loading. DCB specimens, in the same configuration proposed by Alfano et al. [36], were fabricated and tested. Using FEM simulation and the virtual crack closure technique (VCCT), the strain energy release rate was evaluated for both standard and tailored configurations. It was observed that the energy release rate was affected by the crack position with respect to the material distribution of the sub-surface geometry. By comparing the results obtained with the different channel shapes, it was established that channel shapes have a relevant effect on crack propagation and, therefore, a parametric study on sub-surface geometry was carried out in a second work [35]. It was found that increasing channel height, width and pitch has a positive effect on joint performance. Larger values for these geometrical parameters, lowering the adherend stiffness, led to the nucleation of secondary cracks that significantly increase the dissipated energy. However, these values are limited due to buckling phenomena and consequently there is an adherend strength reduction. The conflict between strength and toughness is a well-known engineering

problem [130], but recent works attempted to address it by developing new materials or material deposition micro bio-inspired patterns [131].

The work by Afferrante et al. [132] can be considered as complementary to the works by Alfano et al. [36] and Morano et al. [35] as it investigates the effect of 2D sub-surface structure with loading in different directions with respect to the tailored structures. The authors studied that it is possible to control the joint strength using the crack trapping mechanism and controlling the adherends stiffness. In a direction orthogonal to the embedded channel structures, the toughening effect is confirmed. On the other hand, crack propagation parallel to the channels is affected in a detrimental way. The direction-dependent adhesion properties must be taken in account while designing the AM tailored joints in order to avoid failure under accidental loading of the structure, but they also can be exploited to enable new applications, for example in robotic manipulation systems.

2.2.3 Adhesive tailoring to improve joints quality and performance

AM enables control over the material at voxel resolution and this, if coupled to MMAM, can be used to create joints with tailored physical and mechanical adhesive properties. One of the main engineering challenges in tailoring adhesives is to obtain a seamless variation in the material properties in order to obtain a functionally graded adhesive (FGA) behaviour [122]. FGA can be obtained by a continuous change in material composition and/or the microstructure along the overlap of the joint. The practical methods to obtain FGA adhesives are to mix adhesives with particles of different properties in different volumetric percentages, to create a non-uniform reinforcement distribution in the bond line or to apply different localized curing cycles. Usually the aim is to optimize the stress distribution in the bondline, lowering peel stresses at the overlap ends.

Redmann et al. [47], using AM based on photopolymerization, developed a joining method, similar to the AddJoining one [116], for composite reinforced fiber polymeric adherends. The authors assessed the feasibility of AM adhesive deposition using the b-stage curing epoxy EPX81 (Carbon Inc., Redwood City, CA, USA) and adherends made of NB-EP4030-D (Mitsubishi Chemical Holdings Corporation, Tokyo, Japan) pre-impregnated woven carbon fiber. The adhesive material was deposited in a controlled way on the adherends using the AM process based on the continuous liquid interface production (CLIP). After deposition, the adhesive was partially cured with ultraviolet (UV) light. Afterwards the substrates were assembled to form a SLJ and the cure was finished using a thermal cycle. Reference values were provided by testing monolithic SLJs of NB-EP4030-D carbon fiber reinforced polymer and adhesively bonded SLJs with 3M DP190 (3M Company, Maplewood, MN, USA), fabricated with the same dimensions. Micro–

51

computed tomography (micro-CT) testing showed that AM joints had a nominally void free adhesive layer with respect to manually deposited adhesive. Mechanical testing did not point out any relevant differences in terms of maximum shear stress, while lower strain at failure and lower toughness was identified for the manually assembled joints. Experimental testing proved that it is possible to deposit the adhesive in a controlled way using AM but the use of a b-stage curing adhesive places limitations on adherend-adhesive compatibility and on the processing temperatures.

The work of Dahmen et al. [48] was based on the work by Redmann et al. [47] and used the same 3D printing setup used in [47] and materials to assess if the proposed AM adhesive deposition method could be suitable for industrial application. As a case study, the authors considered a T-joint configuration, a non-standardized joint but highly relevant in aerospace industry applications, as it is commonly used in the spar-skin joints of aircraft wings.

The T-joint solution (Figure 33) is designed to transfer out of plane loads and is composed of a base platform, a bent vertical structure with a stiffening function integrated in the shape and a deltoid, which is a filler to stabilize the webs. It was assessed that the deltoid material and shape are a relevant factor to improve the joint load carrying capacity, but the actual manufacturing process, based on the manual pre shaping of the deltoid material, cannot guarantee reproducibility or a void free joint. The use of an AM process to introduce partially cured adhesive was identified as a possible solution to address the limitations of the manual process and to obtain highly optimized joint shapes.
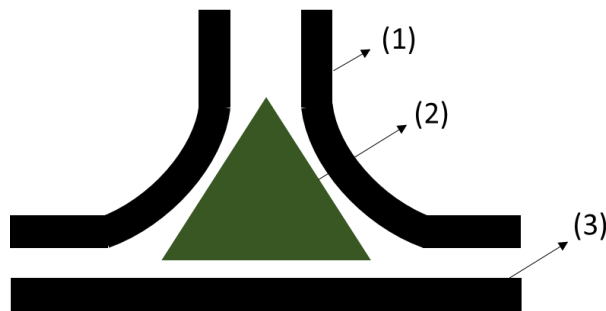
Figure 33: 2D view of the components of a T-joint assembly, webs (1), deltoid (2) and platform (3).

The joining process was performed using three different processes to manufacture the deltoid: adhesive bonding with AM, a manual process with adhesive bonding and a manual process with pre impregnated carbon fiber (Figure 34). At first, SLJs were manufactured in order to tune the process parameters and to set a reference using a standardized testing method. Results confirmed those reported in [47]. Failure

modes were mixed, exhibiting both adhesive and cohesive failure of the adhesive for the two bonding-based solutions while delamination occurred in the co-cured pre impregnated joint. Delamination was restricted to the bondline zone and did not progress to the adherends. An initial visual inspection confirmed the superior quality of the AM joints, without the porosity and voids associated with the manual adhesive deposition or the rolling process of the pre impregnated fibers (Figure 34). Manually processed T-joints, tested under a pull-out load, failed at 284 N, while using AM to apply adhesive the load at failure increased by 34%. The use of pre impregnated fibers was quite effective, showing a 47% increment over the manual reference. The authors pointed out that, considering relevant factors such as the different base material mechanical properties, joint defects and result reproducibility, the AM process appears to be the best solution, especially since the curing processes were not the subject of an optimization process. Moreover, the geometrical accuracy of the AM process could be used to tailor bonded joints for several specific applications, for example, in joining components with optimized and complex overlap geometries or hollow structures.
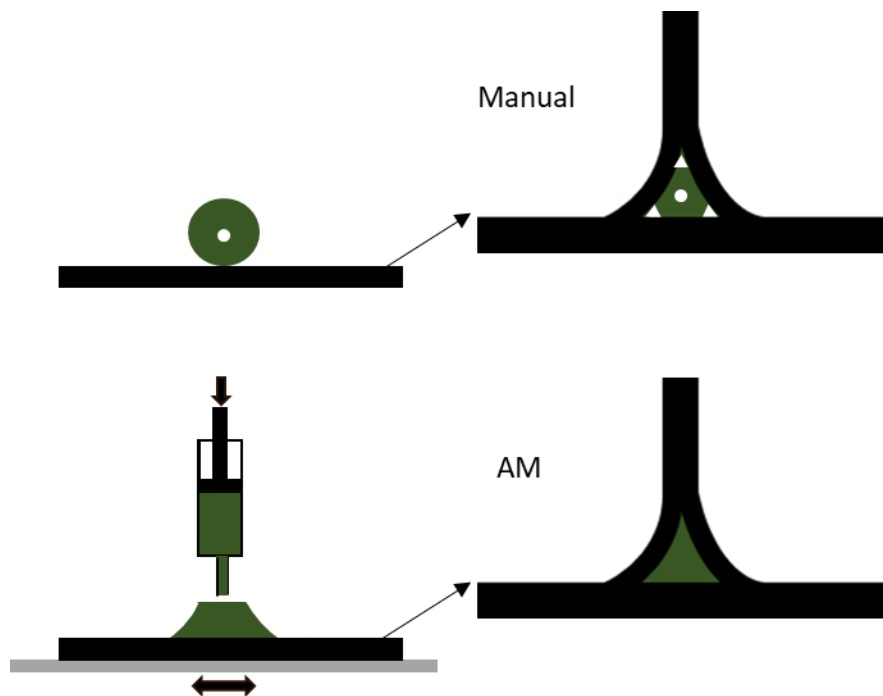
Figure 34: Manually pre-shaped deltoid vs. an AM processed pre shaped deltoid. AM T-joints have better geometrical accuracy and less porosity.

The work by Niese et al. [133] assessed the feasibility of using powder bed fusion to tailor the adhesives in both deposition patterns and in its physical properties, such as electrical conductivity. However, the authors warned of high porosity in the materials due to the process.

The work by Schmidt et al. [32] completed the previous works [47,48,133] by assessing the effect of various deposition strategies on the physical and mechanical properties of UV and thermally cured adhesives. Schidt et al., changing the AM process, were able to overcome the limitation of SLA and manufacture flawless bond lines, confirming the results obtained in [47]. The aim of the work is the same presented by Niese et al., which is to create a single process for the manufacture of complex mechanical, electrical and optical conductive systems using AM and direct printing. The authors designed a custom-made setup in order to evaluate the effect of build direction, the edge along which the layered adhesive stacking is performed, the raster angle and the deposition pattern of the material in the single layer, on the physical and mechanical properties of adhesives processed via 3D printing. The investigated adhesives were five dual curing, four commercial solutions, epoxy/acrylate Loctite 3217, acrylate Loctite Eccobond UV 9052 (Loctite Corporation, Düsseldorf, Germany), polycarbaminoacid Delo Dualbond AD346 (Delo Industrie Klebstoffe GmbH & Co. KGaA, Windach, Germany), and one experimental epoxy adhesive. All adhesives contained particles that provide them with thermal and electrical conductivity. Reference values were obtained for the mechanical properties using specimens fabricated in a jig and using a single cycle cure adhesive, the Dellomonopox GE7985 epoxy (Delo Industrie Klebstoffe GmbH & Co. KGaA, Windach, Germany). Analysis on the experimental results showed that the different raster orientations do not have a significant effect while the build direction does, leading to strength increases of up to 70%. Observing the fracture surfaces allows us to understand that a longer UV pre curing period enhances the layering effect, anisotropy and particle deposition, with a positive effect on thermal and electrical conductivity. It is worth noting that the rheological behavior of investigated adhesives was shear thinning, which means no flow at rest, and that UV pre curing enables high geometrical details without support and non-dependent build direction. These characteristics are relevant for manufacturing components with complex geometries.

Sekiguchi et al. [33] applied a strategy that combines the adhesive deposition process proposed by Redmann et al. [47] and the work of Kuman et al. [41] for adhesive modulus tailoring along the bondline (Figure 35). These techniques were applied to manufacture SLJs that were later tested under static and low-cycle loading. The authors took advantage of a characteristic of the second-generation acrylic adhesives, where varying the mixing ratios of the two base agents can lead to different mechanical properties. Using agents with different mechanical properties after curing, the stiff G672-ISP and the

54

flexible LDC-141 (Denka company, Tokyo, Japan), in four different ratios 4:6, 5:5, 6:4 and 7:3, the authors were able to tailor the adhesive bulk properties, from 3.72 MPa, 9.06%, 13.8 MPa to 13.7 MPa, 2.81%, 19.5 MPa respectively for elastic modulus, stress at yield point and strain at yield point
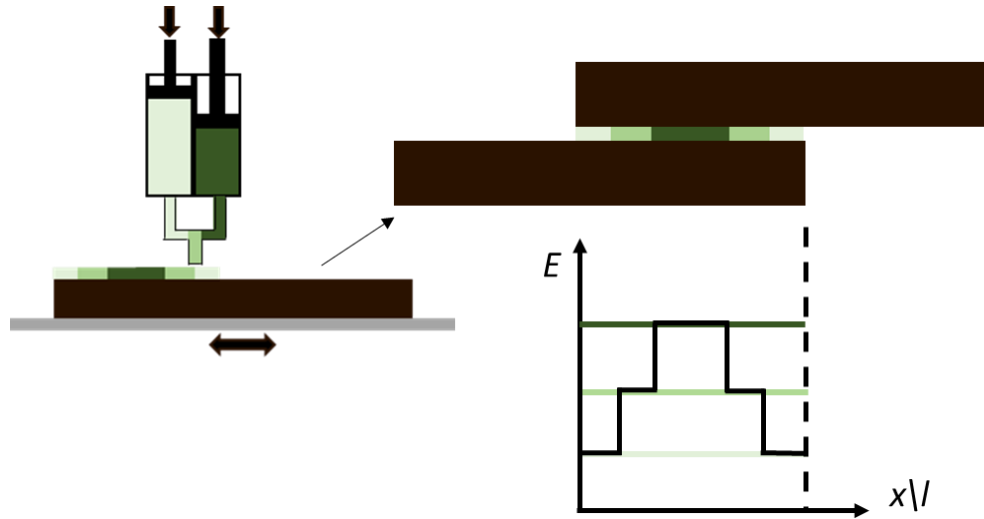
Figure 35: Adhesive modulus tailoring using a stepwise design strategies and second generation acrylic adhesives [33].

To control the mixing ratio of agents during the adhesive deposition at the overlap, a special apparatus was purposely developed [134], making use of a concept already in use for 3D printing of clay and concrete [135], where the extruder is replaced by an adduction system that allows us to extrude fluids for the liquid deposition modelling process. Using this apparatus, flexible adhesives were extruded at the end of the overlap end while a stiff adhesive was extruded at the overlap centre. This is achieved by increasing the volumetric content of the stiff agent every 5 mm along the overlap length, creating a SLJ with tailored adhesive properties. Reference SLJs were manufactured with the same geometry and non-tailored adhesives using the two extreme values of the mixing ratio (the stiffest and the most flexible). Specimens with the graded adhesive outperformed the flexible and stiff non-tailored adhesive joints in quasi static testing, with an increase in failure load of 16.3% and 21.4%, respectively.

While tailoring the adhesive properties along the overlap was already proven to be an effective solution to improve the performance of bonded joints [122], AM processes could be extended to other aspects of a bonded joint to further improve performance. This can be achieved with a finer control over the final geometries, adopting voxel-oriented material tailoring, enhancing reproducibility and lowering the

porosity in the adhesive. The next main challenges will be in engineering the proposed methods for different adhesives and different scales, from large aircraft wings [40], integrating the deposition of the long fiber reinforced matrix, to micro scale, electronic applications using new tailoring approaches such as the one presented in [136] where a patterned adhesive, controlled by droplets in size from 0.5 to 6.0 µL, outperformed a continuous adhesive with an increment of ~70% in shear strength.

2.2.4 Overlap tailoring AM enabled to improve the joints performance

This sub-section presents and summarizes works which aim to improve the performance of adhesive bonded joints performance with an optimized geometrical design of the adherend in the overlap area. The approaches presented here were often originally proposed for laminate materials [123,137], which have many similarities to AM processed components, such as a layering effect and an anisotropic behaviour under load [77].

The AM design strategies to increase the bonding area or to modify surface properties, presented in this section and those that follow it, are shown in Figure 36. At macro-scale, adherend modifications can be achieved by including features such as pins or wavy interfaces. At micro-scale, AM process parameters, such as layer height or nozzle temperatures, can be used to finely modify surface properties, leading to changes in the morphology. Some surface modifications suitable for industrial contexts were also investigated
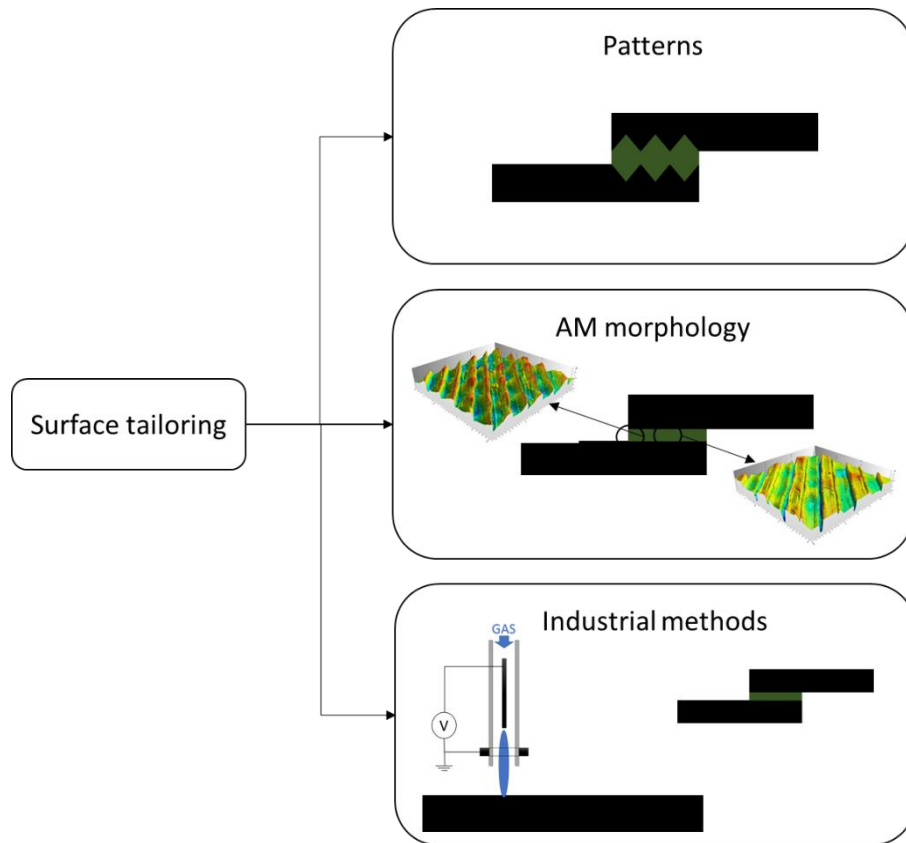
Figure 36: AM design strategies for tailoring the adherend at surface overlap.

Spaggiari et al. [21] explored the effect of a sawtooth patterns applied at the overlap area, generating the geometry while manufacturing specimens with FDM Stratasys process (Figure 37). ABS was used for the specimens as well as a variety of structural epoxy adhesives with slightly different elastic moduli. The authors investigated the effect of zig-zag patterns with different orientations, (0°, 45°, 90°) with respect to the loading direction and compared the output with a monolithic reference SLJ. Data analysis revealed that the adhesive stiffness is the only relevant effect in the investigated configuration, as the joints assembled with ductile adhesive outperformed all others. Furthermore, it is worth noting that ABS polymeric adherend and epoxy resin bonding does not require additional surface modifications besides solvent cleaning. Failures were always cohesive in the adhesive or in the adherend. Thus, the sawtooth morphology is to be discarded as its shape does not provide mechanical interlocking and is in fact a stress concentration feature. However, it still has some practical potential as a shape optimization for this kind of AM patterns at overlap has yet to be published in the literature.

Figure 37: AM adherends with enhanced bonding area in the adherend volume [21].

Cavalcanti et al. [24] expanded upon the work of Spaggiari et al. [21] by investigating the effect of sinusoidal tailoring of the overlap coupled with different building directions. The authors, using fused FFF, built PLA adherends in two different directions, flat wise and edge wise, and manufactured SLJs using an epoxy adhesive. A good degree of compatibility between the PLA polymer and the epoxy resin was observed, as all joints had failure in the adherends. Additional remarks were drawn by observing the failure surfaces. Specimens built in the flat wise direction or with a standard overlap geometry presented delamination failure, while the specimens built in the edge wise direction or with a sinusoidal overlap presented failure through the thickness, illustrating that component placement can strongly affect the mechanical properties of layered constructions [67].

Garcia-Guzman et al. [30] investigated the effect of the structured interfaces seen in the previous works by Spaggiari et al. and Cavalcanti et al. [21,24] using DCB testing. This experiment was carried out to determine that morphological patterns on the surface of the adherends influence the fracture toughness. The authors parametrized a recurrent trapezoidal pattern as a function of discrete values of amplitude, wavelength and aspect ratio. Tests carried out on PA glass fiber reinforced adherend, manufactured with a MarkOne (Markforged, Watertown, MA, USA) 3D printer and bonded with structural adhesive, led to an increase of the critical energy release rate from 100% up to 800%, when compared to the flat DCB configuration. An analytical model was developed to understand the physics of the fracture process and to support the selection of the optimal pattern configuration. It was observed that the tooth morphology increases the effective bonding area and modifies the direction of the crack propagation as a function of the tooth slope. Under the hypothesis of constant strain rate, it was possible to distinguish between the energy dissipated at the flat part of the trapezoidal tooth and the energy dissipated at the slope and to use a failure criterion derived from the Benzeggah-Kenane one [138]. Correlating experimental data to the components of the dissipated energy showed that a higher amplitude to wavelength ratio corresponds

58

to higher fracture toughness. This is related to a change of the fracture from pure Mode I to mixed mode which forces crack propagation to travel longer distances along the vertical and horizontal directions and thus absorbs more energy.

Garcia et al. [22] investigated the effect of an AM tailored macro pattern on an adherend that protrudes into the bonding line (Figure 38). The authors used the FDM process to create a tailored texture on carbon fiber-reinforced polymeric (CFRP) adherends with the AddJoining method [116]. This approach has the advantage of being compatible with a wide range of materials and works with any adherend, independently of its manufacturing process. The effect of different spacing of ABS reinforcements, having uniform trapezoidal cross sections along the width and height similar to the adhesive layer thickness, was numerically modelled and experimentally validated. The numerical analysis pointed out that the reinforcements modify the stress distribution. Experiments quantified the positive effect of the macro pattern on joint performance, changing the failure mode from adhesive to cohesive and attaining a minimum performance improvement of 43%. For every reinforced configuration studied, an increment in strain was found.
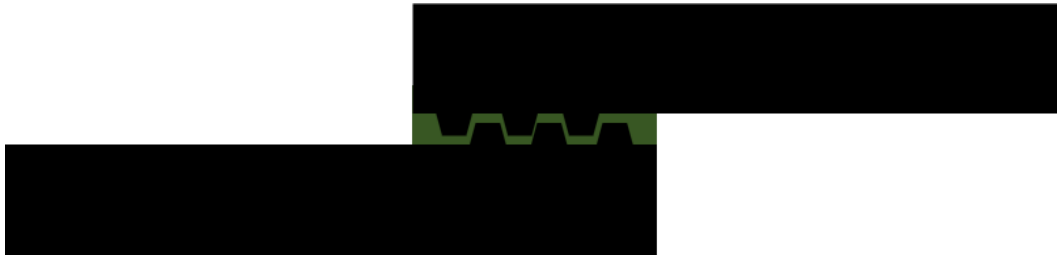
Figure 38: Adherends with a AM deposed pattern at the overlap in the bondline volume [22].

Bürenhaus et al. [23] investigated different tailored overlap configurations, such as the scarf joint, the finger joint and the tongue-groove joint against more standard joint geometries such as the SLJ, butt joint and T-peel joint. Specimens were manufactured and numerically modelled, using a composite-like material approach presented in [77]. The authors compared the results of these approaches to the results obtained with a reinforcement pattern on the surface designed as presented in [22] by Garcia et al. Adherends were manufactured in the various geometries using FDM with PEI material. The adhesive used (Loctite LM-21 HP) had excellent compatibility with PEI without surface treatment. Preliminary screening with SLJs showed cohesive failure in the adhesive. The base geometry was designed according to DIN-EN-ISO 1465 [139] with a thickness of 1.778 mm, width of 25 mm and an overlap of 12.5 mm. Experimental testing confirmed the dominant effect of changes in the geometrical configuration on the texture

obtained by the manufacturing process. The maximum joint strength of 35.45 MPa was achieved with the butt joint configuration, while T-peel had the lowest joint strength value with about 13 MPa. Among the joints with tailored overlap geometry, the scarf joint had the best performance improvement of about 66%, despite an almost unchanged overlap area. In the specimens manufactured according to the work of Garcia et al. [22], adherend failures occurred at low loading due to stress peaks at the pattern locations.

Data on the effects of overlap tailoring provided by the previously described works have been completed by the investigations carried out by Fieger et al. [38] on tailoring using 3D and 2D pattern geometries with constant cross section along the adherend width. Four different patterns were designed to address the low adhesion of adhesives to PA. The design takes in account different overlap tailoring strategies, namely maximizing bonding area using coupled protruding-hollow dimple-shapes, modifying the bondline with 2D structures equally spaced along the overlap, seeking mechanical interlocking of adhesives in the adherends using undercut or between adherends with snap fastener like structures. The SLJ results, in agreement with the results from Spaggiari et al. [21], indicated a beneficial effect of increasing the bonding area. The tensile shear strength increased by 44% with respect to flat-standard SLJ. The 2D structure in the bondline was found to be unsuitable. This result is in apparent disagreement with the findings of Garcia et al. [22] but could be explained by the different and uniform spacing of the AM structures in the bond line. Finally, the maximum improvement in tensile shear strength is achieved with the configuration that combines adhesive bonding and mechanical interlocking between the adherends, indicating that this design strategy should be the target of further research.

The use of mechanical interlocking in AM bonded joints is still an open topic of research and few works are available on this specific subject, even if it seems to have a mostly positive effect on joint performance. This is probably due to the limitations on buildable geometries and the geometrical tolerances achievable with current AM processes. However, recent studies on the effect of the placement and AM process developments are now enabling these novel design strategies. An example of mechanical interlocking applied to AM bonded components can be found in the work of Jilich et al. and Frascio et al. [140,141], where pins were used for adherend alignment, adhesive thickness control and to create a snap-like connection. Another relevant work on the design of AM snap connection for AM can be found, although without the use of adhesive bonding. Rossing et al. [142] addressed the low compatibility between silicones and other materials with mechanical interlocking and MMAM, devising a solution that dispensed the use of primers. Possible future works could focus on assessing the feasibility and the effectiveness of adopting AM joints solutions previously investigated for other processes and materials, such as pinning, tapering or filleting with integrated design in the AM tailored adherends.

2.2.5 Surface modifications for additively manufactured adherends

This sub-section reports works that focus on surface modifications in AM joints, carried out in order to obtain performance improvements. According to Packham [51], adhesion mechanisms are described by three main supporting theories; the absorption theory that focuses on the correlation between wettability and covalent and van der Waals forces, the mechanical theory that focuses on the mechanical interlocking that occurs when the adhesive penetrates in the adherend morphology and, lastly, the diffusion theory that is based on polymer chain dynamics and the compatibility between the different polymers. It is worth noting that, at time of writing, recent literature [143] is questioning the chemical effect of surface modifications on bonded joints performance, pointing out that performance variations could be only correlated to the morphology modifications at nanoscale.

AM offers the possibility to implement integrated surface modifications. This can be done, for example, by mounting an atmospheric plasma torch on the nozzle or to affect the surface properties through the printing setup.

An AM integrated approach was first presented in the work of E. Dugbenoo et al. [29], where the authors increased the effective bonding area by using the air gap AM process parameter (Figure 39).
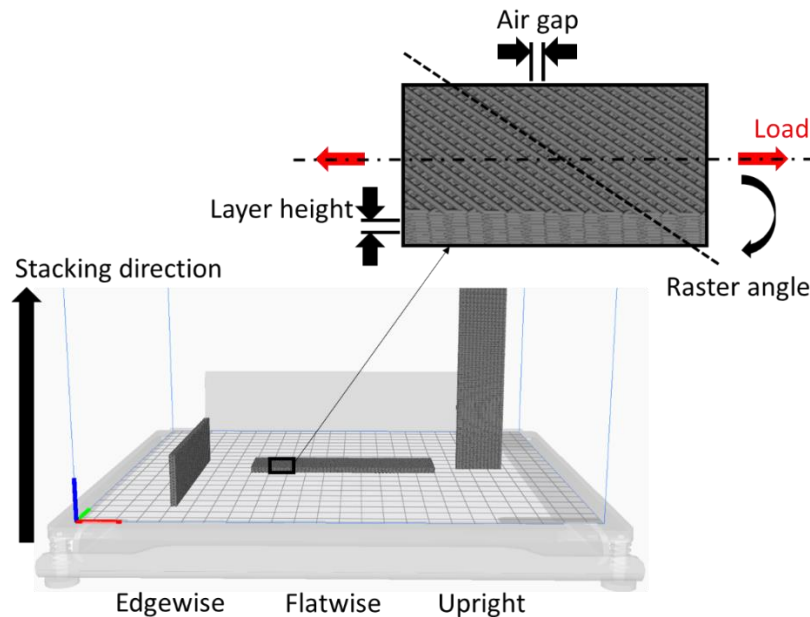
Figure 39: Overlap modifications through the parameters of build setup, investigated in [23,24,26–29].

By setting a partial infill at the overlap interface, while compiling the G-code programming language, it is possible to obtain optimal surface morphology avoiding post processing. Thus, it is clear that this approach could be advantageous for a reduction of production costs. By setting an offset of ~120 μm in the material deposition pattern (air gap), the authors obtained a 50% infill density at the adherend–adhesive interface that led to the increase of the bonding surface area by ~150% and enhanced the interlocking effect. To assess the effect of this design on actual joints AM SLJs were manufactured with printed adherends composed of long fiber, carbon, Kevlar and glass, reinforced PA matrix supplied by Markforged. SLJs were manufactured using a two-component epoxy adhesive (EM9500 and EM9520, Kumho P&B Chemicals Inc., Seoul, South Korea) to join mechanically abraded and air gap tailored adherends. Experimental data identified a joint strength increase of up to ~145% and a joint toughness increase of up to ~820% for tailored joints, values which are dependent on the nature of the material being used as reinforcement.

Fieger et al. [38] experimentally evaluated the effect of four different surface treatments on powder bed fusion processed PA adherends. Adherends were treated with flame treatment, corona treatment, atmospheric plasma treatment and chemical etching treatments and then used to manufacture bonded joints with four different adhesives. SLJ testing highlighted changes in the failure mode from adhesive to cohesive and an improvement in tensile shear strength. Maximum tensile shear strength was measured for flame treated SLJs with an improvement of over 80% with respect to the reference. It must be noted that the results have large dispersion, suggesting low process reproducibility.

Leicht et al. [37] investigated the effects of the construction direction (Figure 39) and surface modifications on the tensile strength of adhesive bonded joints made of powder bed fusion processed PA adherends and epoxy resin. Adherends were fabricated with a geometry compliant to the Centrifugal Adhesion Testing Technology (CATT) procedure described in [144], that uses a centrifugal force to apply the load and satisfy DIN-EN-ISO 15870 standard [145]. Three different epoxy adhesives with different mechanical properties were investigated, DELO-DUOPOX SJ8665 (DELO Industrieklebstoffe GmbH & Co. KGaA, Windach, Germany), 1277 (Sika Schweiz AG, Zurich, Switzerland) and Easy-Mix HT 180 (WEICON GmbH & Co. KG, Muenster, Germany). The joints were fabricated with adherends subjected to chemical smoothing, atmospheric pressure plasma (APP) and the combination of the two treatments. Untreated substrates were also used as a reference. Experimental testing showed that both adhesives had a similar response to the surface modifications under tensile loading, with a decrease in tensile strength after chemical smoothing, but increase after APP and after the combination of the two treatments. To understand why chemical smoothing has a negative effect on the load-carrying capacity of the joints, the authors performed CT scans on the specimens. This analysis demonstrated that chemical smoothing

erases the porous morphology resulting from the melted powder particles, preventing mechanical interlocking between the adhesive and adherend. A maximum tensile strength variation of 300% was found with respect to the non-treated configuration.

Bürenhaus et al. [23] investigated the effect of different surface modifications using industrial treatments and the build parameters of the AM processed (Figure 39) PEI adherends. The tested industrial modifications were ethanol cleaning, abrasion using P80 sandpaper, blasting with glass beads and APP. The raster orientation was selected in order to assess the effect of the directionality of the AM surface texture with respect to the loading direction, 0° parallel to load direction, 45° baseline orientation and 90° orthogonal to the load direction. WELDYX Polyplast acrylate resin (GLUETEC Industrieklebstoffe GmbH & Co., Greußenheim, Germany) and DELO-PUR 9694 polyurethane were selected for this study because they generated adhesive failures without treatment. Experimental data demonstrated that ethanol cleaning and mechanical abrasion are ineffective, while APP and blasting provide similar results with SLJ shear strength improvement of about 110% with respect to the untreated configuration. Surface modifications created using the AM build parameters have the advantage of being directly integrated in the manufacturing process, but they negatively influence the mechanical properties. The authors tailored only the top layers in order to minimize possible interaction effects, but delamination occurred when increasing the airgap to 0.5 mm. The authors pointed out that the use of the scarf joint, coupled to the design freedom of AM, allows one to easily achieve overlap tailoring in these geometries, leading to excellent performance with regard to the maximum transferable forces and reaching utilization factors of over 80%.

Li et al. [25] investigated the effects of mechanical abrasion and APP on adherends made of high performance AM processed polymers (PEI, PEEK) and carbon fiber reinforced PEEK using two different adhesive technologies, a film solution by 3M (AF163-2) and a liquid solution by Henkel (Ea9380.05). The adherends were manufactured using an FFF printer with a geometry according to GBT 33334 standard [146]. Scanning Electron Microscope (SEM) and confocal laser scanning microscopy (CLSM) assessed that the typical stripe-like morphology generated by FFF was erased by the sandblasting treatment, leading to uniform value of surface roughness (*Ra*) while the use of APP led to almost no changes. SLJs were fabricated and tested according to ASTM D5868 [147] using solvent cleaned, sandblasting and APP treated adherends. Data from mechanical testing demonstrated the necessity of a proper surface treatment, as the failure surfaces of solvent cleaned substrates were always adhesive in nature. The PEI adherend reached the maximum shear load after sanding and APP, with mixed adhesive cohesive failures, while

PEEK and carbon fiber-reinforced PEEK reached the maximum shear load after APP, with increments up to + 400%.

Yap et al. [31] investigated the effect of curing the assembled AM SLJs using a thermal cycle. The application of heat can be beneficial, accelerating adhesive cure, and improving mechanical performance. It enhances the phenomena of crosslinking in the adhesive and of diffusion between the layers of the AM adherends. Materials selected to build the adherends were two different engineering polymers, the UV resistant ASA and the CFRP PA. Two adhesives suitable for bonding polymers were selected, the slo-zap cyanoacrylate by ZAP (Ac Marca, Barcelona, Spain) and E-20 HP epoxy by Loctite. Adherends and monolithic SLJs, used to set reference values, were manufactured in compliance with ASTM D3163-01 [148] and ASTM D1002-10 [149] using FDM. The adherends were prepared with two different surface preparations, solvent cleaning and mechanical abrasion, while the SLJs were cured at room temperatures and at 80 °C. For both materials, the maximum tensile load was achieved in the monolithic configuration. SLJs bonded with the cyanoacrylate adhesive always showed cohesive failures, maximum strength of bonded SLJs was obtained for the solvent cleaned surface with 1.7 and 2.7 kN, respectively for ASA and PA, because the heat cycle led to adhesive degradation. On the other hand, SLJs bonded with the epoxy adhesive always failed adhesively, indicating an inadequate surface preparation for structural applications. Indeed, after heat treatment the PA SLJs reached a maximum shear load of 1.7 kN, 2.5 times lower than monolithic reference value.

Kovan et al. [26,27] used FFF to manufacture SLJs and butt-joints with PLA substrates to experimentally assess the effect of changing printing orientation and layer height (Figure 39). The authors design strategy is based on the observation that AM parameters affect the component quality, and in particular the surface morphology [150–152]. This can be used to enhance the mechanical effect of adhesion [51,153]. Adherends were designed according to ASTM D3165 [154] for the SLJ geometry and according to ASTM D2094 [155] for the butt joint geometry in three different layer stacking directions, upright, edgewise, flatwise and with three different layer heights, 125, 250 and 500 μm. Preliminary mechanical characterization showed that the stacking directions of the layers affected the material modulus though diffusion quality and roughness orientation. Each of the joint configurations had a distinct optimal setup to maximize the load carrying capacity. The maximum shear load for SLJs was achieved for the edgewise direction and 250 μm layer height with a performance improvement of 200% with respect to the worst configuration (edgewise direction and 500 μm layer height). For the butt joint, the maximum load value was obtained for the minimum layer height with an improvement of 640% with respect to the lowest load

value measured using adherends with maximum layer height. The authors pointed out that build time and maximum joint load are non-linearly correlated to the levels of the investigated factors.

Kariz et al. [28] investigated the effect of the 3D printing setup on the adherends' morphology for heterogeneous polymer-wood joining. Using FFF equipment and ABS filament, the authors created SLJ adherends, designed according to EN 205:2003 [156], with three different layer heights(Figure 39), 90, 190 and 390 μm. A reference was set using the same 3D printed adherends and erasing the surface morphology by acetone vapor chemical smoothing. SLJs were assembled without further surface modifications using three different adhesives, Mitopur E45 PU1K (PU 1K; Mitol d.d., Sezana, Slovenia) and Bison Power (PU 2K; Bison International, Goes, Netherlands) polyurethane adhesives, and DORUS KS 217 hot melt adhesive (HM; Henkel, Düsseldorf, Germany). Analysing the shear strength of the different SLJ configurations some remarks can be drawn. The Bison Power adhesive had the highest shear strength in each configuration while Mitopur E45 had the lowest. Acetone smoothed specimens had the lowest overall shear strength, showing that the AM derived morphology has a positive effect.

2.3 Discussion and general remarks

Recent developments in additive manufacturing processes and in innovative materials have expanded the use of additively manufactured components to many new engineering fields, leading to an increased interest in the use of this technology. In particular, the joining of additively manufactured components has been a key area of study, as this technology is essential for manufacturing structures of increased complexity.

Different design strategies have been investigated to take advantage of the beneficial effect of voxel size control provided by additive manufacturing on the geometry and material properties.

Most works focused on additively manufactured adherend tailoring. Kumar et al. [40,41] and Khan et al. [42,43,125] in their works modelled the stress distributions of joints using functionally graded materials achieved with digital materials and Ubaid et al. [44] experimentally assessed load carrying and toughness improvements due to a modified strain field distribution in the bondline using single lap joints and digital image correlation.

Other authors focused on the so called geometrical-complexity-for-free provided by additive manufacturing processes and used tailoring of adherends at the bonding interface and in the thickness. The first approach is used to create a desired pattern able to provide mechanical interlocking and increase the area at the interface between adherend and adhesive. Several authors [21,24,29,30] used geometrical patterns indented in the adherend thickness to maximize the overlap area, while others [22,40] used patterns protruded in the bondline to seek mechanical interlocking and to alter the strain distribution in the adhesive.

The second approach draws inspiration from organisms which show high adhesion and toughness. Using a fracture mechanics-based approach, several authors [34–36,131] developed through the thickness structures able to delay crack propagation and the failure of the joints.

The results of these works provided the first quantification of the effects of tailored additively manufactured adherends and highlighted the advantages and disadvantages of this design approach. Major limitations are due to the minimum size of the printable features, inherent to a given additive manufacturing process specifications, and the effect of the tailoring on the adherend stiffness. Indeed, an unsuccessful tailoring procedure can increase the susceptibility to bending, leading to increased peel stress in the bondline and causing failure at loads lower than that of a non-tailored joint configuration.

New developments in additive manufacturing processes, such as the multi material additive manufacturing and the use of new materials, are enabling different design solutions, such as the creation

Joints designed for Additive Manufacturing

of functionally graded adherends or embedded sensors, although they urgently require the development of new testing methods and standards to address the resultant complex material response. Available results indicate that this approach can improve joints performance, although it is still common for joints manufactured using additive manufacturing technology to fail predominantly by adhesive failure, pointing out that further performance improvements can be achieved by improving the quality of surface treatments and material compatibility.

A possible solution for these limitations could be the combination of several different design approaches for the manufacture of the adherends or the use of surface modifications. Some of the studies applied surface modifications which are already in industrial use [25,31,37,38], while others [23,24,26–29] explored that the printing parameters affect the physical and the mechanical properties of the polymeric adherends. Plasma treatment was assessed as the most effective surface modification for this purpose as it is suitable for use in hollow structures and has the potential of being process integrated. For example, an FFF printer can include a plasma torch on the nozzle. On the other hand, while tailoring the printing parameters does not require any additional equipment or post processing, it can be a highly complex process, as the interaction between different parameters can lead to unexpected and undesirable results.

Some authors explored the feasibility of using additive manufacturing to tailor the bondline by controlling the adhesive composition or shape [32,33,47,48,133]. The main benefits of this approach are the compatibility with non-additively manufactured adherends and the improved joint quality, as the adhesive layer is relatively free from porosities and possesses high geometrical accuracy and reproducibility. Such local control has the potential to enable the manufacturing of true functionally graded adhesives by controlling adhesives composition, adhesives mixing, or the dispersion of reinforcements in the adhesives. This concept has been successfully demonstrated in laboratorial settings, but no commercial solution is available at the time of writing this chapter.

Finally, tailoring additively manufactured adherends and adhesives, following a design for additive manufacturing approach, has proven to be an extremely useful, yet relatively unexplored, solution to improve the performance of adhesively bonded joint. While many researchers have laid the foundations for more extensive use of additive manufacturing in conjunction with adhesive bonding, additional research is still required to enhance manufacturing reliability and repeatability. Another important conclusion of this chapter is that aspects related to the degradation and long-term durability of polymeric additively manufactured bonded joints are relatively unstudied. This represents a topic of great interest for industrial applications and must certainly be an important subject of research in the coming years.

Chapter 3

Design for additive manufacturing - Case of study

This chapter is based on papers [140,141] and presents that a robotic gripper specific for grasping and handling of textiles and soft flexible layers can be miniaturized and improved applying polymeric design for Additive Manufacturing. The outcomes are a lower complexity of the design overall and lower number of components. These are pursued taking advantage of the anisotropy of the AM processed polymer and assigning appropriate shapes and linkages in the mechanisms. Adhesive joining is performed assembling the optimized shapes in order to overcome constraints on the geometry.

3.1 Background and motivations

This chapter presents the case of study design of a cost-effective gripper for AM starting from the expertise previously gained in the EU research FP7 project Clopema [157,158]. The Clopema project aimed to advance the state of the art in the autonomous perception and manipulation of all kinds of fabrics, textiles and garments.
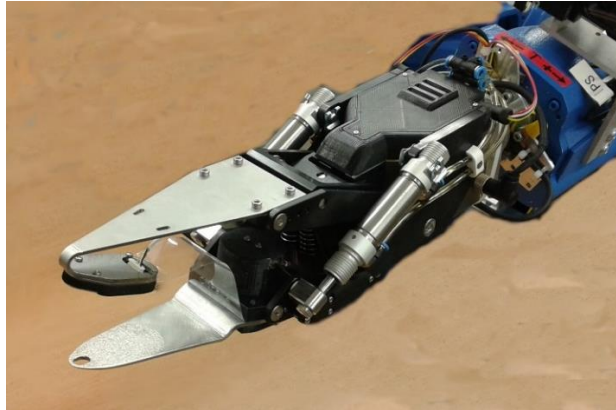
Figure 40: Clopema gripper on Yaskawa Motoman MA1400.

The Clopema gripper (Figure 40) was designed for picking non-rigid items, an unconventional application that still does not find standard solutions. The output is covered by the US patent US 9089973B2. The aim was to apply the DfAM to obtain a new design focused on taking advantage of AM benefits with the Clopema gripper. A practical case of exploiting the advantages of AM using dedicated design rules as the reduction in part count through integration of functions in the geometries is presented [159]. The new developed gripper focuses on an application with a limited payload and the target of minimum overall size despite embedded actuators, controller and textile identification sensing with Clopema tactile sensor as design requirements. Adhesive bonding is performed to assemble the optimized AM components. Finally, from the information and from the data provided in this and the previous chapters, relevant research topics are identified and then investigated in following chapters.

Design for additive manufacturing - Case of study

3.2 DfAM applied to the Clopema Gripper re-design

3.2.1 Design requirements

The Clopema grippers are designed to manipulate clothes, fabrics and any other flexible materials. As stated in [157] the kinematic of human hand is the primary template for the adopted gripper architecture. Interferences with hard surfaces during the picking are the important issue to consider. A compliance in the hand design prevents the gripper components from overloads. The opening stroke is selected to ensure that a target items can be grasped and to accommodate for the errors of the vision system. The range of the picking force must guarantee secure holding of the garment without any damage. The function of the fingers is not only to move clothing but also to support the cognitive system by providing tactile sensing information. Data are collected while slipping the two gripper tips, an approximation of the human like finger rubbing movement: the precision and comparability of the acquired data are dependent on the regularity and repeatability of the rubbing movement.

3.2.2 DfAM applied to the kinematics of the gripper

The kinematic chain of the original Clopema gripper (Figure 41) has two sub-chains. The first is the outer mechanism, a (variable) four-bar linkage, comprising joint J1, J2, J3, J4 (black colour) with the two fingertips. The second, the inner mechanism (grey colour J5, J6, J7), moves joint J4 using the coupled actuated sliders A1 as actuation. The outer mechanism is free to tilt in any configuration of the inner mechanism. This tilting is actuated with actuator A2 connected to the lower finger with joint (J8). The actuator A2 has variable stiffness that permits passive displacement of fingers as reaction to external loads and active tilting that cause relative parallel displacement (rubbing) between the two fingertips when the gripper is in closed configuration (Figure 44). The relatively complicated kinematic of inner sub-chain is due to the need to expand the actuator A1 stroke, which has been chosen as a compromise among those available on the market by analysing general construction factors of the gripper.

Design for additive manufacturing - Case of study
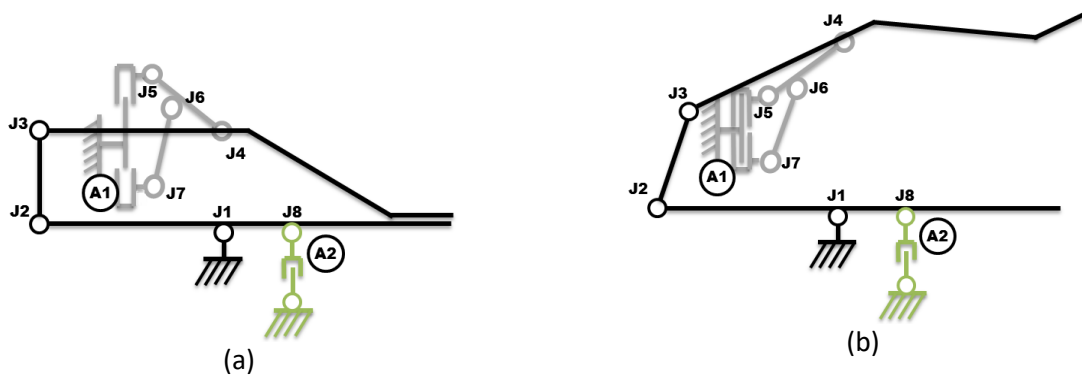
Figure 41: Schematic of Clopema gripper, (a) - closed configuration, (b) - opened configuration.

The new architecture selected to fulfil the same requirements with gripper redesigned for AM is again planar mechanism (Figure 42). The gripper consists of a main frame 1 with interface to the robot and interfaces for all the other components; a tilting motor block 2 with a main linear stepper motor, a micro Direct Current (DC) motor and electronics to drive the motors and identify their position; an upper moving finger 3 and a lower fixed finger 4.
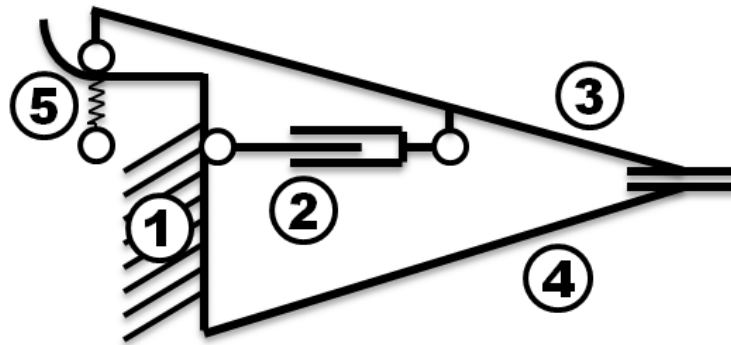
Figure 42: Gripper schematics, 1-Gripper frame, 2-Motor block, 3-Upper finger, 4-Lower finger; 5-Flexible beam.

The lower finger is rigidly connected to the gripper frame. Its fingertip displacement is possible only due to finger body deformation. The shape of the finger body is chosen as a compromise to satisfy different requirements. The fingertip deflection of finger 4 has to be limited to permit the gripping while finger 3 apply a downward force. The force applied on the frame by the displacements of the finger 4 for upward

forces has to be as little as possible to allow the picking from surface function. This characteristic will also prevent rupture from accidental collision with the environment, for instance a table (Figure 43).

<table>
<tr><td>(a)</td><td>(b)</td></tr>
</table>
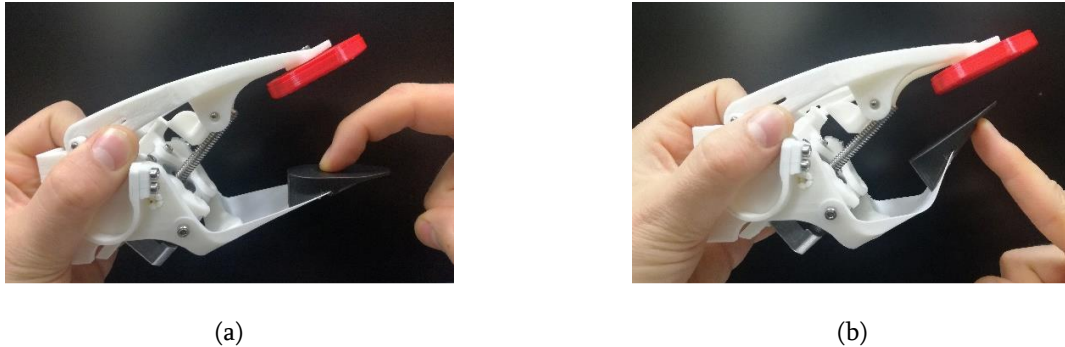
Figure 43: Lower finger loaded with (a) downward force (b) upward force.

The upper finger, rear side, slides over a shaped surface to form a cam coupling. Each side is connected by a pin to a flexible U shaped support that acts as spring and maintains the cam in contact with the sliding surface (one side of the U is fixed to the frame of the gripper while the other side is hinged to the finger). The axis of the pin translates forward and backward along the shaped surface; the position depends on the force of grasp and thickness of the item grasped. When repositioning in the direction of the fingertip (forward), the axis stays in a plane with constant orientation with respect to the gripper frame. When moving backward, the distance between the axis and a mid-plane of the gripper frame increases progressively and non-linearly with the amount of the backward translation. The forward movement allows to execute the rubbing motion with a constant contact pressure between fingertips. (Figure 44). The rubbing movement is performed with the motor block fixed in an appropriate position.
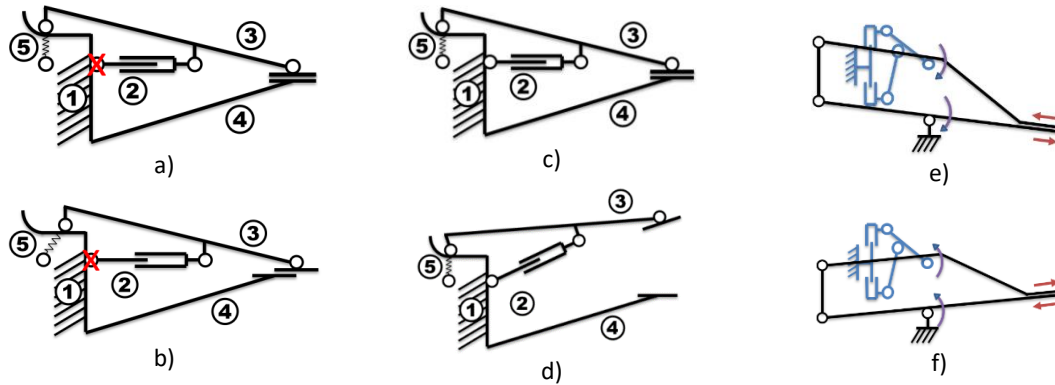
Figure 44: Schematics of the rubbing motion of the gripper with locked joint between frame and motor block (a-b) and the opening motion (c-d); principle of rubbing motion used for original Clopema gripper (e-f).

When the motor block is released to tilt freely, the same motor movement opens and closes the gripper (Figure 44). Instead, the backward movement of the pin occurs when the finger presses a thin object (like a layer of fabric): thanks to this displacement, the contact force on the pressed object increases (Figure 45). The fingertip of the upper finger is connected to the finger body by a flexible hinge and its orientation adapts passively to the orientation of the surface in contact, either belonging to the item grasped or to the opposite fingertip. This adaptation uniforms the contact pressures and it is necessary for the proper operation of the tactile sensor mounted on the fingertip.
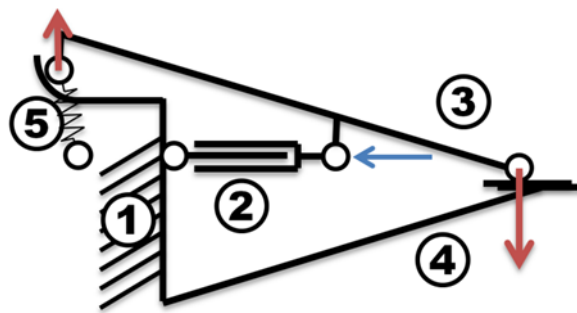
Figure 45: Schema of force transmission due to finger backward motion (blue - motor force direction; red - useful fraction of the reaction force on the finger).

3.2.3 Gripper designed for additive manufacturing assembled using fastening

The original Clopema gripper was designed as set of modular logical blocks (actuators, kinematic chain, upper/lower finger, sensorised fingertip) each of them containing several components. Various modules can be reassembled/combined to adequate the gripper for changing needs. Almost all part was built in CNC turned components. All parts of the new gripper have been designed having in mind the advantages and limitations of the FFF additive manufacturing process. The main advantage is the freedom of shaping, which allows obtaining the desired functional characteristics by exploiting the elasticity of the properly designed components, minimizing the overall size of the gripper and the number of parts of the mechanism. Three are the components designed to deform in a way that performs their intended functions.
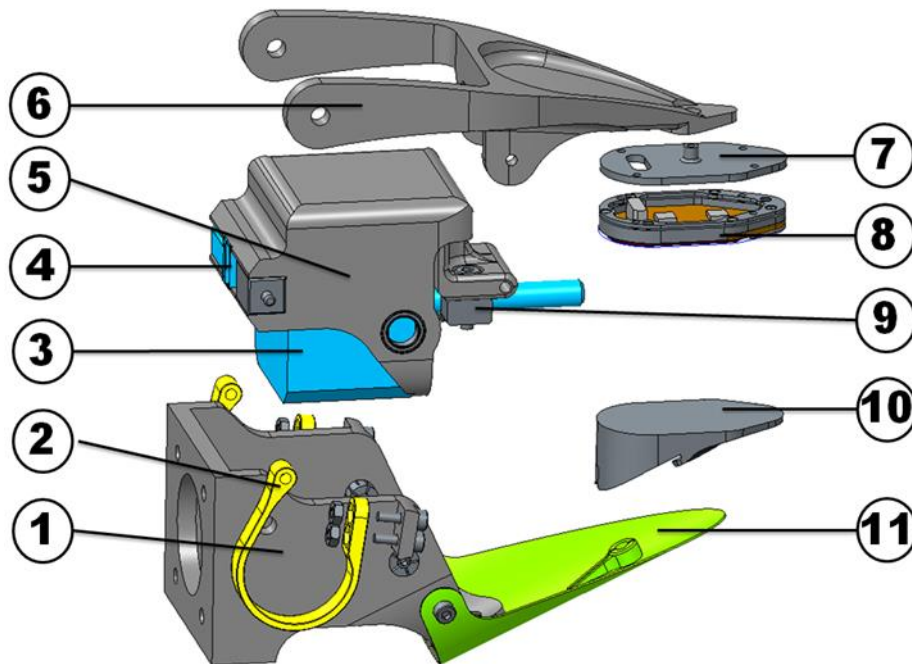
Figure 46: Exploded view of gripper. The numbered components are: 1- main frame; 2- U-shaped spring; 3- stepper motor NEMA17 with lead screw; 4- micro DC motor; 5- tilting motor block with embedded electronics; 6- upper finger; 7- sensor holder with elastic hinge; 8- tactile sensor; 9- slider on the lead screw; 10- lower finger pad; 11 – lower finger.

The lower finger consists of a thin sheet fabricated flat and then wrapped cylindrically and fixed on the cylindrical surface of the finger frame (Figure 47). Once fixed, it maintains its cylindrical shape: any grasping force pointing downward is resisted by the wrapped sheet with minimum deformation; any

contact force finger-table pointing upward results in an immediate and large deformation of the wrapped sheet. This allows to slip under the clothes with the lower finger that has been slightly deformed through the contact with the table. The compliance of the finger protects the gripper and the robot from possible damages caused by small accidental collisions.

a)

b)
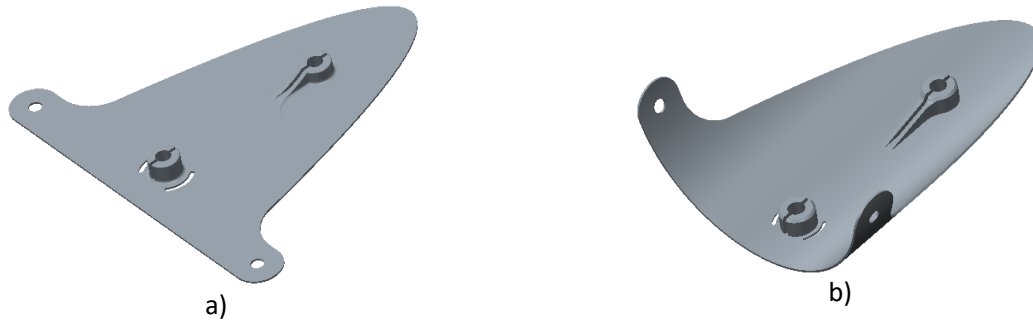
Figure 47: Lower finger: a- the shape of the finger printed by FFF, b- the final shape of the finger wrapped and fixed on the gripper frame, note two expandable pins for quick and save mounting on central plane of the finger.

The second flexible component is the support of the upper finger. The rear side of finger and the frame works as a cam. The flexible component allows the relative movement of these components on defined trajectory permitting the opening and closing of the gripper when the motor block is free to tilt, or the rubbing when the motor block is fixed in horizontal position. When the motor block is free to tilt, the forces acting on the support do not deform it except for the last 5 mm of travel of the lead screw, while the gripper is already closed with the tip of the upper finger in contact with the tip of the lower finger. In this position, the motor force moves the upper finger backward by sliding the back of the finger over the frame curved up. The upper finger tilts. By adjusting this position, one can adjust the gripper gripping force. On the contrary, when the motor block is blocked, the actuation force deforms the support, allowing the horizontal rubbing movement between the fingertips (Figure 48).

76
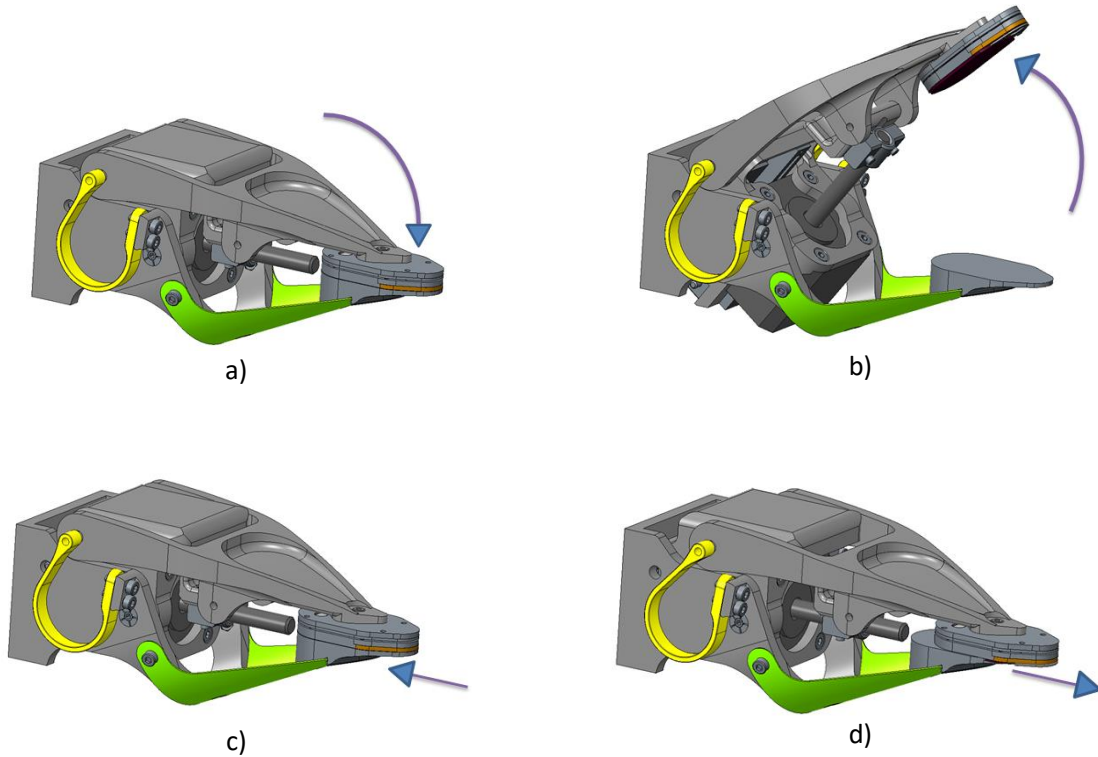
Figure 48: Comparison between the opening and the rubbing motion; a- gripper full closed, b- gripper full opened, c- gripper with motor block locked with finger in maximum backward rubbing position, d- gripper with motor block locked with finger in maximum forward rubbing position.

The third flexible component is the support between the upper finger and the tactile sensor to maintain the sensor parallel to the surface to sense and the contact force uniform along the surface of contact. The typical goal of the rubbing is to classify clothes: slight adjustments of the inclination of the fingertip are enough to obtain proper parallelism between fingertip and material for any thickness of the fabric grasped, so the range of angular adjustment targeted is ±1.5˚.

For the assembly, expandable pins are extensively used. Each of these pins has a threaded hole in the centre: after insertion, a grab screw is screwed to expand the pin into the hole where it gets blocked by friction (Figure 49).
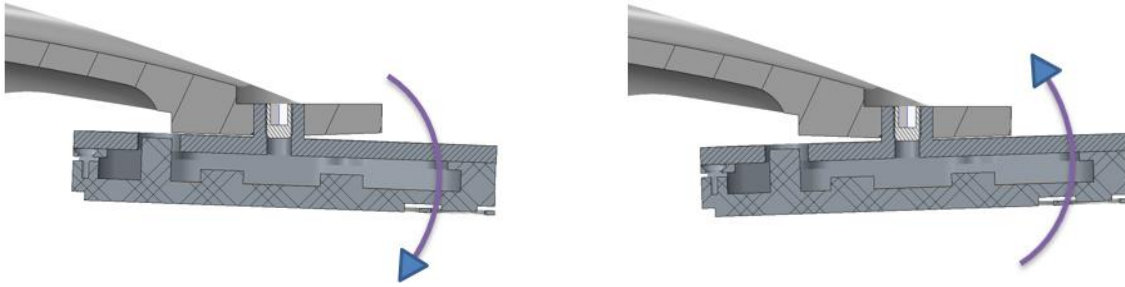
Figure 49: Inclinable upper fingertip with tactile sensor; note the white grab screw inserted in expandable pin.

All the remaining components have been designed to be rigid without major differences compared to the design of the components produced with traditional technologies but for the exploitation of the freedom in shapes. The largest embedded commercial component is the main motor with lead screw. Around the motor is a block that apart from the main motor itself contains a micro DC motor and the PCB with drivers for the two motors, plus a linear potentiometer (Figure 46). The micro DC activates a pin which, inserted in the appropriate hole in the main frame, locks the motor block in the position required for the rubbing. A linear potentiometer has the shuttle fixed to the slider of the main motor: it is used to measure the position of the motor. The motor block is fixed to the main frame through two coaxial pins inserted to the bearings incorporated in the body of the motor block. The upper finger is fixed with pins to the main motor slider and on one side of each U-shaped spring. The finger has a variable section in order to better resist the loads expected in various points of his body.

3.2.4 Gripper with upgraded design for additive manufacturing, assembled using adhesive bonding

The design presented in the previous sub-section (Figure 46 and Figure 47), even if complying with the design input, presented a critical durability issue due to the assembly of the components on the gripper frame. Fastening solution, due to its typical stress distribution, caused premature failure in the AM optimized frame-components coupling surfaces. Therefore adhesive bonding solution was selected on the basis of its improved stress distribution [17] and a modified AM design, dedicated to the bonding joining process, was performed.
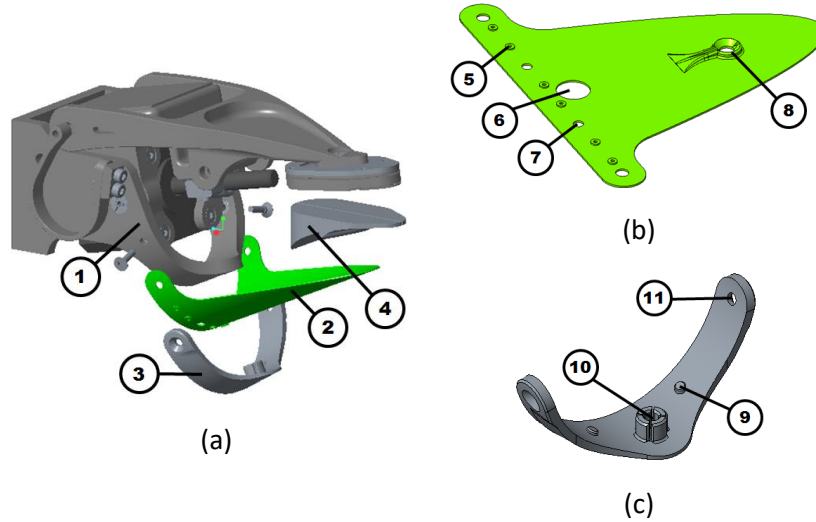
Figure 50: (a) Redesigned gripper: (1) unchanged main frame, (2) redesigned lower finger (bonded to the main frame), (3) additional arc element; (4) lower fingertip. (b) New finger shape before wrapping: (5) spacer to guarantee constant thickness of the adhesive, (6) hole for the central alignment pin, (7) hole for the lateral alignment pin, (8) reinforcement for the screw connection to the fingertip. (c) Additional arc element (9) lateral alignment pin, (10) central alignment pin, (11) hole for the screw connection between the arc element and main frame.

From the literature presented in Chapter 2 it is known that adhesive bonding of AM component is not straightforward, then a dedicated adhesive bonding procedure was studied and tuned. Particularly, two surface modifications were investigated and evaluated using SLJs, i.e. mechanical abrasion and low pressure plasma (LPP) treatments (Table 4).

Table 4: Investigated surface treatments for the AM components.

Treatment	Procedure and parameters
Mechanical abrasion	Cleaned with the Loctite SF 7063 solvent, abraded using SiC grinding paper #320 along the width direction, cleaned
Low pressure plasma	Cleaned with the Loctite SF 7063 solvent, processing gas Air, Power 150 W, Time 180 s, 0.65 mbar

The first step of the assembly process consists in solvent cleaning, important step to avoid weak adhesion and to prevent the low pressure chamber of the Gambetti low pressure plasma machine to be contaminated. Mechanical abrasion was performed using SiC grinding paper #320 along the width

79

direction. LPP was performed placing the components in the low-pressure plasma chamber with the overlap surfaces upward to expose the bonding surface to the ionized gas flow (Figure 51).

Figure 51: Gambetti low pressure plasma chamber.

The adhesive has to be applied on the surfaces to be bonded immediately after the components are taken out of the plasma chamber to maximize the effect of the treatment. Then the parts have to be assembled applying a pressure to obtain a constant adhesive thickness of 0.25 mm taking advantage of the spacers.

Once the adhesive fixing time is elapsed, the curing cycle can be performed in the oven with controlled atmosphere, at the same time as the specimens.

Joining procedure validation was performed using SLJ tests. The adherend specimens have dimensions 100 mm×25 mm×4 mm in the directions, respectively, x, y, and z, according to the ASTM D3163-01(14).

The lap shear joints were realized with 12.5 mm overlap and 0.25 adhesive thickness. This overlap configuration was selected because representative of the overlap configuration adopted in the gripper bonded joint between parts 2 – finger – and part 3 – arc element – shown in Figure 42.

The experimental values of the single lap shear tests are reported in Figure 52. The values were obtained with test speed set at 1 mm/min.
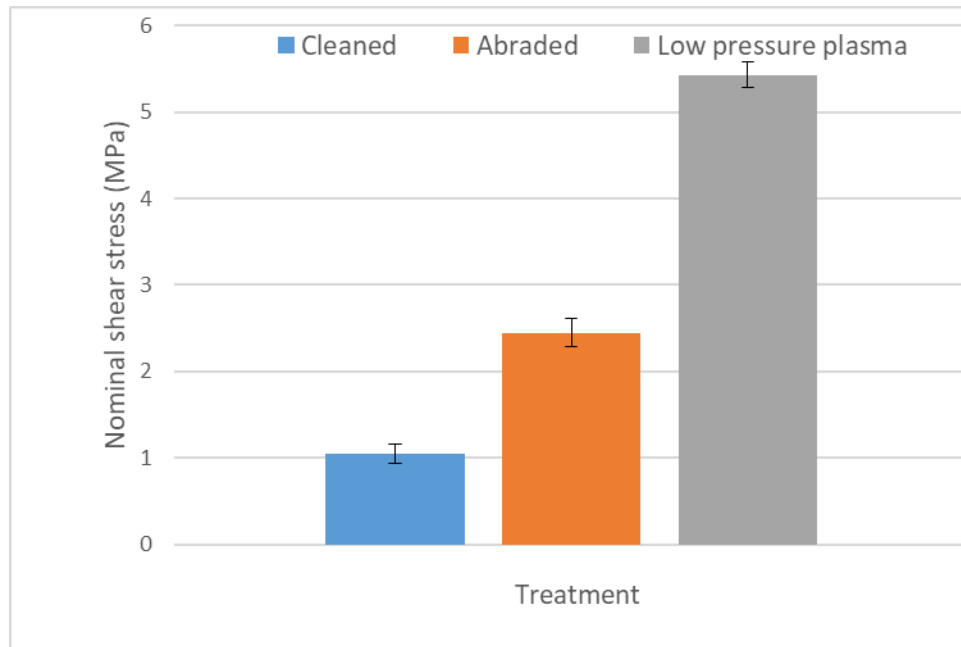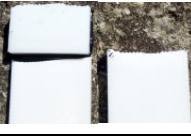
Figure 52: Lap shear tensile test output.

The comparison between the average maximum shear stresses registered during the tests points out that LPP treatment seems the best surface modifications. The failure surfaces are reported in Table 5 for the three cases considered, i.e. solvent cleaned (reference); solvent cleaned, abraded, solvent cleaned again; solvent cleaned and low pressure plasma treated.

Table 5: Failure surfaces after the two surface modifications and for the reference as is from manufacturing (solvent cleaned).

Treatment	Failure type	Failure surface
Solvent cleaned	Adhesive	
Abraded	Mix adhesive and Cohesive	
Low pressure plasma	Adherend	

Adhesive failure occurred in the case of cleaning only. Abrasion treatments improved the performance of the joint (failure type was adhesive) and suggested the possibility of further performance improvement. The low pressure plasma treated joints showed adherends failure: the strength of the bonded joint is higher than the strength of the adherends. This did not permit to analyse the performance of the LPP surface modification but qualified this bonded joint process as the best for this application.

3.3 Components fabrication and validation

In the following section, the validation process of the gripper components based on the data collected from bibliography and experiments is described. Testing was performed using a Zwick 10 kN ProLine equipped with dedicated FFF designed tools. A preliminary study on how the specific process setup affects the mechanical behaviour of the components was performed to choose the materials and building parameters [160,161].

Using an FFF Prusa MK2S five specimens for each test were built according to ISO 527-2:2012. This standard is compatible with AM as indicated in the NIST report [63]. The 1ba geometry was chosen because miniaturization of specimen is relevant to reduce the build time in AM.

The raster orientation ±45° with respect to the prevalent dimension was chosen because this angle configuration is the best to enhance the elastic performance of compliant ABS prototypes. The print was performed with nominal infill 100% and with all the specimens in the same position on the building plate to enhance reproducibility. Minimum layer thickness of 0.1 mm was adopted to have best resolution and minimum surface roughness [162]. Consideration from experimental data comparison, material costs, material processability and data available in literature were made. ABS was chosen for the lower finger and the springs. PLA was chosen for the gripper body and upper finger.

The method by Casavola et al. [77] is suitable for the modelling of the compliant finger. At first it is necessary to measure the elastic modulus in the longitudinal and transverse directions E1 and E2. Five single layer specimens for each configuration were tested according to the ISO 527-2:2012 geometry but with 0.15 mm thickness and raster orientations 0°, 90°, and 45° (Figure 53).

Design for additive manufacturing - Case of study
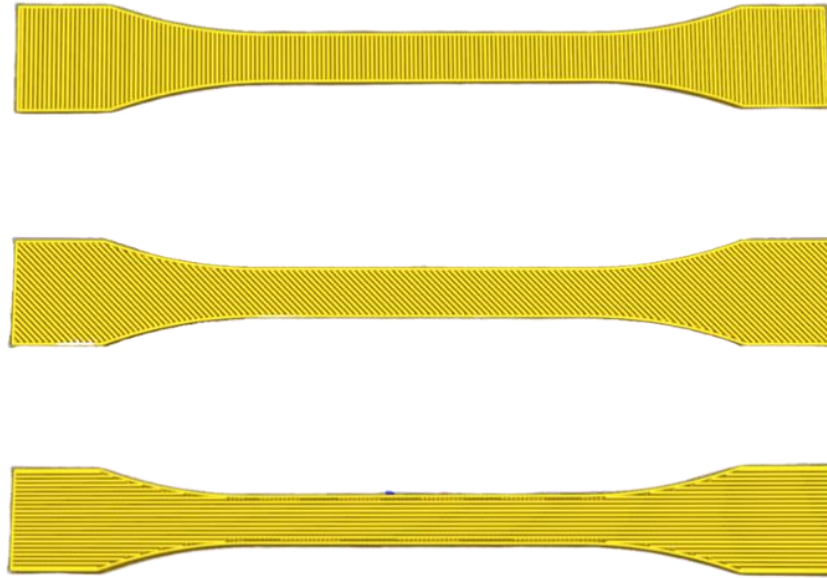
Figure 53: Single lamina dogbone characterization for three different orientations (0°,45°,90°) according to [163].

The ABS specimens were processed using the parameters reported in Table 6

Table 6: Building parameters.

Parameter	Value
Layer height, mm	0.15
Wall line count	2
Infill density, %	100
Infill pattern	Line
Infill overlap percentage, %	15
Printing temperature, °C	255
Build plate temperature, °C	100
Print speed, mm/s	30
Enable print cooling	No

The mechanical properties of the single layer specimens at different raster angle are reported in Table 7.

Table 7: Results of dogbone single layer tensile characterization.

		Tensile Modulus E, MPa	Yield Strength σ_y, MPa	Yield strain ε_y, %
ABS 0°	Average value	2250	31	1.4
	Standard deviation	448	2.06	0.18
ABS 45°	Average value	1930	28.6	1.6
	Standard deviation	196	1.18	0.12
ABS 90°	Average value	1970	23.4	1.6
	Standard deviation	56.0	3.24	0.25

Assuming as Poisson's modulus for ABS the values of v12 = 0.344 measured by Casavola et al. [77], the values of v21 = E22 / E11 = 0.301 were computed.

(Equation **1** [164] is used to compute the shear modulus G_{12} (G_{12} = 711.74 MPa).

$$G_{12} = \frac{1}{\frac{4}{E45} - \frac{1}{E11} - \frac{1}{E22} + \frac{2v12}{E11}}$$ (Equation 1)

Two FE models were made in Altair Optistruct software using around 13 thousand 3D first order elements. In the first model isotropic materials input were used. In the second data from as laminate characterization (Table 7) were used. The aim was to verify if the component displacements are compatible to service loads and if there were significant differences in terms of accuracy with respect to experimental data. The FEM model calibration was done through the analyses of the ISO 527-2 1ba specimen.

For this application 20 N was the maximum load service expected. The load was applied distributed under the sensor location using a linear ramp from unloaded to maximum service load boundary condition. Full DOF constraints were placed on the contact surface between the finger and the gripper main body. The results of the analysis are reported in Figure 54.

Design for additive manufacturing - Case of study

a)	b)
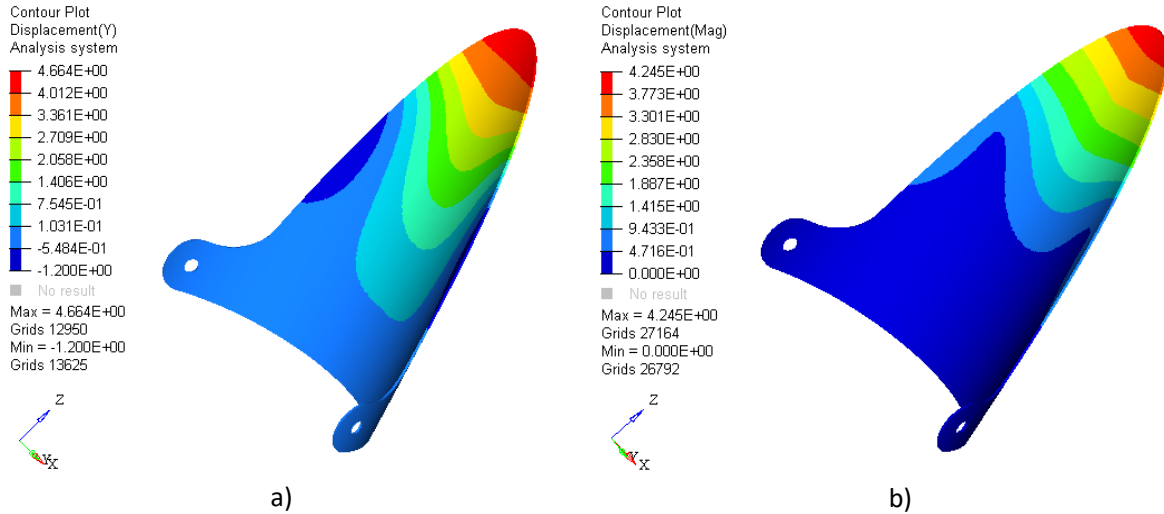
Figure 54: Computed displacements for (a) isotropic material and (b) orthotropic material models.

The average computed displacement in the gripping zone was 3.6 mm. The analysis output confirmed that the displacement caused by the maximum service load comply with the requirements for the gripping function.

The component was built with the same parameter used for the tensile specimens (Table 6). Monotonic loading test in force control was performed: numerical and experimental values are in good agreement (Table 8).

Table 8: Comparison between numerical and experimental values of displacement (mm) for maximum service load.

Computed displacement	Experimental displacement
3.6	3.9

More monotonic loading tests were performed with the sensor assembled on the fingertips. The data from five tests are reported in Figure 55. The sensor had a stiffening effect as the displacement decreased from 3.9 mm to 2.5 mm, therefore the final assembled components have a performance improvement compared to the single part.
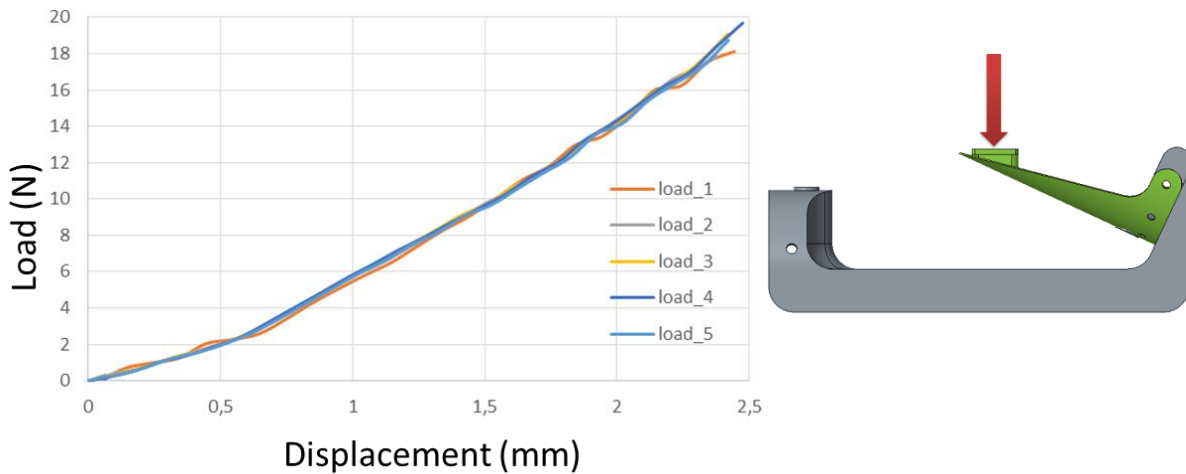
Figure 55: Experimental results from repeated loading.

The fulfilment of collision resulting in immediate displacement of the fingertip at low force was then investigated. Monotonic single and repeated testing were performed on the finger. Tests were performed setting a 10 mm displacement and monitoring the reaction force (Figure 56). Data show a peak of 1.07 N at 7.1 mm of vertical displacement with a stiffness variation at 6 mm correlated to a change in the geometrical configuration. Force values comply with the requirements for the picking function and the collision-proof design.
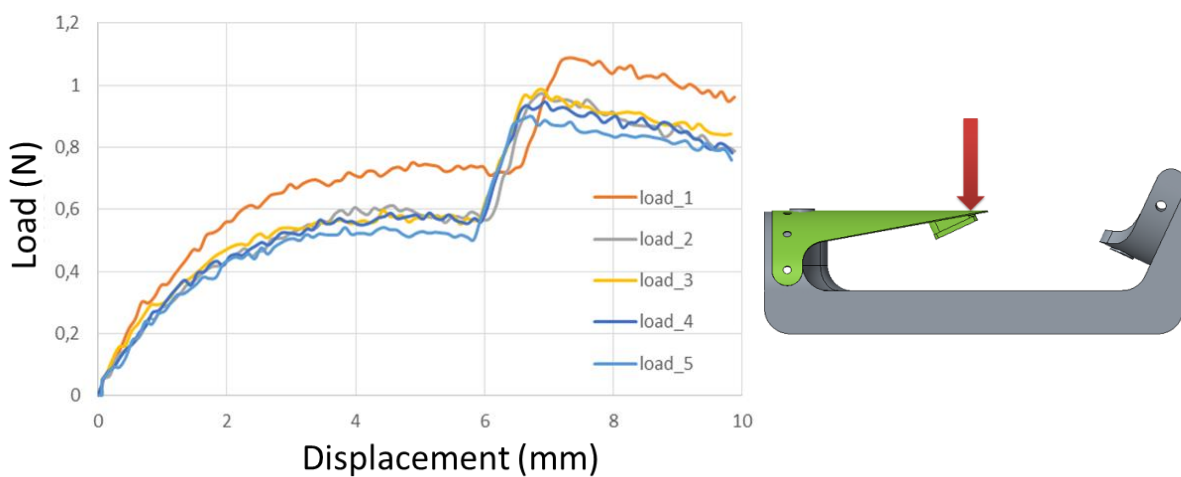
Figure 56: Measured values of reaction force for deflected configuration.

The computed stresses are shown in Figure 57. The value of the first principal stress is 25 MPa. By the experimental characterization of AM processed ABS specimens for R = 0 application [165] the suggested life span of this component can be considered acceptable. It is worth noting that this component can be printed in less than 20 minutes.
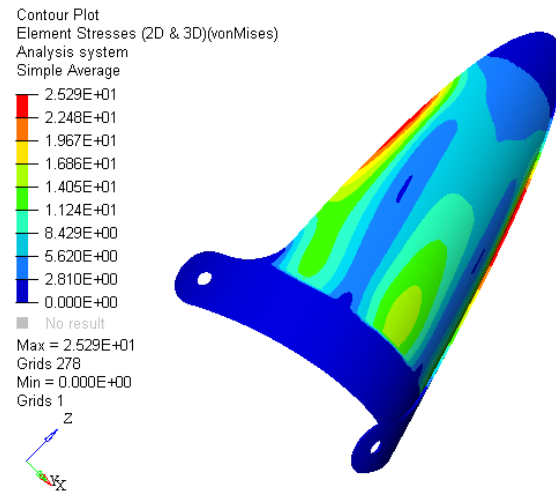
Figure 57: Computed stresses for maximum service load condition.

The springs were built modifying the parameters reported in Table 6 to take advantage of the FFF anisotropy. The infill was set all wall to obtain a deposition parallel to the perimeter. Extra 5% of filament superposition was set to enhance material packing.

Experimental tests were performed to characterize the gripping force developed by the upper finger at the closing and rubbing positions of the springs on the slide. For testing AM with PLA filament was used to recreate the kinematic of the mechanism from the movement of the crosshead as shown in Figure 58.

(a)   (b)

Figure 58: (a) AM setup for spring testing. (b) Slider detail.

Monotonic loading with force control and measured displacement was performed and the stiffness of the spring was then computed. In Figure 59 positive displacement is referred to the rubbing span; negative displacement is referred to the closure span. The values comply with the design requirements.
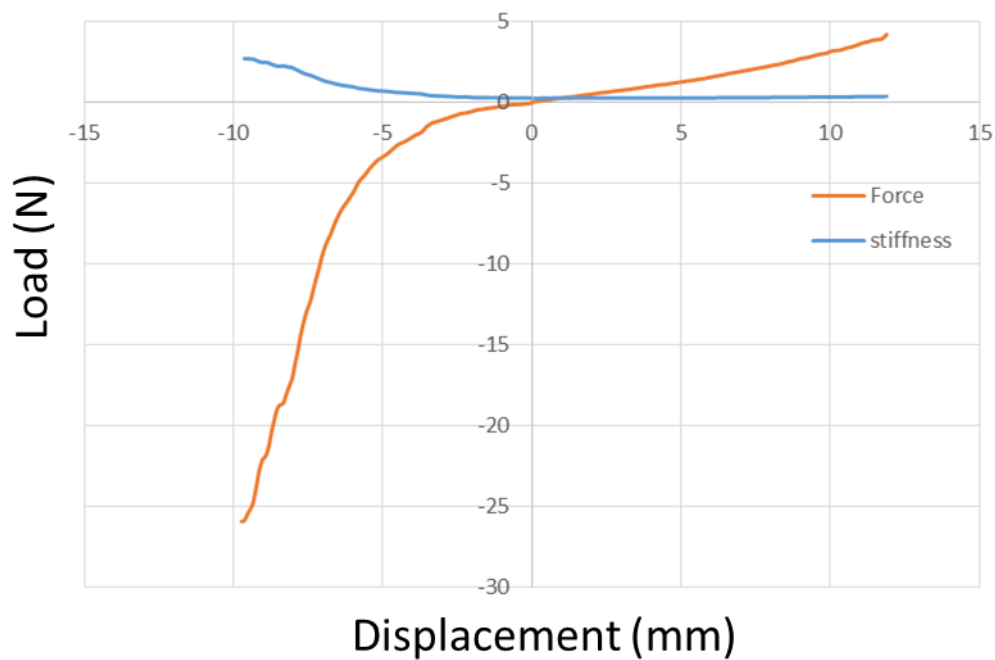
Figure 59: Spring force and stiffness along the trajectory on the slide.

89

FEM analysis was performed using about 3 thousand 2D first order elements materials data in Table 7 (ABS 0°). The boundary conditions for the U-shaped spring were imposed displacements, upward and downward in plane YZ, known from the kinematics.

(a)   (b)
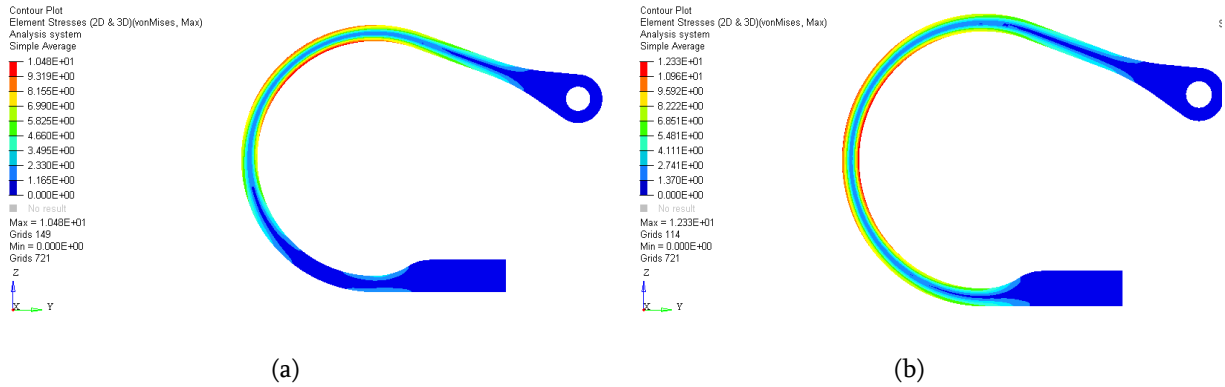
Figure 60: Computed spring von Mises stresses (a) upward displacement (b) downward displacements.

The output is reported in Figure 60 and shows similar values of the stresses in the two configurations, with a peak of 12 MPa for downward displacement and 10 MPa for upward displacement.

A fatigue life prediction based on experimental tests with R = −1 [165] and the first principal stress magnitude of 11 MPa suggests that the life span of this component is more than 10^6 cycles.

90

3.4 Discussion and general remarks

In Chapter 3 a design benchmark of an end effector was performed to produce knowledge on DfAM starting from the data presented in Chapter 1 and Chapter 2. The benchmark focused on a robotic gripping device for non-rigid items manipulation. The output shows a possible optimized design solution based on DfAM. The design of the components has been validated using FEM analysis and mechanical testing. The material data required have been measured from standard and single-layer specimens ad discussed in Chapter 1. Output of the numerical models showed a good matching with the experimental data from monotonic tensile tests performed on specimens and components. Service life prediction based on experimental data was attempted. In the lower finger the computed stresses at maximum service load suggest a limited but acceptable life span for cyclic loadings.

The FFF process is confirmed as a cost-effective option to obtain complex optimized geometries. Most relevant advantages are no tooling delay (time saving) for production and the part count reduction (assembly cost saving). The number of components decreased from more than 40 to 10 and only a single actuator is used, therefore a dramatic miniaturization was possible (Figure 61).
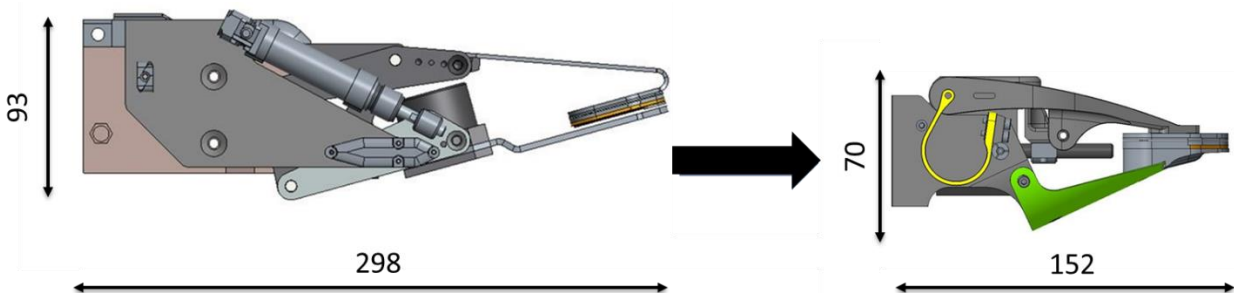
Figure 61: Comparison of the overall dimensions (mm) between original and AM designs.

Moreover, the DfAM gripper can be adapted to different tasks in short amount of time using the advantages of the AM process to change the shape or the length of the fingers. The total build time is 20 hours and the used material is 140 g. The total weight of the FFF gripper is 330 g, a reduction in weight of 85% compared to the original one.

From the work presented in Chapter 3, was possible to identify relevant research topics. One of the relevant topics is that the printing parameters play a critical role on materials properties. Therefore, if carefully calibrated, the printing parameters can be used as design variable to affect the materials and surfaces characteristics. This research topic was investigated in Chapter 4. Another relevant topic is the

Design for additive manufacturing - Case of study

improvement of the adhesive bonding performance; therefore available surface modifications were evaluated in Chapter 5. Finally, innovative joining solutions for AM components, in order to obtain components ready to be assembled, were investigated in Chapter 6.

Chapter 4

Design for Additive Manufacturing applied to

surface modifications for bonded joints

This chapter is based on papers [150,166] and is aimed at exploring the influence of Fused Filament Fabrication printing parameters on the Mode I fracture toughness of polymer bonded joints.

The motivation is that realizing small-size, highly optimized AM parts to be later assembled into larger components or on a main structure can be convenient from the manufacturing standpoint. Adhesive bonding is a suitable joining technology as it avoids distortion and material modification due to heat like welding, or the presence of fasteners.

Since printing parameters can affect surface roughness and wettability (not only adherend strength and stiffness) they can become effective design parameters for bonded joints. Therefore, in this chapter two different materials frequently used in FFF, PLA and ABS, and three different printing parameters, namely extruder temperature, printing speed and layer thickness, were selected in order to evaluate their influence on roughness, wettability and tensile behaviour of the adherends.

A full-factorial Design of Experiment (DoE) was chosen for the study of roughness and wettability that requires a limited specimens manufacturing and measurement time, while a Taguchi L9 orthogonal array was selected for the tensile tests, in order to save manufacturing and testing time. The significance and the mutual interactions of printing parameters were identified by ANOVA.

Combinations yielding maximum and minimum values of the output, respectively, were used to produce adherends for Double Cantilever Beam (DCB) joints and evaluate the effect on Mode I fracture toughness, demonstrating that process parameters do have an effect on fracture toughness and that an optimum value can be found by simply operating on the FFF printer setup

Design for Additive Manufacturing applied to surface modifications for bonded joints

4.1 Background and motivations

From the analysis of the results of previous chapters was pointed out that one of the next challenges of DfAM is the definitions of the methods to assemble the AM components together or on a main structure [107]. One of the first investigations on selecting suitable techniques for joining AM components was carried out by Espalin et al. [114], in which methods were sorted in order of effectiveness with respect to the strength of the joint: hot air welding, ultrasonic spot welding, solvent and adhesive bonding. Adhesive and solvent bonding methods were therefore suggested when one values aesthetic results and is not concerned with mechanical property performance. However, adhesive bonding can be performed without heating, that was proven to have a detrimental effect on the dimensional accuracy of the AM components [167] especially if materials to be joined shows different coefficients of thermal expansion.

Taking advantage of adhesive bonding, heterogeneous materials joints can be performed, Kariz has studied the influence of 3D-printing parameters on the bond shear strength of 3D-printed ABS bonded to beech wood [28]. After the first work by Arenas et al. [115] in which a method was proposed to select structural adhesives for AM, several works focused on coupling the tailoring enabled by AM to the knowledge of adhesion and failure mechanisms [119] in order to lower peel and shear stress concentrations that develops at the ends of bonded joints, hence to obtain overall joint performance improvements. Examples are FGM adherends obtained in [44] using MMAM, cavities through the thickness of the adherend structures that cause crack trapping [35] or LDM to obtain stepwise adhesive stiffness changes [33]. However, even if improvements in joint strength can be achieved by tailoring methods, most of failures were adhesive, except for epoxy resins that have good compatibility with most of AM materials [21], pointing out that further improvements could be achieved till reaching cohesive or adherend failures.

As remarked by Packham [51] surface physics and morphology plays a key role in the adhesion mechanisms, however only few works are available on surface modifications for AM. In Chapter 2 was presented that Bürenhaus et al [23], Li et al. [25], Fieger et al [38], Leicht et al [37], investigated overlap surface modifications using industrial methods as mechanical abrasion, chemical etching, flame impingement, corona treatment and Atmospheric Pressure Plasma (APP). Even if industrial modifications, and in particular APP, led to adhesion improvements, specific equipment and post-processing are required, thus alternative approaches to embed surface modifications in AM processes were investigated. These approaches do not require any specific equipment and are based on the observations that printing setups, as parts placement in the build volume and material deposition patterns, and printing parameters,

95

as layer height, infill, nozzle temperature and speed, affect material physics, i.e. crystallinity [71], and properties, i.e. Young's modulus [168] and surface roughness [169].

As pointed out in the NIST report by Forster [63], at time of writing current standard are not applicable for AM adherends and dedicated modifications are required. Most of the works in literature adopt SLJs, but several different geometries have been proposed to investigate additively manufactured joints as summarized in Chapter 1. Regarding joint characterization, one of the most relevant test methods is DCB as it provides data for mode I loading, which is known to be critical for the strength of adhesive bonding. First explorative works were carried out by Morano et al. [34,35], Alfano et al. [36], Garcia-Guzman et al. [30]; however, those papers focused on a specific geometrical tailoring across adherend thickness rather than studying if and how AM process parameters could influence the fracture toughness of the joint.

The work presented in Chapter 4 is aimed therefore at exploring in detail the influence of the adherend surface and mechanical properties obtained by varying the FFF printing parameters on the Mode I fracture toughness of bonded joints. Two different materials frequently used with FFF, PLA and ABS [112], and three different printing parameters, namely extruder temperature, printing speed and layer thickness, each at three levels, were selected in order to evaluate their influence on roughness, wettability and mechanical properties of the adherends. This configuration (3 factors, 3 levels) entails 27 possible combinations for each considered material. Parameters values were combined using a statistical approach and their importance and mutual interactions were identified by analysis of variance (ANOVA) [170]. Combinations yielding maximum and minimum values of the output, respectively, were used to produce adherends for DCB joints to assess the effect of the corresponding surface morphologies on Mode-I fracture toughness.

4.2 DfAM for process embedded surface modification: a study on additive manufacturing build parameters as bonded joint design factors

Adhesion mechanisms are based on mechanical interlocking and on the ability of the adhesives to be in contact and interact with the adherends, i.e. wettability and diffusion. In this sense, layer height is a relevant printing parameter as it modifies the surface roughness and affects adhesion trough mechanical interlocking mechanism. Wettability is affected not only by roughness [171] but also by the physics of the surface, i.e. polarity and crystallinity, therefore extruder temperature and deposition speed are relevant parameters for adhesion, too, since they do not only affects the surface morphology but also its physics though the thermal cycle experienced by the polymeric material [71,172,173]. These printing parameters (extruder temperature, deposition speed and layer height) affect also other mechanical properties and build time. Moreover, interaction exists between parameters, making crucial to evaluate the process parameters-surface properties relationship in order to obtain the desired bonded joint performance improvement.

Specimens were manufactured using an FFF Delta Wasp 4070 3D printer (WASP, Massa Lombarda, Italy), with PLA from BQ (BQ, Madrid, Spain) and ABS from Sienoc (Taiwan, China). The same flatwise (Figure 39) placement at build plate centre, where temperature is monitored by a thermocouple, was adopted. Preliminary specimens were manufactured in order to validate qualitatively this build approach, as these two polymers have different physical properties. The effects of the three design parameters, namely deposition speed (V), extruder temperature (T) and layer height (H), were investigated on three levels, minimum, medium and maximum of the operating ranges (Table 9) indicated by the material suppliers.

Table 9: Printing parameters for PLA and ABS, their levels and coding: note the only values changing between the two materials are printing temperatures.

Deposition speed, V (mm/s)	Layer height, H (mm)	PLA Extruder temp., T (°C)	ABS Extruder temp., T (°C)	Taguchi L9 OA DoE coding
30	0.1	200	230	1
75	0.2	215	240	2
120	0.3	230	250	3

Design for Additive Manufacturing applied to surface modifications for bonded joints

In order to determine how the factors (extruder temperature, deposition speed and layer height) affect the response variables (the mechanical and surface properties), DoE systematic approach to process optimization [170,174] has been used. To study the effect of the print parameters on tensile behaviour of the adherends, a Taguchi L9 Orthogonal Array (OA) [175] was selected instead of a full-factorial one in order to reduce the number of specimens to be manufactured, while at the same time the orthogonality of the design allows to apply consistently ANOVA to estimate the effects of each factor and identify its interactions [176]. Printing parameters V, T, H are respectively assigned as first, second and third factor of the OA. Since the FFF manufactured PLA and ABS behave almost linearly up to failure, only the ultimate strength has been chosen to represent the tensile behaviour for the sake of simplicity. In order to have sufficient degrees of freedom (the minimum number of independent experiments to be conducted: one for the mean value and two for each of the remaining factors), the Taguchi L9 OA is filled in with the nine experiment configurations reported in Table 10. Three test repetitions for each configuration have been performed.

Table 10 Coded Taguchi L_9 Orthogonal Array for the characterization of the tensile behaviour of the adherends.

Trial number	Deposition speed, V (mm/s)	Extruder temp., T (°C)	Layer height, H (mm)
L_{9_C1}	1	1	1
L_{9_C2}	1	2	2
L_{9_C3}	1	3	3
L_{9_C4}	2	1	2
L_{9_C5}	2	2	3
L_{9_C6}	2	3	1
L_{9_C7}	3	1	3
L_{9_C8}	3	2	1
L_{9_C9}	3	3	2

Since, differently from tensile tests, the specimens to investigate surface morphology and wettability required a short manufacturing time, a full-factorial design was used in this case to investigate changes in morphology and wettability. Print placement on the build plate, infill and raster orientation are kept constant between different designs.

4.2.1 Experimental characterization of the effect of the build parameters on the adherends

Tensile strength has been evaluated using MaCh3D miniaturized testing machine (MaCh3D srl, Parma, Italy) equipped with a 5 kN load cell. Three repetitions for each L9 OA have been performed, both for PLA and ABS, using MaCh3D proprietary tensile test specimen (Figure 62).

Width, W (mm)	Reduced sect. , L_c (mm)	Shoulder radius, R (mm)
13	57	52
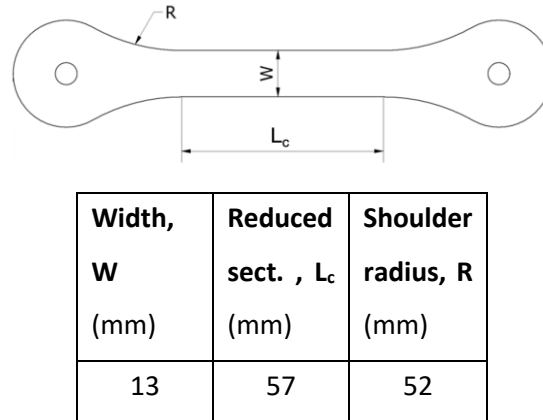
Figure 62:. MaCh3D proprietary tensile test specimen.

Tests were carried out at a constant crosshead speed of 5 mm/min, according to ASTM D638 and a MTS 632 31F-24 extensometer (MTS Systems Corporation, Eden Prairie, USA) was used to measure gauge elongation. Specimens were produced with a 100% infill and a ±45° raster orientation with respect to specimen length direction. The ±45° raster has been adopted for the AM items in this study, since it makes an even surface pattern and it is the standard raster angle assigned by Ultimaker CURA 4.6.1 AM software to the infill of components. Average tensile curves and related scatter bands are reported in Figure 63 (a) for PLA and (b) for ABS, respectively. The legend in Figure 63 reports both the Taguchi L9 OA trial number (Table 10) and, for the sake of reading-ness, the corresponding printer setup as V (mm/min)-T (°C)-H (mm).
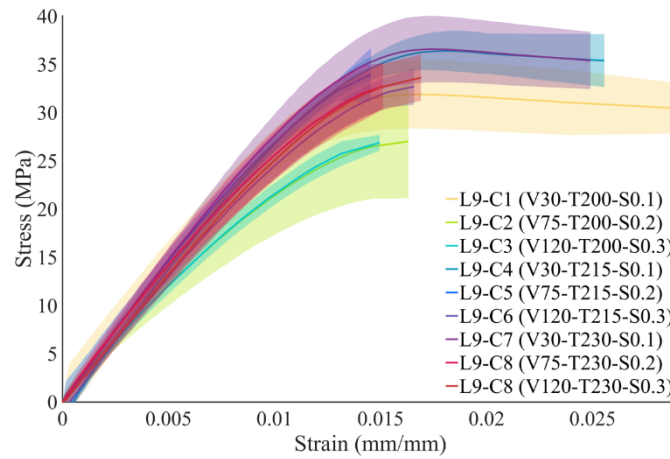
(a)
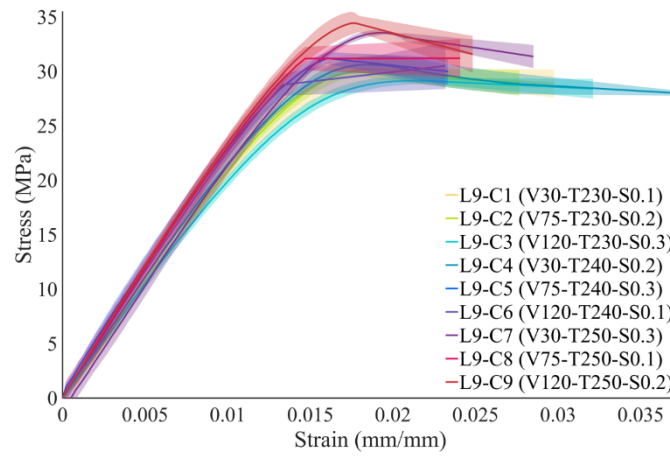
(b)

Figure 63: Averaged strain-stress curves together with data dispersion band, for PLA (a) and ABS (b).

Average ultimate tensile strengths (R_m) with error bars representing one standard deviation more or less than the average, are reported in Figure 64 for the different setups chosen according to the Taguchi L9 OA method.
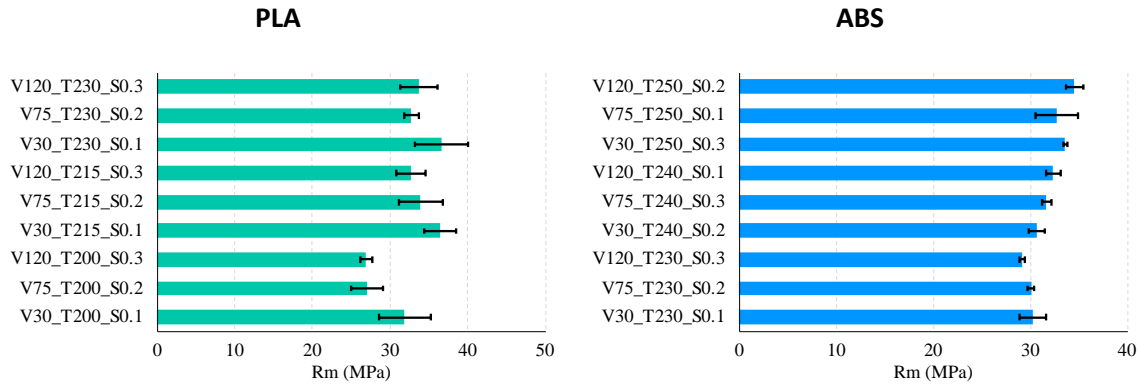
Figure 64: Average ultimate tensile strength (R_m) with error bars representing +/- one standard deviation for the various Taguchi L_9 OA trials.

Regarding R_m, the best mechanical performances are obtained with high extruder temperature for both materials. PLA presents a gradual increase in strength by decreasing layer thickness as well as deposition speed, whilst ABS presents the best performances with high speed and layer thickness, indicating that, in this case, a higher printing temperature seems to be more influential than other parameters. It is confirmed that parameters investigated have a relevant effect on the mechanical properties, maximum variations of Rm are 35% and 19% respectively for PLA and ABS. Similar variations are measured also for Young's modulus average value reported in Figure 65.
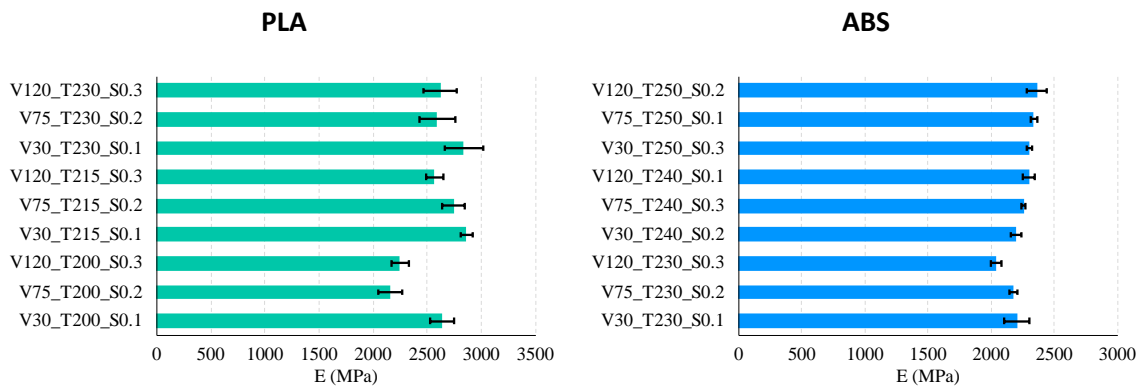
Figure 65: Average Young's modulus (E) with error bars representing +/- one standard deviation for the various Taguchi L_9 OA trials.

Hexahedral tiles of 15×15×1.2 mm^3 size was manufactured for each of the 27 full-factorial set-ups. This small and shallow specimen has been adopted in order to save build time, since surface properties and morphology are evaluated only on the last deposited layer and on a 3x3 mm^2 area.

Changes in morphology of the surface to be bonded are quantified using 2D surface roughness parameter *Sa*, measured according to ISO 25178-2:2012 with a CCI 3D optical profilometer (Taylor Hobson, Leicester, UK). *Sa* is the absolute value of peaks and valleys height, z, integrated along the surface coordinates x and y and averaged over the surface sampling area A (Equation 2).

$$S_a = \frac{1}{A} \iint_A |z(x,y)| \, dxdy$$
(Equation 2)

The surface is analysed at three different locations on surfaces of 3×3 mm^2 each. *Sa* measurement for each printing setup are reported in Table 11. The configuration "PLA_V120_T200_H0.2" since the measurement was not possible at several points within the sampling area A, as the profile of the valleys was too sharp to be correctly detected by the optical profilometer.

Table 11: Surface roughness values.

PLA

Deposition speed, V (mm/s)	Extruder temp., T (°C)	Layer Height, H (mm)	Surface rough., Sa (µm)
30	200	0.1	**7.97**
		0.2	**9.80**
		0.3	**10.87**
	215	0.1	**7.30**
		0.2	**9.79**
		0.3	**11.06**
	230	0.1	**9.20**
		0.2	**8.16**
		0.3	**11.46**
75	200	0.1	**9.25**
		0.2	**11.17**
		0.3	**11.26**
	215	0.1	**10.61**
		0.2	**8.84**
		0.3	**13.34**
	230	0.1	**11.02**
		0.2	**16.17**
		0.3	**18.68**
120	200	0.1	**23.64**
		0.2	-
		0.3	**15.04**
	215	0.1	**12.64**
		0.2	**15.88**
		0.3	**13.68**
	230	0.1	**12.54**
		0.2	**10.86**
		0.3	**14.24**

ABS

Deposition speed, V (mm/s)	Extruder temp., T (°C)	Layer Height, H (mm)	Surface rough., Sa (µm)
30	230	0.1	**15.35**
		0.2	**12.28**
		0.3	**13.56**
	240	0.1	**17.58**
		0.2	**13.68**
		0.3	**12.87**
	250	0.1	**13.78**
		0.2	**9.53**
		0.3	**19.24**
75	230	0.1	**12.48**
		0.2	**11.81**
		0.3	**14.90**
	240	0.1	**17.13**
		0.2	**11.59**
		0.3	**10.16**
	250	0.1	**11.38**
		0.2	**10.42**
		0.3	**14.81**
120	230	0.1	**13.98**
		0.2	**10.60**
		0.3	**13.52**
	240	0.1	**12.56**
		0.2	**10.88**
		0.3	**15.76**
	250	0.1	**12.07**
		0.2	**11.96**
		0.3	**11.09**

Design for Additive Manufacturing applied to surface modifications for bonded joints

An example of PLA morphology variation due to a change in the printing parameters is shown in Figure 66.
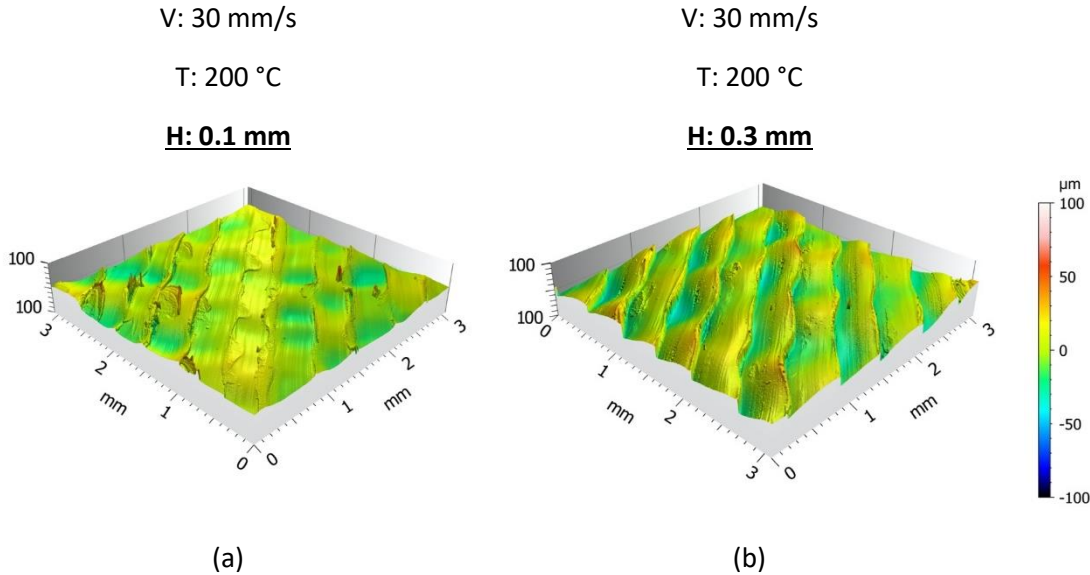
Figure 66: Comparison between 0.1 mm layer height (a) and 0.3 mm (b) maintaining all other parameters unchanged, in the case of PLA.

Wettability analysis was performed on the same tile specimens used for morphology characterization, by the means of sessile drop test with deionised water. The effect of surface texture direction due to the process was taken in account performing multiple measurements according to the methods proposed in [171] for the experimental investigation of the wettability of rough engineering surfaces. First, the surfaces of the specimens were cleaned using a degreasing solvent (Loctite 7063, Henkel, Milan). Then static contact angle (Θ) measurements were performed at room temperature depositing 2 µl calibrated water drops and taking snapshot after 10 s with a custom-made set-up based on a Dino-lite microscope (AnMo Electronics Corporation, Hsinchu 300, Taiwan) in a direction orthogonal to the surface raster angle. The static contact angle was evaluated from the tangent curve to the drop profile in the contact point between sessile drop and substrate surface. Measurements were repeated 3 times on each tile at 3 different locations. Results are reported in Table 12.

Table 12: Static contact angle (Ө) measurements in the direction orthogonal to the surface raster angle

PLA   **ABS**

Deposition speed, V (mm/s)	Extruder temp., T (°C)	Layer Height, H (mm)	Contact angle., Ө (deg)	Deposition speed, V (mm/s)	Extruder temp., T (°C)	Layer Height, H (mm)	Contact angle., Ө (deg)
30	200	0.1	61	30	230	0.1	64.00
		0.2	66			0.2	63.00
		0.3	77			0.3	81
	215	0.1	83		240	0.1	82
		0.2	76			0.2	81
		0.3	73			0.3	77
	230	0.1	68		250	0.1	89
		0.2	75			0.2	60
		0.3	78			0.3	83
75	200	0.1	77	75	230	0.1	80
		0.2	72			0.2	72
		0.3	60			0.3	73
	215	0.1	78		240	0.1	76
		0.2	65			0.2	80
		0.3	78			0.3	80
	230	0.1	75		250	0.1	81
		0.2	64			0.2	80
		0.3	66			0.3	85
120	200	0.1	66	120	230	0.1	83
		0.2	54			0.2	71
		0.3	55			0.3	71
	215	0.1	62		240	0.1	66
		0.2	75			0.2	83
		0.3	71			0.3	80
	230	0.1	65		250	0.1	69
		0.2	67			0.2	83
		0.3	73			0.3	70

In general, the measured values of static contact angle for the various setups were slightly different, but comparable, with the values of static contact angle already published for the investigated materials. Contact angles values maximum variations are 35% for PLA and 39% for ABS. It should be noticed that wettability is a complex phenomenon affected by different phenomena to be taken in account, as roughness that can change wetting regime and surface free energy [171]. As this chapter is focused on assessing feasibility of using printing parameters to affect bonded joints performance, static contact angle of demineralized water droplets can be used as a qualitative indicator of the sum of these effects. However, after performing more dedicated characterization for a specific material processed with a specific 3D printer, it can be possible to maximize wettability changes, it will be used in the next chapter to choose the printing parameters.

ANOVA was performed [170] on the data sets from tensile and surface characterizations to identify the main and the interactions effects of printing parameters on tensile strength, roughness and wettability using the procedure validated and presented in [150]. In particular, using the F-ratio test was possible to determine whether factors or interactions were relevant on each variation of the monitored output. If F is higher than a critical value given by the degrees of freedom of the experiment, then the factor or interaction affects the monitored output, otherwise the variation of the monitored output is due to noise. In defining optimised printing parameters for R_m, S_a and Θ, if one of the factor was marked as non-significant, its value was selected as the one minimizing the build time.

As far as tensile strength (R_m) is concerned, the value at different parameter levels is given in Figure 67 for PLA and in Figure 68 for ABS.
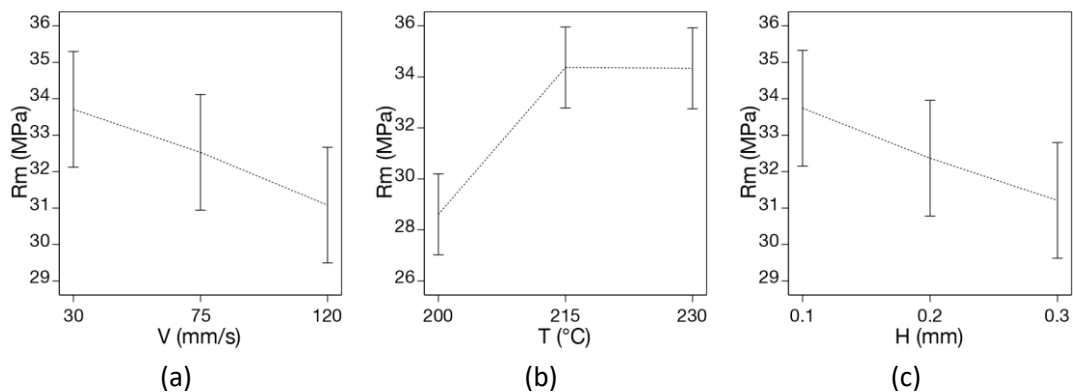
Figure 67: Main effects for mechanical strength of PLA: Deposition speed (a), Temperature (b), Layer height (c).
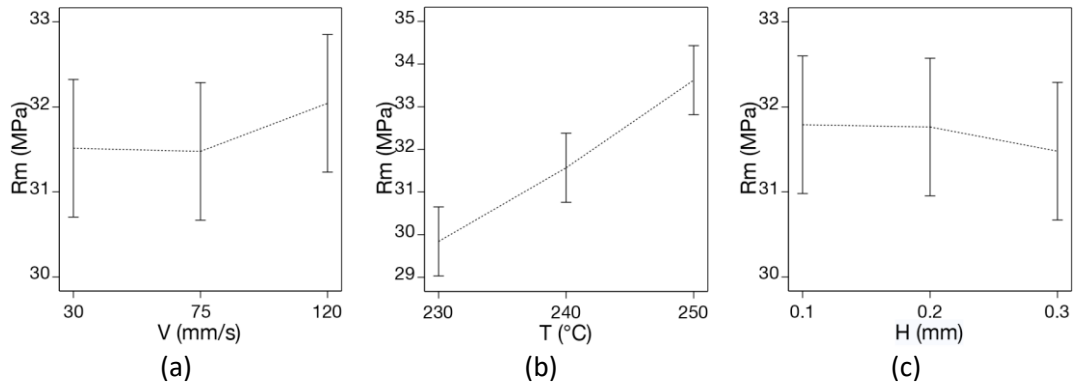
Figure 68: Main effects for mechanical strength of ABS: Deposition speed (a), Temperature (b), Layer height (c).

The F-test identifies for both materials the extruder temperature as the main effect influencing tensile strength (Table 13). The Lack-of-Fit F-value of 1.80 (ABS) and 1.93 (PLA) implies that Lack-of-Fit is not significant relative to the pure error, since there is only a 19.33% (ABS) and 17.33% (PLA) chance that a Lack-of-Fit F-value this large could occur due to noise.

Table 13: ANOVA results for tensile strength (R_m).

PLA

Source	F-value	p-value	Significance
Model	4.13	**0.0074**	**significant**
T	9.5	**0.0013**	**significant**
V	1.5	0.2482	
H	1.39	0.2732	
Residuals			
Lack-of-Fit	1.8	0.1933	**not significant**

ABS

Source	F-value	p-value	Significance
Model	4.11	**0.0075**	**significant**
T	11.9	**0.0004**	**significant**
V	0.3327	0.7209	
H	0.0988	0.9064	
Residuals			
Lack-of-Fit	1.93	0.1733	**not significant**

Regarding surface roughness in the case of PLA, from one of the most influential effects is deposition speed, having a p-value of 0.0024 (Table 14), as well as the interaction between deposition speed and extruder temperature. Interaction graph for deposition speed and temperature is reported in Figure 69.

107

Table 14: ANOVA results for surface roughness in the case of PLA adherends.

Source	F-value	p-value	Significance
Model	3.66	**0.0118**	significant
V	9.29	**0.0024**	
T	0.5633	0.5809	
H	1.07	0.3681	
VxT	3.52	**0.0322**	
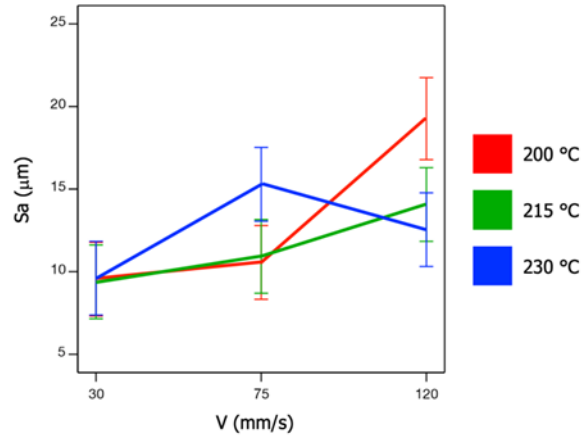
Figure 69: Interaction effect between deposition speed and extruder temperature in determining surface roughness for PLA.

In the case of ABS, the main contribution to surface roughness is determined by layer height, as indicated in Table 15. The model appears to be not significant due to a probability (p-value) higher than 0.05 that F is due to noise. However, looking at the p-values of the single parameters, the origin of such potential noise is related mainly to the extruder temperature, T. A different temperature range and/or a more careful control maybe needed in this case to evaluate if T is effectively influencing the ABS surface roughness. It is worth to remark that, when restricted to V and H only, the model becomes significant.

Table 15: ANOVA results for surface roughness in the case of ABS adherends.

Source	F-value	p-value	Significance
Model	2.22	0.084	not significant
V	1.73	0.2024	
T	0.3925	0.6805	
H	4.53	**0.0239**	

In all cases, a strong interaction exists between all the parameters for both materials. As it can be noticed from Table 16 and Table 17 analysis, temperature and layer height are the most significant factors.

Table 16: ANOVA results for static contact angle Ө for PLA.

Source	F-value	p-value	Significance
Model	5	**< 0.0001**	significant
V	1.16	0.3208	
T	12.73	**< 0.0001**	
H	12.43	**< 0.0001**	
VxT	0.8679	0.4895	
VxH	3.99	**0.0067**	
TxH	2.26	0.0754	
VxTxH	6.11	**< 0.0001**	

Table 17: ANOVA results for static contact angle Ө for ABS.

Source	F-value	p-value	Significance
Model	6.33	**< 0.0001**	significant
V	2.35	0.1055	
T	8.18	**0.0008**	
H	4.01	**0.0241**	
VxT	4.72	**0.0025**	
VxH	8.56	**< 0.0001**	
TxH	3.42	**0.0149**	
VxTxH	8.58	**< 0.0001**	

4.2.2 Validation of using the build parameters as bonded joint design factors

In this sub-section the results presented in Chapter 2 and in the previous sub-section are processed to define the printing setups that maximize or minimize the adherend properties relevant for adhesive bonding applications, that is Rm, Sa, Ө. The setups are shown in Table 18 and Table 19, for PLA and ABS respectively. Experimental validation was carried out using AM dedicated DCB configurations.

A custom DCB specimen geometry has been developed following DfAM approach [109]. The joint geometry is shown in Figure 70. One of the main constraints was to print adherends with faces to be bonded parallel to the building plane in order to have morphological surface characteristics as close as possible to that analysed during surface characterization. This required the use of support material, removed afterwards, in order to obtain the cylindrical loading hole. Adherends have been printed in pairs,

one pair at a time in order to minimize variations due to the different position on the printing table [177,178].

h	B	L	a_0	t
(mm)	(mm)	(mm)	(mm)	(mm)
10.0	20.0	140.0	30.0	0.3
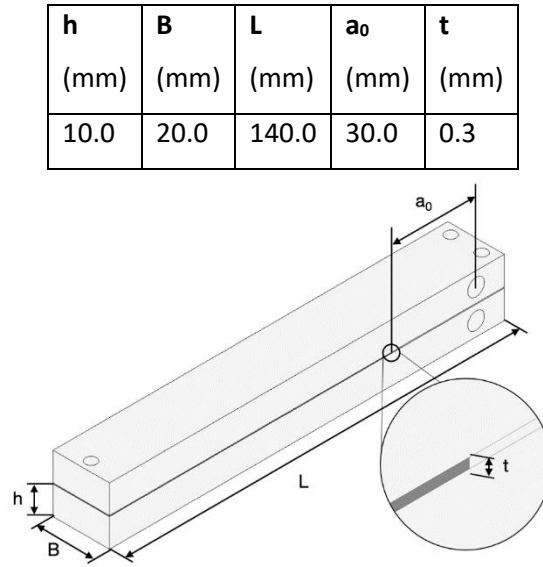
Figure 70: Overall joint geometry.

Figure 71 shows the printing preview of the top view cross section as generated from Ultimaker CURA 4.6.1 software, detailing different structures. In particular, it is possible to see the support structure (light blue) inside the loading hole and the infill reticular structure. Infill shape and percentage influence joint fracture toughness as emerges from the work of Morano et al. [34,36]. Since the present study of fracture toughness is comparative, possible differences are eliminated by maintaining the same infill strategy for all specimens.
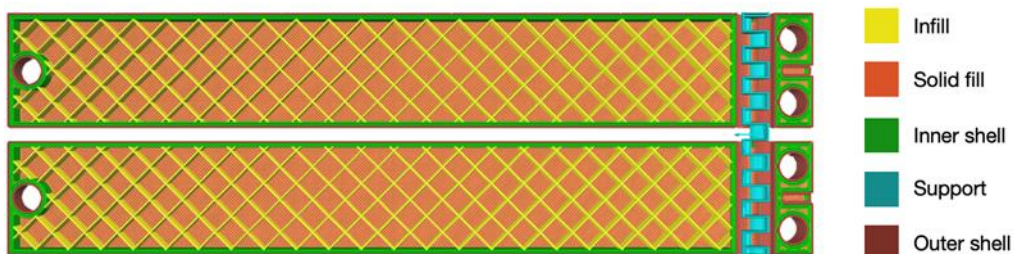
Figure 71: DCB adherends internal structure as previewed from CURA 4.6.1 software.

110

Printing parameters are those reported in Table 18 and Table 19 for PLA and ABS, respectively, resulting in 4 and 6 different parameters combinations for PLA and ABS. To facilitate the interpretation of results, a code is provided for each print setup.

Table 18: Printing parameters for PLA adherends.

Parameter	Roughness		Wettability		T. Ultimate Strength	
	MAX	MIN	MAX	MIN	MAX	MIN
Configuration name	*PLA_01*	*PLA_02*	*PLA_02*	*PLA_03*	*PLA_04*	*PLA_03*
Deposition speed, V (mm/s)	120	30	30	120	30	120
Extruder temp., T (°C)	200	215	215	200	230	200
Layer height, H (mm)	0.1	0.1	0.1	0.3	0.1	0.3

Table 19: Printing parameters for ABS adherends.

| Parameter	Roughness		Wettability		T. Ultimate Strength	
	MAX	MIN	MAX	MIN	MAX	MIN
Configuration name	*ABS_01*	*ABS_02*	*ABS_03*	*ABS_04*	*ABS_05*	*ABS_06*
Deposition speed, V (mm/s)	30	30	75	30	120	75
Extruder temp., T (°C)	250	250	250	230	250	230
Layer height, H (mm)	0.3	0.2	0.3	0.1	0.1	0.3

Concerning the adhesive, Teroson PU 9225, a polyurethane based two-components adhesive supplied by Henkel that cures at room temperature, was chosen according to the results obtained by Arenas [115]. Bulk tensile properties were characterized by testing ASTM D638 Type IV specimen obtained by pouring adhesive into a Polytetrafluoroethylene (PTFE) mould; results are reported in Table 20.

Table 20: Teroson PU9225 Mechanical properties.

Young's Modulus, E_A (MPa)	Poisson's Ratio, v_A	Ultimate Strength, Rm_A (MPa)
576.9	0.33	13.3

Surfaces were cleaned with Loctite 7063 cleaning agent after verifying that the treatment did not affect surface morphology. No mechanical or chemical surface treatment was done in order to preserve the as-built surface texture, with the intention to evaluate if the as-built roughness and texture could compensate by mechanical interlocking the limited adhesion of PLA and ABS, testified by the high surface contact angles. This choice goes into the direction of exploring and exploiting the potential of AM to manufacture ready-to-go components. A polyester sheet was placed on one side of the specimens to create an initial 30 mm long crack (a_0). The adhesive was applied and a layer thickness of 0.3 mm was ensured by placing calibrated metal foils between adherends. The substrates were bonded together by tightening bolts placed in holes at the adherends ends. Joints were cured at room temperature for at least one day before testing. Three repetitions for each combination are performed. A fixture has been developed to allow MaCh3D to perform DCB testing.

For a correct setting and analysis of Mode I DCB fracture test, it is necessary to know how the adherends deform under load. For isotropic materials, the substrate behaviour can be described with a good approximation by the Young's modulus E but this does not apply to anisotropic materials such the ones produced through FFF [112,179] where out-of-plane elastic modulus and shear modulus play a relevant role in determining material compliance. Flexural and shear moduli were therefore extracted by three-points bending tests done at different span distances. A three-points bending (3PB) test equipment has been designed to be compliant to ASTM D790 and ASTM D7264, respectively, Figure 72. The test was done for all the setups listed in Table 18 and Table 19.
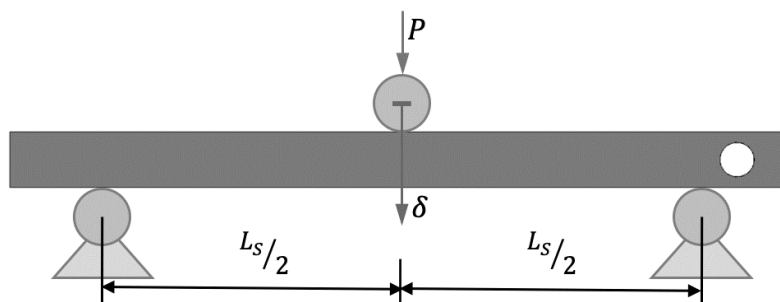

Figure 72: 3PB Test scheme.

The load point displacement, δ, is recorded together with the applied load P. In evaluating specimen compliance, a correction to account for equipment stiffness has been considered.

The 3PB specimen compliance, C_{3PB}, (Equation 3):

$$C_{3PB} = \frac{\delta}{P} = \frac{\left(L_s/2\right)^3}{6E_f I} + 0.6\frac{L_s/2}{GBh}$$

(Equation 3)

where E_f and G are the flexural modulus and the shear modulus, respectively, L_s is the span length, B and h are width and height of the adherends. Performing tests at different L_s, allows to evaluate E_f and G by best fitting (Equation 3) with the least squares method, since shear and bending contribution to deformation varies. In particular, four different span lengths from 40 to 100 mm in steps of 20 mm were considered. Tests were performed under displacement control in the elastic regime, where the crosshead speed was being increased for increasing support span in order to keep the same deformation rate. The compliance was evaluated by performing a linear regression on the displacement-load data for each of the tested configurations at every considered span length. For each configuration, two repetitions were performed, and the average compliance was considered.

The identified moduli are reported in Table 21 for the two materials and the FFF setups listed in Table 18 and Table 19. It is worth to underline that, differently from bulky polymeric components obtained with traditional manufacturing techniques, the shear modulus is more than one order of magnitude lower than the flexural, making the contribution of shear to the bending stiffness non-negligible even for slender structures.

Table 21: Values of E_f and G for the two materials and FFF setups listed in Table 18 and Table 19.

Specimen	E_f (MPa)	G (MPa)	Optimized bonding parameter
PLA_01	1608	65	Max. Roughness
PLA_02	1622	181	Min. Roughness, Max. Wettability
PLA_03	1697	114	Min. Wettability, Min. Tensile Strength
PLA_04	1911	80	Max. Tensile Strength
ABS_01	1167	90	Max. Roughness
ABS_02	1493	56	Min. Roughness
ABS_03	1288	65	Max. Wettability
ABS_04	1404	66	Min. Wettability
ABS_05	1495	53	Max. Tensile Strength
ABS_06	1367	51	Min. Tensile Strength

The testing of a DCB with a relatively soft layer in between the two cantilevers, impose to consider root rotation at the crack tip, stress concentration effects, and the presence of a non-negligible fracture

process zone (FPZ) ahead of the crack tip [180], but it requires also that the deformation of the adhesive layer is accounted for in the evaluation of strain energy release rate. Therefore, the method reported in the work of de Moura [181,182], based on the definition of an equivalent crack length, a_e, evaluated directly from specimen compliance C, that accounts also for the presence of a at the crack tip. The compliance C is expressed as:

$$C = \frac{8a_e^3}{E_f Bh^3} + \frac{12a_e}{5GBh}$$
(Equation 4)

and can be rewritten in polynomial form:

$$\alpha a_e^3 + \beta a_e + \gamma = 0$$
(Equation 5)

where the coefficients α, β and γ are, respectively:

$$\alpha = \frac{8}{E_f Bh^3} \qquad\qquad \beta = \frac{12}{5GBh} \qquad\qquad \gamma = -C$$
(Equation 6)

By solving (Equation 5) and considering only the real solutions, a_e takes the form:

$$a_e = \frac{1}{6\alpha} A - \frac{2\beta}{A}$$
(Equation 7)

being A:

$$A = \left[\left(-108\gamma + 12 \sqrt{3\left(\frac{4\beta^3 + 27\gamma^2 \alpha}{\alpha} \right)} \right) \alpha^2 \right]^{\frac{1}{3}}$$
(Equation 8)

The strain energy release rate becomes then:

$$G_I = \frac{6P^2}{B^2 h} \left(\frac{2a_e^2}{h^2 E_f} + \frac{1}{5G} \right)$$
(Equation 9)

The compliance, *C*, is evaluated as the slope dΔ/dP (Δ = crack opening along the load line) recorded in the partial unloading performed at intervals during the test. Since the unloading, in general, do not point to the origin of the δ-P diagram because of inelastic phenomena at the crack tip and small adjustments/hysteresis in the load train, the simple ratio Δ/P may not represent correctly the compliance of the joint.

The results are reported in two separate diagrams for PLA and ABS. In each diagram, every set of data collects the results of the three repetitions. For both materials, failure was always interfacial due to the relatively low wettability and the intentional absence of surface preparation but cleaning, therefore the surface pattern left by FFF was apparently not able to compensate the inherent low adhesion of these

materials, except in the case of PLA_04 where in two out of the three specimens a partly cohesive failure was recorded: example of one of the cohesive rupture is reported in Figure 73.
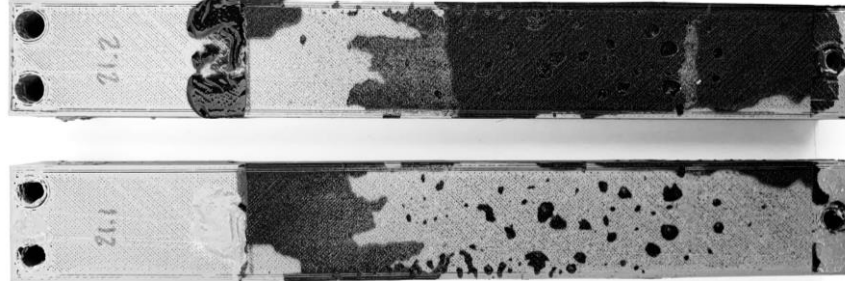

Figure 73: One of the three tested specimens for PLA_04 configuration, showing partially cohesive failure.

Another point common to all experiments is that a more or less steep R-curve was present that does not come to a steady-state value in the range of crack propagation tested. It is possible that the size of the specimen, which was defined according to printing limitations, e.g. 3D printer build volume, was not long enough to allow a crack propagation sufficient to reach a plateau of fracture toughness. Therefore, the discussion can be done only on the slope of the R-curve, with the underlying possibility that a higher slope would lead to a higher steady-state fracture toughness. Results for PLA specimens, reported in Figure 74, show similar value of fracture toughness at the beginning of crack propagation in all cases, while the maximum rate of increase of fracture toughness is obtained with specimen PLA_04 (maximum tensile strength, flexural modulus) whilst PLA_03 (minimum wettability and tensile strength) presents the lowest values. Considering ABS joints, from Figure 75 it can be noticed that all the configurations show both similar values at the beginning of propagation and the R-curve slopes are not much different from each other, giving in fact a unique, large scatter band. Therefore, ABS joints fracture toughness is little influenced by printer setup. Looking more closely at the linear regression of the single configurations, higher G_{IC} corresponds to ABS_01 and ABS_06 (the two configurations with the highest values of roughness) while ABS_04 (minimum wettability) present instead the lower values. This means that, alike for PLA, wettability must be maximized but the roughness seems also to play some role in this case, though the large scatter cannot afford a definitive conclusion about this point.
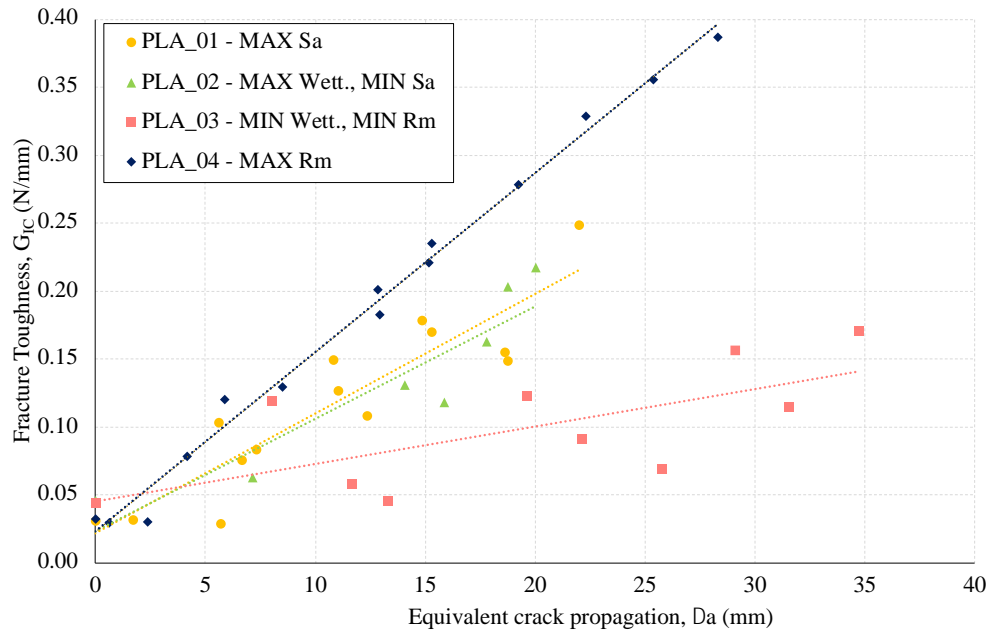
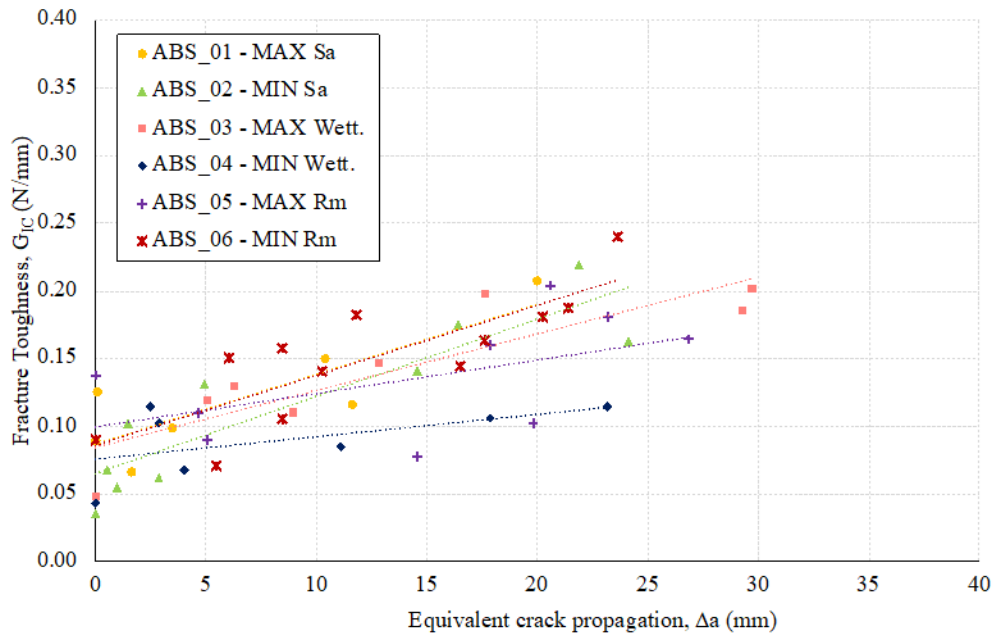Figure 74: Fracture toughness values for PLA adherends.

Figure 75: Fracture toughness values for ABS adherends.

4.3 Discussion and general remarks

This chapter explored the influence of the adherends surface and strength/stiffness characteristics obtained by varying the FFF printing parameters. In particular, the influence of extruder temperature, deposition speed and layer thickness, on the Mode I fracture toughness of bonded joints of two different FFF materials, PLA and ABS was assessed. Combinations of parameters giving maximum and minimum values of the surface roughness, respectively, wettability and tensile strength of the adherends were used to manufacture specimens DCB joints. For both materials, failure was found to be interfacial, meaning that the surface pattern left by FFF could not compensate the inherent low adhesion except in one case (PLA with maximum-tensile-strength-printing set-up), where two out of the three specimens exhibited a partly cohesive failure. All experiments were characterized by a more or less steep R-curve that does not come to a steady-state value in the range of crack propagation tested (Figure 74, Figure 75). A conclusion can be therefore drawn only on the slope of the R-curve, with the underlying possibility that a higher slope would lead to a higher steady-state fracture toughness. Under these conditions, in the case of PLA, a noticeable dependence on the printing parameters was found, where the strength (stiffness) and the wettability are most influential. In the case of ABS instead, it was much more difficult to distinguish a trend since the results of the experiments seem to fall into a unique, large scatter band. However, zooming on the values of each test, again wettability has to be maximized but the roughness seems also to play a role for this material. For both materials, the joints showed a positive dependence of fracture toughness on crack growth (R-curve), that is, more pronounced in the case of PLA.

Since for PLA or ABS adherends the R-curve resulted more or less steep depending on the printing parameters, it can be concluded that FFF parameters are indeed bonded joint design factors. This conclusion adds a new aspect to the design of bonded joints of polymeric FFF adherends. In fact, most works in the literature, as summarized in Chapter 2, used AM to shape or give a stiffness gradation to the adherends in order to improve the strength. However, this approach requires in general a non-trivial numerical study, customized printers and a non-commercial setup, to actually obtain a performance improvement and avoid premature joint failure.

As final general remark of Chapter 4 it can be stated that joint performance improvement can be found by operating on the build setup of the 3D printer.

Design for Additive Manufacturing applied to surface modifications for bonded joints

Chapter 5

Surface modifications for AM adherends

The work presented in this chapter, based on paper [183], addresses need of surface preparation to improve the performance of adhesively bonded 3D printed adherends obtained using FFF.

In particular, mechanical abrasion and two different plasma pre-treatments, i.e., atmospheric pressure plasma APP and low pressure plasma LPP, were compared through the qualitative analysis of surface wettability, using static and dynamic contact angle measurements, and the quantitative evaluation of surface roughness measured using optical profilometry. In addition, mechanical tests were carried out using the single lap joint configuration and the interaction between the treated AM substrates and three different adhesive materials, epoxy, polyurethane and modified silane, were carefully ascertained.

The results indicated that the plasma process at low pressure enabled a substantial decrease of contact angle ($\theta < 10^o$), with little modifications of surface morphology and topography with respect to the reference solvent cleaned surface ($\theta > 80^o$). The improved wetting was accompanied by a relevant increase in the joint strength. The actual mechanism of fracture shifted from adhesive failure, typical of solvent cleaned and abraded surfaces, to full cohesive failure within either the substrates of the adhesive layer. Besides, a strong influence of the adhesive selected for manufacturing was reported. Indeed, using a tough bi-component epoxy adhesive in conjunction with the LPP pre-treatment led to substrate failure, representing the largest possible enhancement of joint strength. The shear strength was over 300% of that obtained with reference solvent cleaned, and 80% larger than that recorded on abraded surfaces.

Surface modifications for AM adherends

5.1 Background and motivations

As discussed in Chapter 1 and 2, several solutions were explored to enhance the performance of adhesively bonded joints comprising 3D printed plastic substrates. AM ability to craft components with complex shapes provided additional scope for research, and novel ideas were proposed to pursue enhanced dissipation in the course of failure, such as tailoring the stiffness of the adhesive [41] and the substrates [35,44]. Moreover, shaping the mating surfaces to enable beneficial mechanical interlocking is another relevant point of advantage for joining difficult to bond materials, such as PA [29] or ABS [21] substrates. In Chapter 4 the feasibility of the use of printing parameters to affect the surface properties was validated. Yet, the reliability of adhesively bonded plastics ultimately depends on surface preparation. Regardless of the joint design, surface preparation is critical to establish interfacial adhesion and largely determines joint strength and overall reliability [184]. The need for proper surface pre-treatment is even more critical for non-polar plastics materials featuring low surface energy [16]. Recent works indicated that abrasion with emery paper could enhance adhesion and promoted cohesive failure in adhesively bonded 3D printed plastics [185]. However, it is also widely recognized that plasma pre-treatments can be very effective, as also assessed in Chapter 3. Indeed, plasma pre-treatments, are controllable and reproducible processes that allows improving interfacial interactions and joint strength for materials that are difficult to bond [186–191]. An adequately designed plasma pre-treatment can increase the mechanical strength of adhesive bonded ABS joints by modifying surface morphology, wettability, and chemical composition [186]. The most significant effects determined by the interaction between a plasma and the polymer surface include ablation, crosslinking, cleaning, and activation [187]. Concerning atmospheric pressure plasma APP pre-treatment, Ku et al. [188] performed an experimental campaign on polypropylene substrates. The APP process can increase surface roughness and decrease the contact angle. Besides, a concurrent rise in maximum shear load was reported. Abenojar et al. [189] investigated the effects of the atmospheric plasma pre-treatment parameters on polycarbonate (PC) and ABS that were chemically formulated to be processed by injection molding. They noted that contact angle values measured with a droplet of water changed after the APP pre-treatment as a function of the pre-treatment speed. The APP chemical modification was studied using X-ray photoelectron spectroscopy (XPS), and the investigation stated that the response was affected by the chemical composition, especially by the additives. The polymer formulation, often tuned for the manufacturing process, can affect the treated surface response to the plasma. Noeske et al. [190] assessed the importance of the distance between the target polymeric surface and the nozzle. Considering the results obtained on five different polymeric substrates, they concluded that the optimal value for the distance that yields the best results exists.

120

Concerning low pressure plasma LPP pre-treatment, the most relevant process parameters are the working gas, the power, and the exposure time. Mandolfino et al. [191] studied the most suitable process setups to improve bonding strength for different polymers using a radio frequency low-pressure plasma (Gambetti Kenologia, Italy). It was found that the mid-range value of the parameters gives the best performance in terms of improvement of contact angle and shear strength tests. Although a significant body of literature work focused on adhesive bonding of plastics, surface preparation for 3D printed components is a topic that still deserves further attention because of printed polymers unique properties [150], as discussed in the previous chapters. Optimizing the surface properties and adhesion may significantly improve the mechanical performance of additive manufactured assemblies [37].

In this chapter, the focus was placed on the analysis of adhesive joints comprising ABS substrates manufactured using FFF. Three distinct surface preparation methods were compared, including mechanical abrasion and plasma pre-treatments, APP, and LPP. The comparative analysis also includes three different kinds of structural adhesives, which feature relatively distinct mechanical behaviour.

5.2 Industrial surface preparations in adhesive bonding of additive manufactured substrates

In this section the experimental work carried out to investigate efficacy of some of the most industrial used surface modifications for AM adherends is presented. The FFF technology was used for the manufacturing of ABS adherends. The 3D printer Wasp 4070 Industrial (Wasp, Massa Lombarda) and ABS filaments (Sienoc, Taiwan, China) were employed throughout this study. The specimens were modelled in Creo Parametric 2.0 while the slicing was performed with Ultimaker Cura (ver. 3.5.1). Using the methodology presented in Chapter 4, preliminary experiments were carried out according to a Taguchi L_9 OA to investigate the effect of 3D printing setup parameters, such as the layer height, the nozzle temperature, and the deposition speed, on the tensile strength of the 3D printed ABS. As before, three levels for each of the above variables were considered, including their interactions. Minimum, mean and maximum of each variable were selected based on the specifications disclosed by the manufacturer. The obtained data was finally analysed by means ANOVA that yielded the processing parameters reported in Table 22 [150].

Table 22: Manufacturing parameters used for the FFF adherends.

Printing parameters	
Layer height (mm)	0.25
Nozzle temperature (°C)	250
Print speed (mm/s)	120

The mechanical properties of the 3D printed ABS were carefully determined through tensile tests performed following the procedure and recommendations reported in the standard UNI EN ISO 527-2:2012. The testing machine Zwick Pro Line (Zwick Roell, Genoa, Italy) fitted with a 10 kN load cell was employed to perform displacement-controlled tensile tests at a cross-head displacement rate of 5 mm/min. A schematic of the dogbone specimens employed in the experiments is given in Figure 76. Five repetition of the test were carried out to ensure consistency of the experimental data, and the obtained results read as follows: tensile modulus, E=(2.32 ±0.17) GPa, ultimate stress, S_{ut}=(33 ± 0.7) MPa, and strain at failure, e_f=(5.1 ± 0.9) %, respectively. These results are consistent with the data obtained by Kariz et al. [28] performing tests on ABS FFF specimens, and very close to that obtained on injection-molded ABS specimens [192].
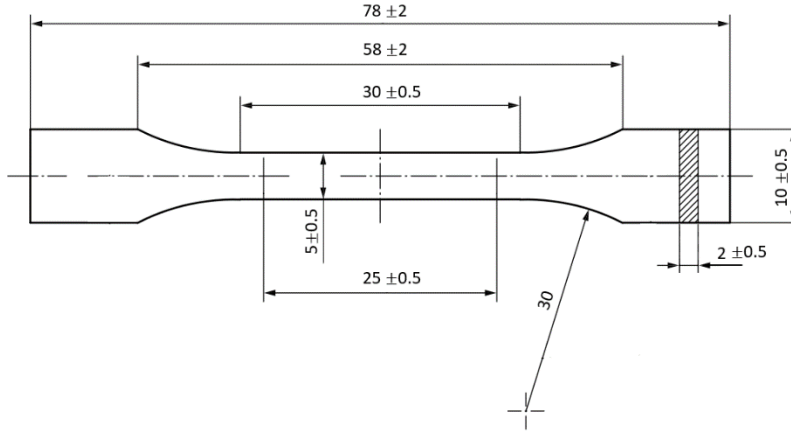
Figure 76: Dimensions of the 3D printed dogbone specimen manufactured according to UNI EN ISO 527-2:2012

Adhesive bonded joints were prepared using three distinct commercial adhesives provided by Henkel Italia Srl (Milan, Italy), i.e., the Loctite EA 9466 bi-component epoxy adhesive, the Teroson 9225 polyurethane adhesive, and the Teroson MS 9399 two-component adhesive based on silane modified polymers. All these adhesives can be successfully cured at room temperature, thus avoiding exposure of the substrates to potentially detrimental thermal effects. The viscosity of the adhesives was determined using a rotational and oscillatory rheometer Anton Paar Physica MCR 301 (Anton Paar Italia S.r.l, Torino) equipped with a truncated cone and plate geometry (50 mm in diameter, 2° of angle, gap of 0.210 mm between the rotor and the plate). Besides, the mechanical properties of the adhesives, including the tensile modulus and the ultimate strength, were determined by performing tensile tests on dogbone specimens obtained using a mold. Notice that the specimens had similar dimensions of that reported earlier in Figure 76 (UNI EN ISO 527-2:2012). Five specimens for each adhesive type were tested and the results are summarized in Table 23.

Table 23: Summary of the investigated adhesives and relevant info, from the datasheet and experimental assessed, for selection.

Adhesive	Technology	Fixture time (s) (ISO 4587:2003)	Cure time (hours) at 22 °C	Tensile modulus (MPa)	Ultimate tensile strength (MPa)	Viscosity (Pa*s)	
Loctite EA 9466	Epoxy polymer	10800	24	2190.4 ± 13.7	39.2 ± 1.6	A component	28
						B component	5.8
Teroson 9225	Polyurethane polymer	1800	5	576.9 ± 16.1	13.3 ± 0.3	A component	800
						B component	60
Teroson MS 9399	Silane-modified polymer	30	24	9.3 ± 0.2	3.1 ± 0.2	A component	10
						B component	20

The surface pre-treatments employed in the present chapter are summarized in Table 24. The reference surface preparation is represented by a solvent cleaning process (Loctite SF7063, Henkel, Milan) whereas the substrates are wiped along the direction of the major dimension with a linen cloth. The solvent cleaning process was used to establish reference conditions for subsequent comparative analyses. Besides, mechanical abrasion using SiC emery paper, as well as APP and LPP.

Table 24: Surface treatments investigated for the AM adherends.

Treatment	Parameters
Cleaning	Solvent degreasing and wiped along the main direction
Abrasion	Solvent degreasing, then abraded with a SiC emery paper #320 orthogonal respect to the main direction as described in ASTM D2093-03 (17), followed by further solvent degreasing
APP	Process and cooling gas: air (29 and 24 l/min respectively), power 300 W, 10 mm nozzle adherend distance, nozzle speed 50 mm/s
LPP	Solvent degreasing. Plasma parameters: working gas Air flow rate of 25 cm^3/min, power 150 W, exposure time 180 s, pressure 0.6 mbar

The abrasion treatment, that is a standard method for surface preparation of several polymeric substrates, has been performed according to the guidelines reported in the ASTM D2093-03(17). Then, two different plasma treatments were carried out. In particular, APP treatment (Figure 77 a) was performed using a radio frequency low pressure plasma (Gambetti Kenologia, Italy) system with a generator power equal to 300 W. Air was used as a processing and cooling gas.

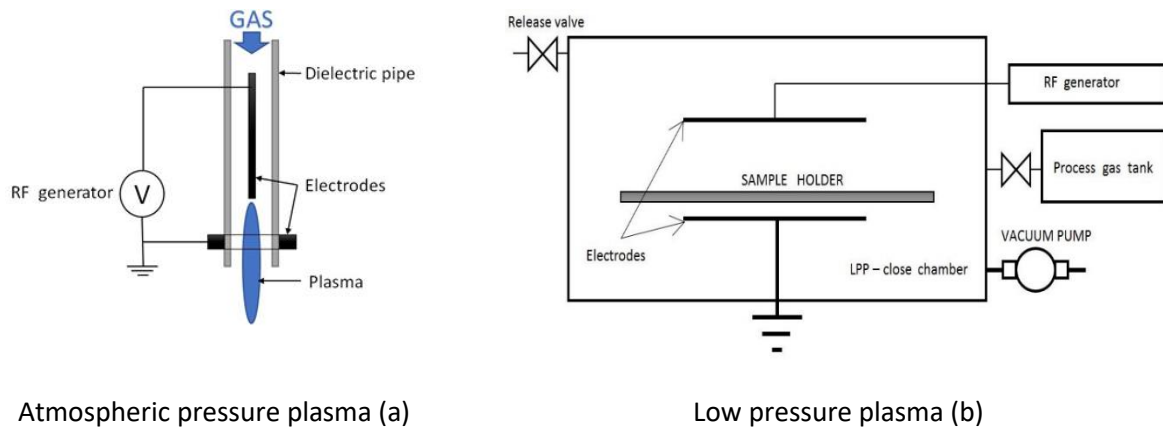Atmospheric pressure plasma (a)   Low pressure plasma (b)

Figure 77: Plasma functional diagrams.

The target surface of the samples received plasma treatment by moving the adherend following a grid pattern, with a spacing equal to 3 mm, using a custom-made translational x-y stage (Figure 78). The chosen parameters were selected by optimizing the procedure as suggested by Noeske et al. [190] and

Bagiatis et al. [193], in particular using a distance of 10 mm between the nozzle and the treated surface, and line speed equal to 50 mm/s.
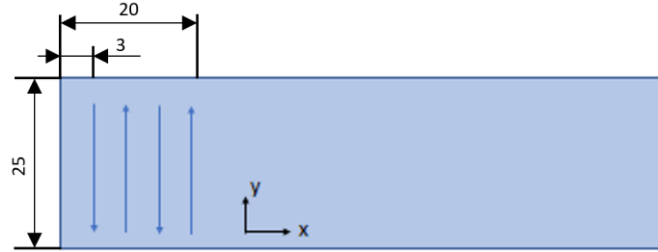

Figure 78: APP plasma jet pattern on the ABS adherend.

LPP treatment (Figure 77 b) was performed with a radio frequency RF generator (Gambetti Tucano, Italy) operating at 13.56 MHz and maximum power of 200 W. On the basis of previous experience, presented in the work of Mandolfino et al. [191], the treatment was performed using a power level of 150 W and an exposure time of 300 s. A flow rate of 0.025 SLM and a process pressure of 0.6 mbar were employed throughout the process.

The single lap joints were designed according to the Standard ASTM D3163-01(14) and a schematic of the joint with relevant dimensions is reported in Figure 79. Built-in alignment tabs were directly 3D printed with the ABS substrates. The adherends were subjected to the surface pre-treatments specified in Table 24. After surface the pre-treatment, the joints were assembled using jig to ensure a 0.25 mm bondline thickness. Curing and adhesive hardening was achieved following the guidelines specified in the adhesive datasheets. Mechanical tests were performed at a test speed of 1.3 mm/min and five repetitions for each sample configuration were done.
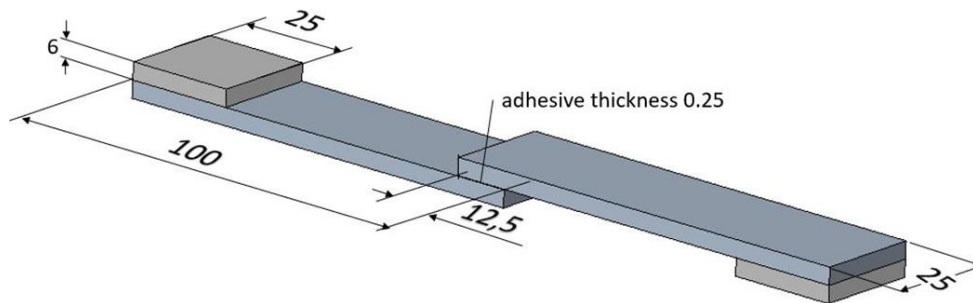

Figure 79: Single lap shear test specimen geometry, the dimensions are expressed in mm.

126

The joints average shear strength (τ_{ave}) was determined using the following equation:

$$\tau_{av} = \frac{F}{A_0}$$
Equation 10

where A_0 was the overlap area, and F_{max} is the maximum load recorded prior to failure. For reference, monolithic single lap specimen (*i.e.*, no adhesive bonding) were 3D printed and featured the same geometry of adhesive bonded single lap joints (Figure 79).

In order to access both the morphology and topography of as produced and treated ABS, surface analysis was performed with an optical profilometer (CCI Taylor-Hobson 3D), and following the procedures reported in the EN ISO 25178 - 600:2019. The S_a as well as the skewness (S_{sk}) were evaluated. These values obtained on the as-produced surfaces were used as a reference to evaluate the effect of the different surface pre-treatments.

Static and dynamic contact angles were determined to provide a characterization of surface wetting and supplement the results of mechanical tests, and the analysis of the associated mechanisms of failure Measurements were performed immediately after the surface preparation in laboratory environment at room temperature (23°C) and relative humidity (RH) 70 %. The static contact angle of metastable droplets of demineralized water placed on the target surfaces was determined from drop shape analysis. Snapshots of 2 µl calibrated water drops were taken 10 seconds after drop deposition using a microscope. For each pre-treatment, ten measurements were carried out by placing the drops at different locations across the surface, as schematically depicted in Figure 80.
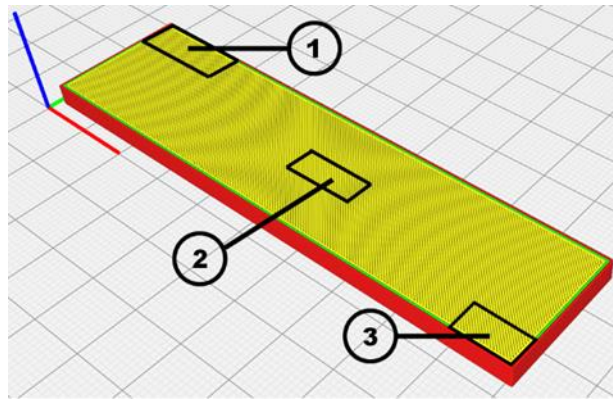

Figure 80: Measurement positions used to obtain a relevant value of the layer surface.

The dynamic contact angle was determined based on the volume changing method and using a programmable Syringe Pump (AL-1000, Word Precision Instrument, USA). A drop of 2 μl of demineralised water placed on the surface was gradually increased in volume with a rate of 0.2 μl/s for 60 seconds, and then the volume was reduced at the same rate for other 60 seconds. Measurements were performed for all pre-treatments reported in Table 24, except for the LPP as for this high hydrophilic sample the deposition of a drop on its surface produces the formation of a thin film and then the evolution of the drop profile cannot be evaluated. Typical snapshots taken during the experiments are reported in Figure 81. The advancing and the receding contact angle were determined from drop shape analysis. Three repetitions on four different samples for each surface pre-treatment were performed.
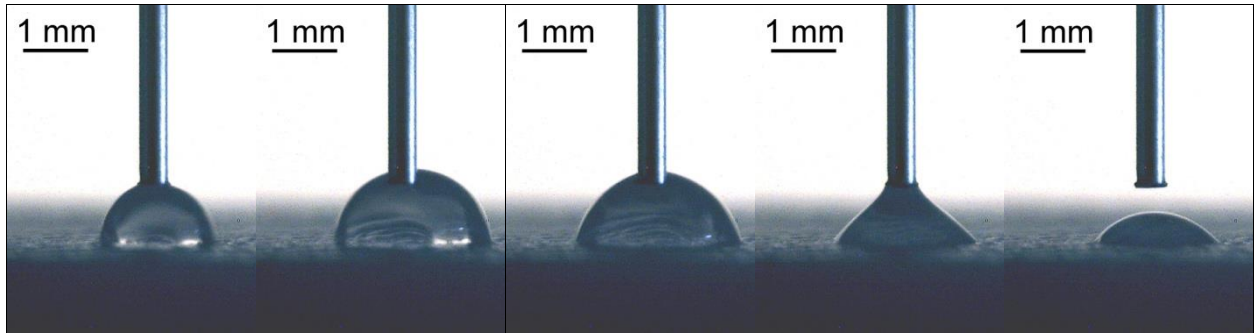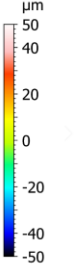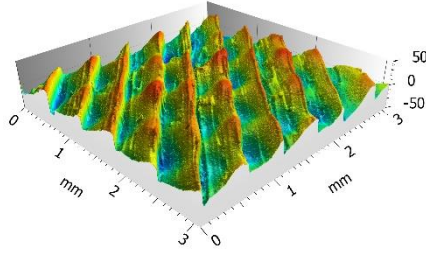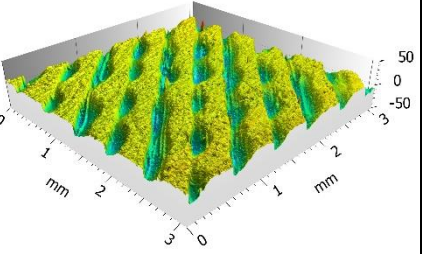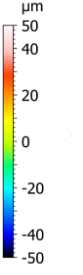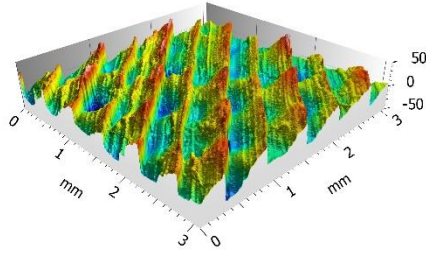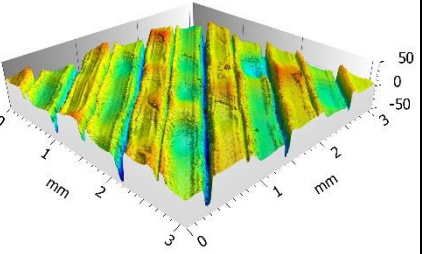

Figure 81: Dynamic contact angle, representative sequence of the volume drop variation during the test.

5.3 Appraisal of the industrial surface preparations in adhesive bonding of additive manufactured substrate

In order to investigate the effects of different pre-treatments on surface roughness, the S_a was determined on the ABS surface considering the locations highlighted in Figure 80, as showed in the previous section. The mean values of repeated measurements are reported in Table 25 along with the values S_{sk}, relevant because it represents the degree of bias of the roughness shape. It is worth noting that the height distribution can be symmetrical around the mean plane (S_{sk}=0) as well as skewed above (S_{sk}<0) or below (S_{sk}>0) the mean plane. Comparing the data reported in Table 25 with the characteristics of the reference surface (solvent cleaned), the following conclusions can be drawn. A significant reduction of roughness occurs after mechanical abrasion because the pre-treatment leads to flattening of surface asperities. As a result, the obtained S_a is the lowest among all treated surface, and a negative value of S_{sk} also follows since the height distribution is skewed below the mean plane.

129

Table 25: Mean values and standard deviation of roughness after the treatments.

Treatment	Solvent Cleaned		Abrasion	
	Average	Std. Dev	Average	Std. Dev
Skewness	-0.05	0.01	-1.39	0.2
S_a (µm)	11.09	1.5	5.24	1.1

Treatment	APP		LPP	
	Average	Std. Dev	Average	Std. Dev
Skewness	0.22	0.05	-0.56	0.15
S_a (µm)	11.06	0.79	9.51	0.33

The analysis of S_a and S_{sk} suggests that APP pre-treatment provides surface morphology almost unchanged compared to the reference solvent cleaned ABS. However, in this case the height distribution is skewed above the mean plane. The LPP pre-treatment lowers S_a and S_{sk} but compared to mechanical abrasion it seems to affect both peaks and valleys of the target surface and had a smoothing effect. Interestingly, this behaviour is in contrast with the increase of S_a observed for injection molded specimens, as reported by

Mandolfino et al. [191]. The different response for the same pre-treatment can be explained considering the surface morphology before the pre-treatment. Injection molded specimens are macroscopically smooth and the LPP pre-treatment slightly increase the roughness. On the opposite, the FFF specimens are macroscopically rough and the LPP pre-treatment contributes to the flattening of the crests. It is worth noting that the peculiar FFF texture is driven by the process parameters [150] and by the deposition pattern. In particular, in this work the direction of the surface features is parallel to the fused filament deposition direction (±45° with respect to the loading direction).

The naturally low wettability of ABS, that normally exhibits contact angles around 90°, can be substantially modified using plasma pre-treatment and, particularly the LPP, as reported in [192]. Modification of surface wettability involves both chemical and morphological aspects of a surface. For metals, the morphological aspect is more relevant [194], since the influence of the surface chemistry varies greatly from metal to metal, while for polymers, the formation of polar oxygen-containing groups, such as C-O, C=O, and O-C=O, can modify surface wettability to a large extent. Examples are reported by Mandolfino et al. [191] and Abenojar et al. [189], where XPS was performed on both untreated and APP-treated PA and ABS. A remarkable increase of O/C ratio after pre-treatment was recorded, which could explain the observed surface hydrophilicity.

The average values of the static contact angles and of the dynamic contact angles for each surface pre-treatment are reported in Figure 82.

(a)   (b)
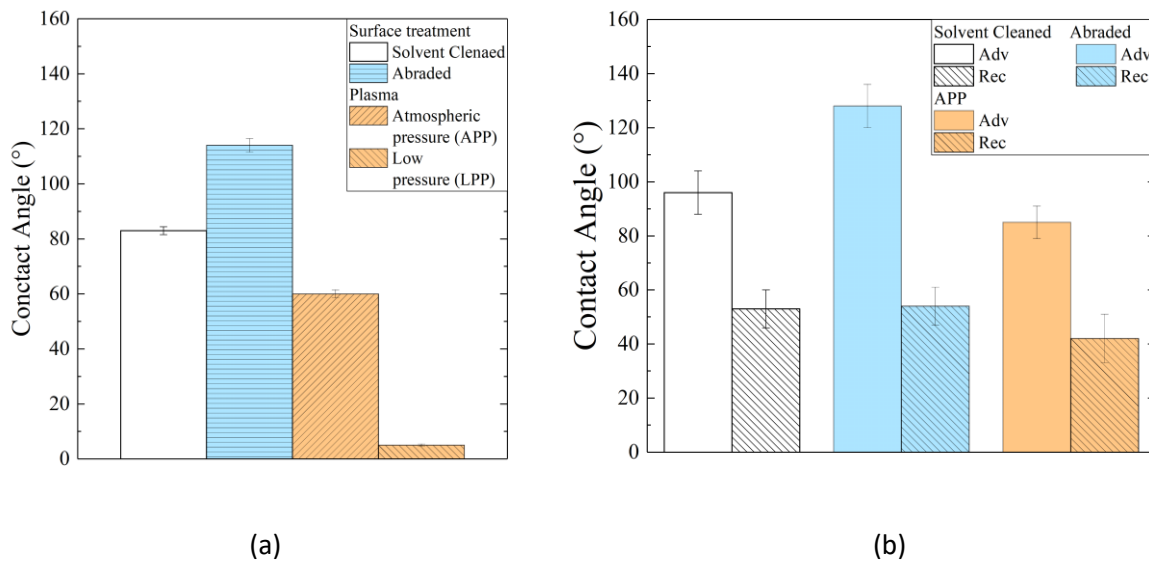
Figure 82: Contact angles measured after the surface treatments, (a) static contact angles, (b) dynamic contact angles, advancing Adv and receding Rec.

LPP pre-treatment induces a dramatic decrease of contact angle that prevented dynamic contact angle measurements: therefore, in Figure 82b, only the measurements concerning the surface APP treated are reported. This is likely due to the chemical modification induced by plasma, as observed also on injection molded polymers [192], but also to the ability of the process to reach the valleys of the surface morphology which ensures that large portions of the target receive pre-treatment. Mechanical abrasion contributed to an apparent increase of static contact angle with respect to the solvent cleaned surface. However, considering a contact angle of the reference slightly different from 90°, an explanation of the remarkable reduction of the wettability of the surface with a change in the roughness cannot be found in the Wenzel model [195]. Moreover, the validity of the Wenzel equation implies that the drop must be sufficiently large compared with the roughness scale, while in this case the maps of surface shows a horizontal distribution of the peaks and of the valleys of about 0.5 mm. The comparison of the receding contact angle between the two treated surfaces evidences an average value of 53° in both the samples and thus no differences can be observed. The contact angle hysteresis, namely the difference between the advancing and the receding contact angles, detects a metastability of the drop connected with the slower kinetic of the liquid penetration in the surface capillarity of the abraded sample with respect to the larger one of the reference specimens [196]. The abrasion with emery paper #320 produces a reduction of the asperities at mesoscale level, limited to the peaks, but not changes are introduced in the valleys and an increase of the roughness are created at microscale. The higher hysteresis found in the abraded surface with respect to the one treated with the solvent is connected thus with a higher microscale roughness [196].

Now, the experimental results of the single lap shear tests are reported. The shear strength of the adhesive joint with solvent cleaned surfaces has been included as a reference to evaluate the effects of the other surface modifications. Moreover, the shear strength of the monolithic samples (no adhesive bonding), that was equal to (7.6 ±0.2) MPa, has been also included in the comparative analysis. Lap shear test results, obtained using the epoxy adhesive Loctite 9466, are reported in Figure 83.

132
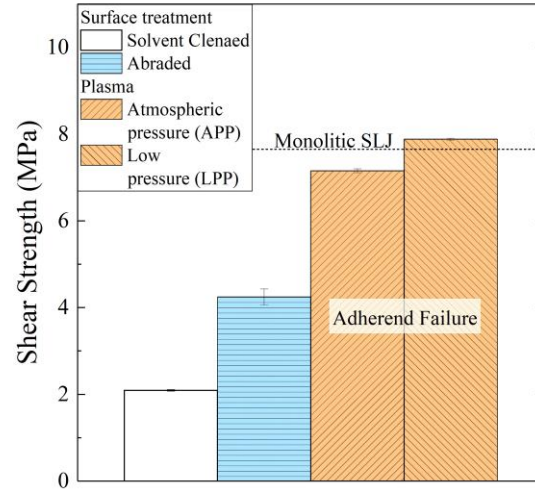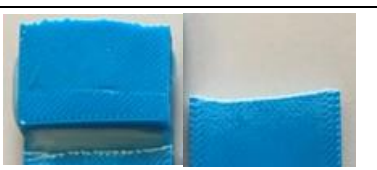
Figure 83: Epoxy adhesive lap shear test results.

In particular, a significant increase in shear strength was achieved using both plasma pre-treatments. The mechanical strength after LPP is almost four times higher than that of solvent wiped surfaces and two times higher than that of abraded surfaces. Mechanical abrasion reduces surface roughness, because it flattens the surface asperities at the mesoscale level and exposes the previously under surface polymeric material supposedly free of impurities and contaminations. These impurities are not necessarily removed by a simple solvent cleaning step and the establishment of weaker interfacial interactions may explain the poor performance of the reference surfaces with respect to the mechanical abraded interfaces. The increase of the water contact angle and of the hysteresis contact angle can be attributed with an increase of the coarseness of the surface abraded at macroscopic range [196]. The failure surfaces of single lap joints bonded with the bi-component epoxy adhesive are reported in Table 26. The survey confirmed the effectiveness of plasma pre-treatments. While solvent cleaning and abrasion with emery paper resulted in adhesive failure, plasma-treated specimens exhibited failure of the substrates, representing the maximum performance improvement.

Table 26: Epoxy 9466 failure surfaces, nominal bonding area is 25×12.5 mm^2.

	Treatment	Failure mode	Failure surfaces
Epoxy adhesive	Cleaned	adhesive	
	Abraded	adhesive	
	APP	adherend	
	LPP	adherend	

The shear strength of single lap joint bonded with the polyurethane adhesive is reported in Figure 84. The results demonstrate that a substantial increase in shear strength can be achieved with any surface pre-treatment other than solvent cleaning. The best results were obtained with low pressure plasma pre-treatment whose corresponding average joint strength was more than three times higher than the baseline surface.
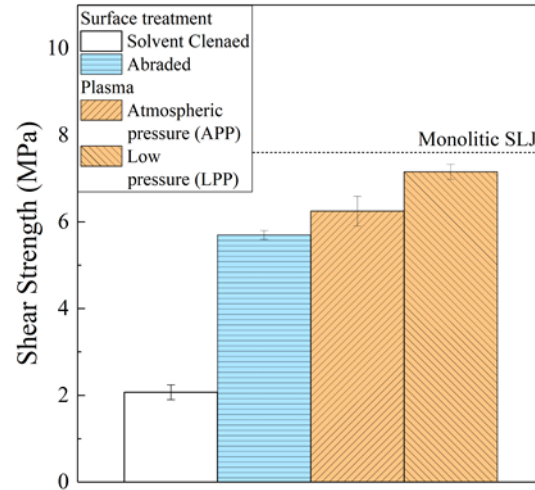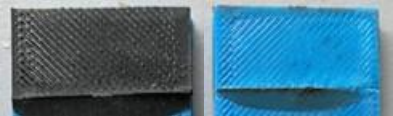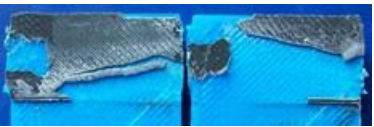
Figure 84: Polyurethane adhesive lap shear test results*.*

Additional comments can be drawn from the analysis of failure surfaces reported in Table 27. Solvent cleaning leads to adhesive failure and low shear strength. Mechanical abrasion and atmospheric pressure plasma could provide much higher joint strength but still displayed adhesive failure. However, the failure surfaces of joints subjected to APP pre-treatment have also shown some degree of adhesive whitening, indicating the occurrence of large strains within the adhesive before failure and, thus, improved adhesion. On the other hand, LPP has led to the highest joint strength in conjunction with cohesive failure, emphasizing a higher efficiency.

Table 27: Polyurethane 9225 failure surfaces, nominal bonding area is 25×12.5 mm^2.

	Treatment	Failure mode	Failure surfaces
Polyurethane adhesive	Cleaned	adhesive	
	Abraded	adhesive	
	APP	adhesive	
	LPP	cohesive	

In Figure 85 the results of the lap shear tests for the Silane-modified Teroson 9399 adhesive joints are reported. Since it is a silane-modified adhesive, as expected, lower shear strength compared to other adhesives were recorded.
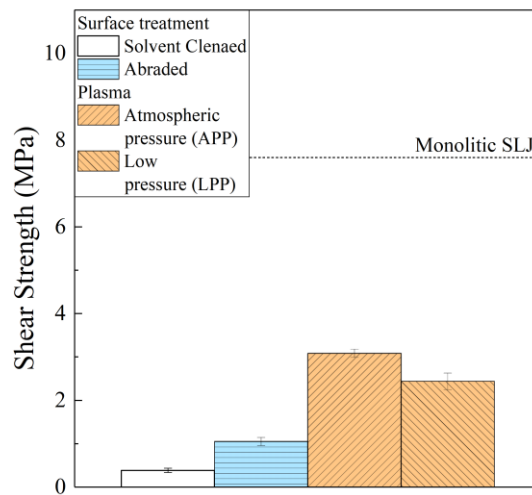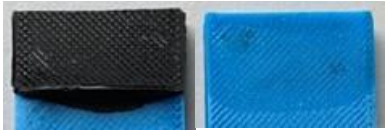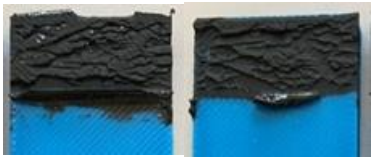
Figure 85: Silane-modified lap shear test results.

From an analysis of the failure surfaces reported in Table 28, it is observed that solvent cleaning and abrasion are unable to promote cohesive failure, indeed, an adhesive failure was observed in all tests. On the contrary, both plasma pre-treatments led to cohesive failure of the adhesive.

Table 28: Silane-modified 9399 failure surfaces, nominal bonding area is 25×12.5 mm^2.

	Treatment	Failure mode	Failure surfaces
Silane-modified adhesive	Cleaned	Adhesive	
	Abraded	Adhesive	
	APP	Adhesive	
	LPP	Cohesive	

In order to summarize and compare the obtained results, the average shear stresses as a function of the surface pre-treatments examined in this work is reported in Table 29. The percentage variations provided in the table represent the improvements with respect to control samples. It is inferred that the shear strength of adhesive joints subjected to solvent cleaned are quite low and, as such, may be unable to ensure reliability of bonded assemblies in structural applications. This conclusion is in line with recent works by Espalin et al. [114] and Spaggiari et al. [185]. The visual inspection of failure surfaces suggests that solvent cleaning leads to purely adhesive failure. Mechanical abrasion provided a remarkable improvement of the shear strength up to +285%. As discussed earlier, this pre-treatment decreases surface roughness removing a thin superficial layer of material that usually embeds impurities, such as additives used to improve extrusion through the nozzle, and contaminations. Although the pre-treatment may help in establishing stronger interfacial interactions, in this work the extent of the improvement was not enough to promote cohesive failure. In addition, being AM typically used to make hollow and/or

137

lattice structures with complex geometries featuring thin walls, the risk of damage associated to subsequent mechanical abrasion could be a factor that should be accounted for while selecting a surface pre-treatment method. Moreover, in contrast to plasma technology, mechanical pre-treatments are less attractive in terms of both automation and repeatability. Regarding plasma pre-treatments, the increase of shear strength always exceed 300%. While adhesive joints subjected to plasma pre-treatment and bonded with the epoxy adhesive have always shown failure within the substrates, the polyurethane bonded joints could not achieve comparable performances. The best result was obtained with the LPP pre-treatment because it led to cohesive failure. Finally, the performances of the silane modified adhesive were mainly limited by the mechanical properties of the adhesive itself. Consistently with the other batches of samples, the plasma pre-treatments provided the best results leading to cohesive failure. The results were in good agreement with those reported in previous works [192], and further support the effectiveness of plasma pre-treatment in improving the strength of adhesive bonded 3D printed ABS.

Table 29: Results of τ_{av} for the different surface treatment conditions and increment against control samples.

Adhesive	Surface treatment	τ_{ave} (MPa)	Standard deviation (MPa)	Increment
Epoxy	Cleaning	2.1	0.03	Reference
	Abrasion	4.2	0.04	200%
	APP	7.2*	0.09	343%
	LPP	7.9*	0.05	376%
Polyurethane	Cleaning	2	0.34	Reference
	Abrasion	5.7	0.21	285%
	APP	6.2	0.69	310%
	LPP	7.2	0.35	360%
Silane-modified	Cleaning	0.4	0.09	Reference
	Abrasion	1.1	0.18	275%
	APP	3.1	0.19	775%
	LPP	2.4	0.38	600%
*failure occurred in the adherends				

5.4 Discussion and general remarks

In this chapter, the experimental characterization of SLJs with substrates manufactured using FFF was carried out and the effects of various surface preparation methods and adhesive materials were examined. Three surface pre-treatments were considered, i.e., mechanical abrasion with emery paper, atmospheric pressure plasma and low-pressure plasma.

Morphology analysis based on both arithmetic mean height and skewness pointed out that the three different pre-treatments had different effect on the texture created by the FFF material deposition. The APP (S_{sk} = 0.22 μm and S_a = 11.06 μm) barely modified the surface morphology from the baseline cleaned surface; mechanical abrasion flattened the surface peaks and decreased surface roughness (S_a = 5.24 μm), while the LPP smoothed both peak and valleys leading to S_a = 9.51 μm and S_{sk} = -0.56.

Wettability has been assessed qualitatively determining both the static and dynamic contact angles. The 3D printed ABS exhibited contact angles around 90° after solvent cleaning; however, it increased following to the mechanical abrasion, to which corresponded also a growth of the difference between the advancing and the receding contact angle; this increase of the dynamic contact angle hysteresis is induced by the grinding action that, while reduce the asperities of the surface at mesoscale level, however causes an increase of microscale roughness of the specimen. Finally, values lower than 10º were observed after LPP, such decrease may be associated to the formation of oxygen-containing polar groups.

The results of mechanical tests demonstrated that abrasion with emery paper could increase the joint strength with respect to baseline solvent cleaning in a range between 200% and 285% and the visual assessment of failure surfaces revealed the occurrence of mechanical interlocking, but final failure was still interfacial. Plasma pre-treatments were proven to be the most effective and could promote cohesive failure within the adhesive layer (polyurethane and silane modified bonded joints), as well as substrate failure (epoxy bonded joints). The joint strength was increased remarkably and up to +775% with respect to solvent cleaning. In addition, the obtained results have shown that, for a given surface preparation, the mechanical behaviour is affected by the adhesive material employed for joint fabrication. For instance, adhesive joints with plasma treated surfaces and bonded with epoxy resin were characterized by adherend failure, which represents the largest possible increase in joint strength. Finally, considering that LPP and APP provided similar results, any recommendation about which one should be used will need to be based on additional considerations. The size and the shape of the component to be treated will play a role in that respect. For instance, the vacuum chamber has a limited working volume, while the plasma torch at atmospheric pressure can work also on complex surfaces.

Surface modifications for AM adherends

Chapter 6

Design for Additive Manufacturing and

Multi Material Additive Manufacturing

applied to joining processes

This chapter is based on paper [197], the presented work aims to explore innovative joining processes for additively manufactured components to overcome the drawbacks outlined in the previous chapters. In particular, the work presented in Chapter 6 focus on the feasibility of hybrid weld-bonded joints. After feasibility analysis, the performance of the hybrid joint is evaluated by comparison with the baseline bonded and welded joint configurations.

The novelty of the proposed solution lies in the fact that welding is achieved using a 3D printed material with conductive filaments, a solution derived from the use of embedded 3D printed circuits (direct printing) in the AM components. Direct printing can be used to obtain an accurate local control of the thermal cycle and to overcome geometrical limitations inherent to the process, as for example the need of an access for the welding tools.

The feasibility of the hybrid weld-bonded joint was assessed and, while for adhesive bonding the use of dedicated surface treatments was found to be necessary to improve the joint performance, the welding process was determined to be the most promising joining process, especially when directly integrated in a MMAM process.

6.1 Background and motivations

The new developments on Additive Manufacturing (AM) processes [198,199] and the wider availability of high performance reinforced materials [200,201] are enabling new AM industrial applications, as it was presented in the previous chapters. These developments are addressing the needs of various applications, including healthcare products [11,202], robotics [140,203], light weight and safe vehicle structures [204,205]. In general, AM industrial applications are convenient if highly optimized-for-the-application components are necessary.

In particular, in Chapter 2, on the basis of recent literature analysis, it was pointed out that some of the most promising technology and design technique advances are achieved by coupling the local control on the geometry with the local control on the materials properties [206,207]. This DfAM approach was used, for example, to create field driven lattice structures or to locally control the material properties at voxel size [200,208].

This design method belong to the DfAM concept [209] and one of DfAM aims is to integrate functions in the components geometry to achieve embedded multifunctionality [210], as shown in Chapter 3, or to obtaining controlled stiffness or again variable thermal and electrical conductivity [211].

Another focus of DfAM is that the widespread use of AM components creates a need for effective and practical joining processes, suitable to assemble these AM parts and create more complex final products.

Furthermore the nominally limitless design freedom, provided by the AM process features in some applications, could be not achievable due to the constrains of a 3D printer build volume, component placement and 3D printing parameters adjusted for printability instead of maximum performance [212]. However, as discussed in Chapter 4, printing parameters play a critical role on the AM processed properties and durability, as assessed by the data produced in Chapter 1. This is especially true when service loads in structural applications require the use of AM with long fibre reinforced materials. Therefore, in many cases it is convenient to decompose the component in optimized sub-assemblies to enable the choice of the optimal printing setup for the application, using the effect of the print parameters on the material as design variable, as investigated in Chapter 5. Moreover this approach addresses the limited building rate of AM process by performing multiple parallel builds [62,150,166,213].

While fastening and snap connections represent commonly encountered solutions for this issue, the use of adhesive bonding has been explored by several authors [107] as it provides a better distributed stress field that allows for higher joint performance and a larger degree of geometrical freedom in the design of the coupling interfaces (Chapter 3).

The work presented in this chapter is based on a simple consideration, i.e. most AM processes rely on thermoplastic polymers. Therefore, besides adhesive bonding other joining processes can be suitable. In literature there are several examples, mostly based on thermal welding, many of which have already been found to be effective for joining long fibre thermoplastic matrix reinforced materials [214]. Moreover, implementing DfAM for these processes can further explore the advantages of multi material additive manufacturing MMAM to include conductive reinforced polymers and direct writing [87,211,215–217] to embed circuits and heating elements through the thickness of the materials. The end result are components that can be joined together via the application of a controlled electric current. Other key advantages are the geometrical freedom obtainable in the weld zone, as no access for external tools is needed, and the improved control over the welding setup geometry, one of the most relevant process parameters [218]. Furthermore, these circuits and heating elements could also be used for structural monitoring and to enable self-healing (Figure 86), taking advantage of the knowledge on the failure mechanism of layered materials developed on components manufactured with other processes [123,219].
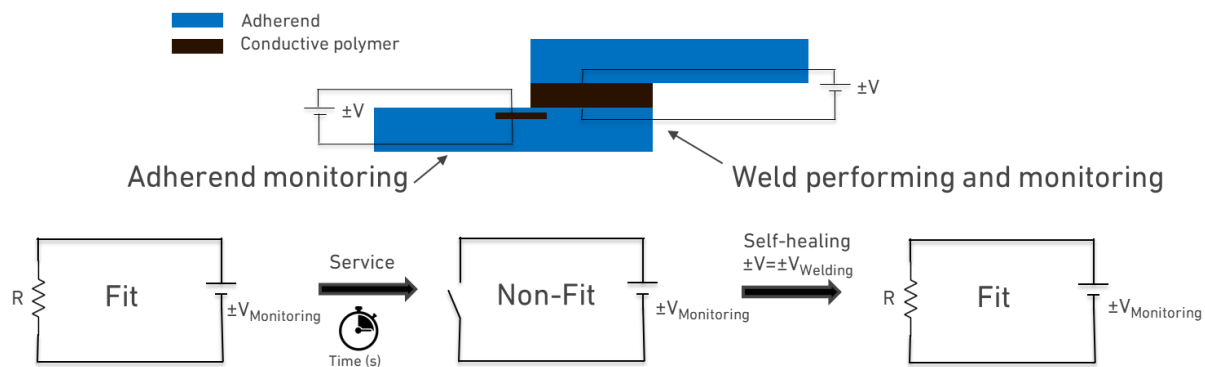
Figure 86: Concept of welding and self-healing using AM conductive material and embedded circuits.

Finally, taking into account the layered nature of AM processed materials and the current state of the art in bonding and welding joining processes, the use of AM opens the possibility to design and manufacture novel energy absorbing and crashworthy components. These components can combine different joining methodologies to enhance joint performance both under static and dynamic loading conditions [6,220], redistributing the loads.

6.2 Experimental set-up for hybrid weld-bonded joints feasibility assessment

An Ender 3 pro 3D printer (Creality, Shenzhen, China), equipped with 0.4 mm nozzle was used for the fabrication of the adherends using the FFF process. Two different PLA thermoplastic filaments were used, a bulk PLA by Sunlu for the adherends (Zhuhai sunlu industrial Co., Zhunhai, China) and a conductive PLA by ProtoPasta for the weld pads (ProtoPlant extrusion technology, Vancouver, Washington, USA). The conductive PLA was selected following the findings of Flowers et al. [216], which reports this material as suitable to manufacture resistors that could be used even to perform welding via joule heating. This is due to the relatively high resistivity ρ of the material that is equal to 12 $\Omega \cdot$cm. The printing parameters reported in Table 30 were used to manufacture the adherends. The mechanical properties of both PLA materials were characterized by manufacturing tensile specimens according to the ASTM D638 – 14, geometry type IV, with the printing set-up used for the adherends (Table 30) and selected according to the manufacturer specifications. The specimens were modelled in Creo Parametric 5.0 while the slicing was performed with Ultimaker Cura 4.6, imposing a correction factor to improve dimensional accuracy.

Table 30: Manufacturing parameters employed in the FFF process.

Printing parameters	
Layer height (mm)	0.2
Infill (%)	100
Deposition speed (mm/s)	60
Deposition pattern	lines
Nozzle temperature (°C)	220

All specimens were manufactured in the same position on the bed, aiming to enhance reproducibility, laid flatwise with crisscross material deposition ± 45° in the raster with respect to the loading direction, as shown in Figure 87, selected according to the works presented in the previous chapters [106,164,213]. Additional tensile test with unidirectional material deposition of 0° specimens were performed to obtain data on to model the adherends failure. After manufacturing, the adherends were degreased using isopropyl alcohol, wiping along the main direction.
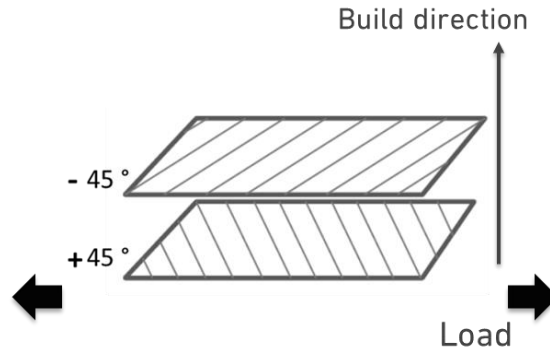
Figure 87: Material deposition pattern of the specimens.

The adhesive used in this work was the Teroson PU9225 by Henkel (Henkel Italia Srl, Milan, Italy), the same bicomponent polyurethane based adhesive used in Chapter 4, selected due to its mechanical properties, in particular to the adhesive and the PLA Young's modulus ratio, according to the work by Machado et al. [6]

Recent literature at the time of writing [107] and the work presented in Chapter 4 and Chapter 5, pointed out that, for bonded joints with AM adherends, surface modifications could be necessary to improve the adhesion. The surface energy evaluation was carried out on the AM adherends, in the overlap area, in order to take into account the effect of the surface morphology created by the manufacturing process [51,166]. The surface energy was assessed via contact angle measurements, using the equilibrium of the forces, as proposed by Young's equation [221] and the Owens-Wendt-Rabel-Kaelble (OWRK) method [222]. The contact angle measurements were performed using a OCA 15 goniometer (DataPhysics, Neurtek Instruments, Eibar, Spain) under ambient conditions, using three different liquids: water (polar liquid), ethylene glycol 55% (polar liquid) and n-hexadecane (nonpolar) as shown in [223]. The procedure was repeated after APP surface treatment. The APP treatment was carried out using Arcotec GmbH (Ebhausen, Germany) equipment, manoeuvring the torch at a distance of 15 mm from the surface for 180 s, the treatment parameters were set according to literature and the previous experiences reported in Chapter 5 [183,190,223,224].

The Teroson PU9225 adhesive was characterized through bulk tensile test, according to the ASTM D638 – 14, geometry type IV, and by performing DCB and End-Notched Flexure (ENF) tests. The DCB and ENF tests were performed using two different set-up configurations, as shown in Figure 88.

Dimensions	h (mm)	B (mm)	L (mm)	a_0 (mm)	t (mm)
Steel	12.7	25.0	290.0	45.0	0.3
PLA	10.0	20.0	140.0	30.0	0.3
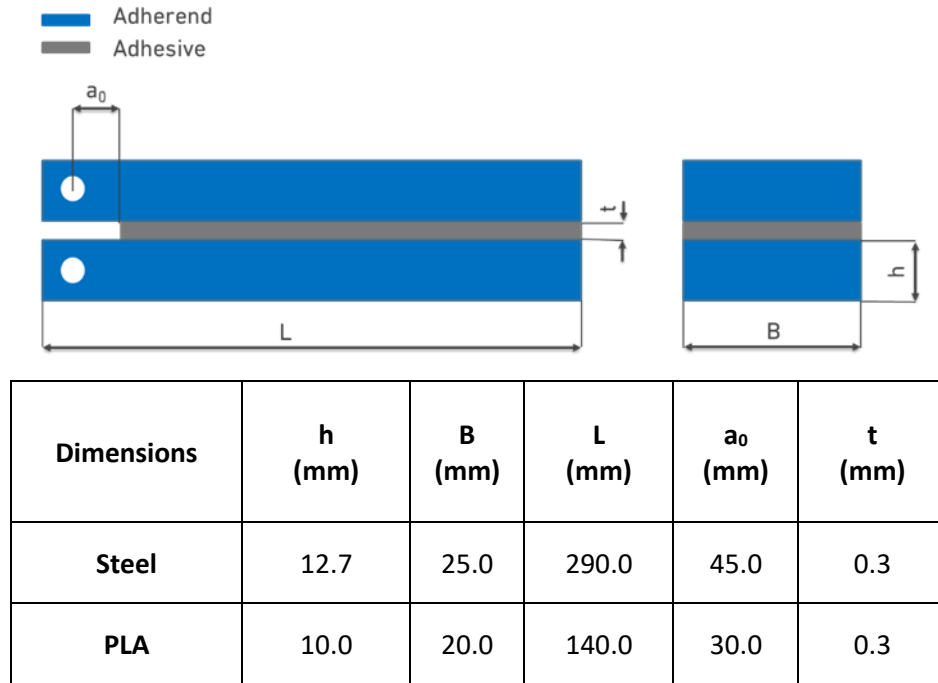
Figure 88: DCB and ENF nominal dimensions for steel and AM PLA specimens [166,181].

The first test configuration uses steel adherends, according to the procedure shown in the work by de Moura et al. [181]. This is a standardized procedure and it was performed to obtain results comparable with the results published in the literature. The second test configuration uses PLA adherends, according to the work described in Chapter 4 for mode I, using cylindrical contact points of radius 5 mm and a span of 100 mm for mode II, in order to produce representative data of the real joint configuration, being to take into account the effect of the AM surface morphology in the case of weak adhesion.

The welding setup design, shown in Figure 89, was based on the works by Hou et al. [225] and Brassard et al. [218].
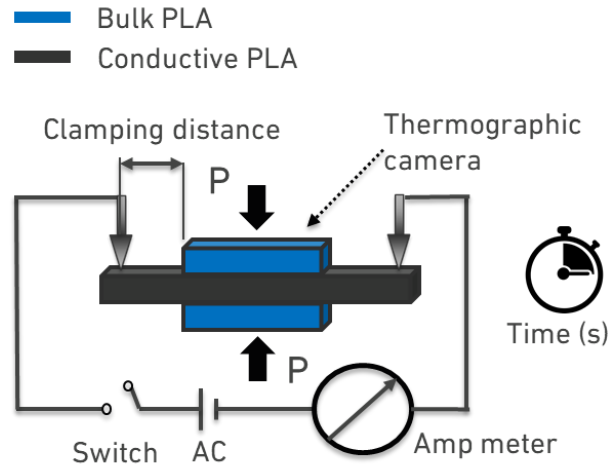
Figure 89: Welding process setup realized according to [218,225].

The welding setup comprises of a non-conductive jig, an AC power supply, able to provide up to 220 V at 50 Hz and controlled using pulse-width modulation (PWM), a thermographic camera Fluke Ti25 Thermal Imager (Fluke Ibérica, S.L., Madrid, Spain) and a system to adjust the clamping distance. It is worth noting that clamping distance is one of the most relevant process parameters, as pointed out in [218]. The thermal cycle was adjusted in order to obtain a temperature range in the 170-250 °C range in the welding area, as recommended in the work of Vanaei et al. [226]. The welding process parameters were chosen with a preliminary characterization: the configuration used for the joints was modified on the upper side, replacing the full size adherend with a single layer adherend. Using this configuration, it was possible to measure a thermal map representative of the studied application. A clamping distance of 1.5 mm was selected, for which the resistance of the conductive plates was assessed to be 1.5±0.4 kΩ between the contact points. The optimum welding parameters were found to correspond to a power density of 440 kW/m^2 and a pressure of 1 MPa applied for a time of 120 s.

6.3 Joints - Bonded, Welded, Hybrid weld-bonded- fabrication, characterization and numerical modelling

In the work reported in this chapter three joint configurations were investigated. These are the bonded, welded and hybrid weld-bonded joints (Figure 90).
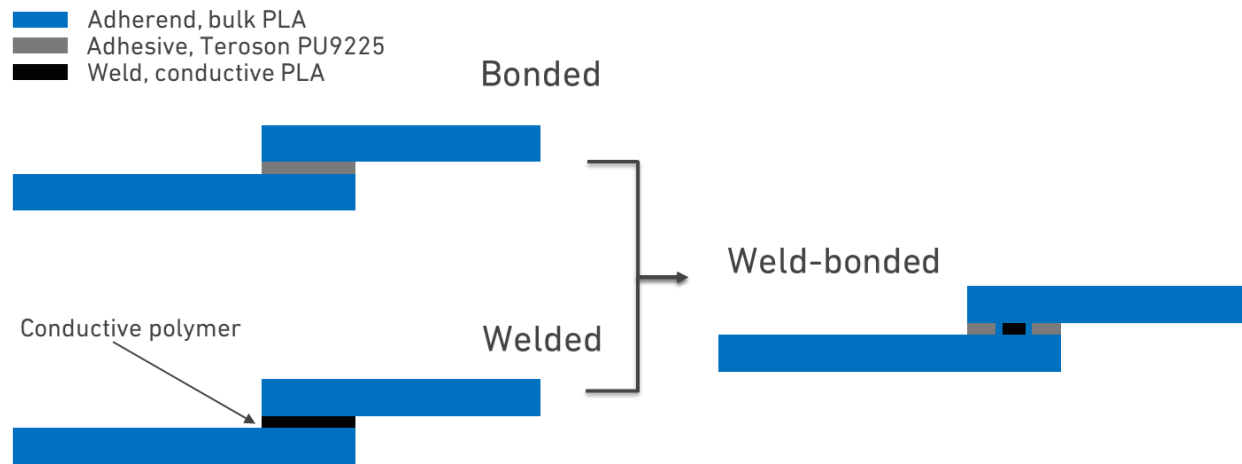
Figure 90: Joints configurations investigated.

To select the adherend thickness and to determine the adhesive percentage of the total overlap in the hybrid solution, a preliminary linear elastic finite element analysis (FEA) was carried out with the Abaqus (Dassault Systèmes Simulia Corp., Johnston, Rhode Island, United States) finite element software. An adherend thickness of 8 mm was selected to guarantee stress levels below the PLA yielding value. The adhesive overlap length in the hybrid solution was selected to improve the joints reproducibility and by observing the trend of the maximum peel and shear stresses, which were found to stabilize in the weld for a total bond length greater than 16 mm. The selected joint geometry is reported in Figure 91 with the same overlap length and bondline thickness being used for all investigated configurations.

Design for Additive Manufacturing and Multi Material Additive Manufacturing applied to joining processes
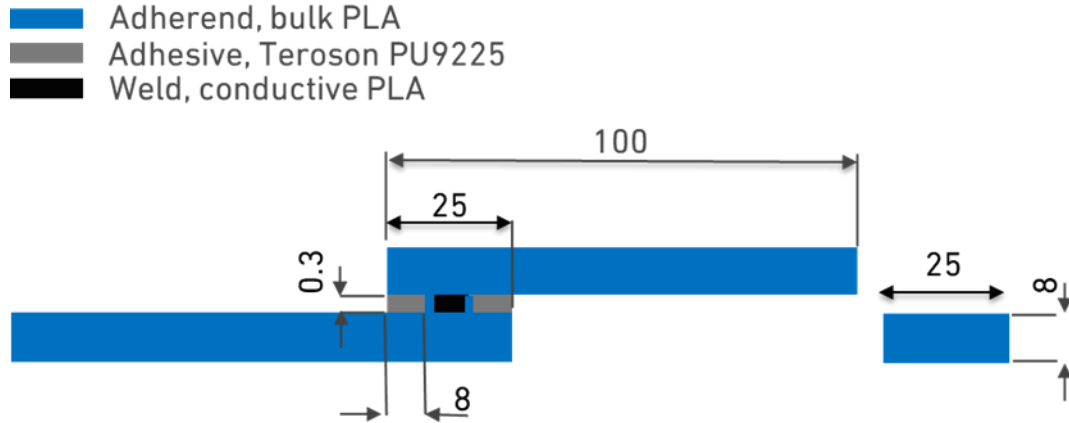
Figure 91: Joints geometry dimensions (expressed in mm).

All mechanical characterization processes were performed using a universal testing machine, the INSTRON® 3367 (Norwood, Massachusetts, USA) equipped with a 30 kN load cell. The tests were carried out under displacement control and at a test speed of 1 mm/min. Load-displacement (P- δ) curves were obtained for each configuration and at least three repetitions were performed for each characterization test.

A FEA was performed using the Abaqus finite element software package for the bonded, welded and weld bonded joint configurations under study (Figure 92).
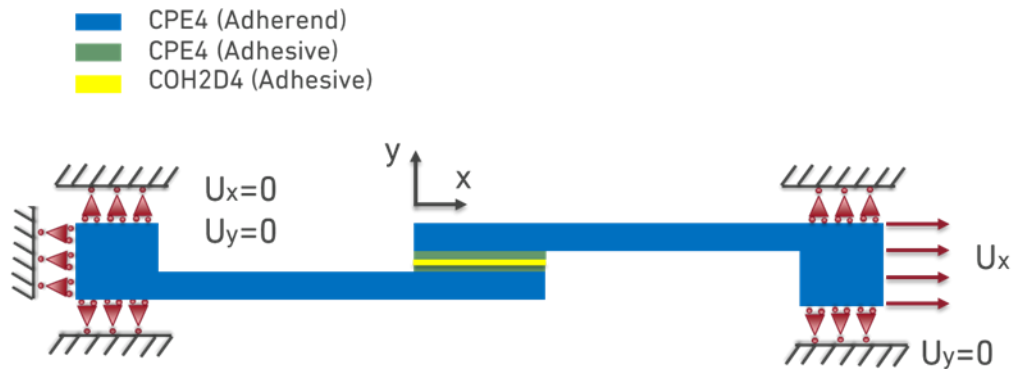
Figure 92: Schematic representation of the numerical model realized in Abaqus.

All the experiments were 2D modelled with plain strain, four node, quadrilateral solid elastic elements (type CPE4) for the adherends and the adhesive or the weld. In the bondline, a cohesive layer of 0.1 mm

was modelled using four node cohesive elements (COH2D4). The layer of cohesive elements is implemented with a triangular cohesive zone model (CZM) law, allowing to accurately model the joint failure process. The dependence of the fracture energy on the mixed mode was modelled using the power law fracture criterion. The mesh size was refined to reduce element size in areas where large stress gradient occur. Each section of the model was assigned with the material properties obtained in the experimental characterization of the materials, described in the previous section.

The results of the mechanical characterization of the PLA materials are reported in Table 31. It is worth noting that the stiffness of the bulk PLA and of the conductive PLA differ by less than 10%, a result consistent to what is reported by Rane et al. [227]. Therefore, it could be possible to tailor the physical properties for the specific application, using the conductive particles as explored in [211,228], without creating significant stiffness gradients in the component that could result in undesirable stress intensity factor effect under service loads.

The unidirectional specimens stress at failure was 26.2±1.5 MPa, this value was used to model the welded material strength in the cohesive law as representative of the intralayer adhesion between the fused filaments.

Table 31: Bulk and conductive PLAs mechanical properties.

		Young's modulus (MPa)	Stress at failure (MPa)	Strain at failure (%)
Bulk PLA	Average	2850.4	56.4	3.4
	Standard deviation	46.8	2.1	0.17
Conductive PLA	average	3110.5	54.5	2.4
	Standard deviation	134.7	4.4	0.18

The PLA surface energy characterization identified an increase of the surface energy from 33.3 mJ/m^2 (as is from 3D printing) to 61.1 mJ/m^2 (after APP treatments). The typical contact angles obtained with water droplets are shown in Figure 93.

(a)   (b)
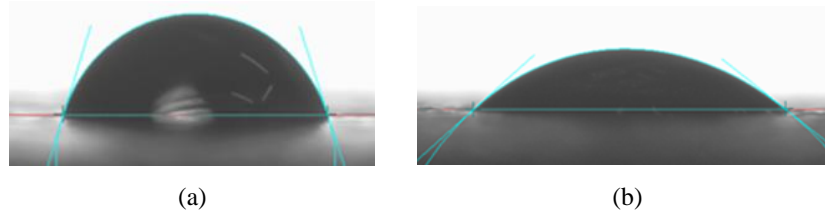
Figure 93: Typical contact angle for wated droplet on AM PLA surface (a) as is from manufacturing, 77º±1º; (b) after 180 s of APP surface treatment, 40º±1º.

The results of the tensile test on the Teroson PU9225 bulk adhesive are reported in Table 32.

Table 32: Tensile mechanical properties of bulk Teroson PU9225 adhesive.

		Young's Modulus (MPa)	Stress at failure (MPa)	Strain at failure (%)
Bulk PU9225	Average	576.9	13.3	13.0
	Standard deviation	16.1	0.3	0.1

The results of the DCB and ENF test, using the Teroson PU9225 adhesive with steel and AM PLA adherends are reported in Table 33.

Table 33: Adhesive and cohesive characterization of the Teroson PU9225 adhesive.

	PLA	STEEL
Fracture toughness mode I	G_{IC} (N/mm)	G_{IC} (N/mm)
Average	0.53	1.39
Standard deviation	0.15	0.04
Fracture toughness mode II	G_{IIC} (N/mm)	G_{IIC} (N/mm)
Average	1.90	7.60
Standard deviation	0.14	0.10
Failure	Mixed	Cohesive

Although cohesive failure was found in the tests carried out with steel adherends, with the PLA adherends weak adhesion was identified, as the failure surfaces showed a mixed failure mechanism, despite the APP surface treatment. As cohesive failure corresponds to the maximum performance achievable in the bondline [17], by comparing the values it can be assumed that the bonded joint performance could be improved by exploring different surface modifications, fully integrated in the AM process, e.g. as described in [107], or performed manually, e.g. chemical etching [223].

6.4 Joints – Bonded, Welded, Hybrid weld-bonded- performance evaluation

A representative load-displacement curve of the adhesively bonded SLJs is reported in Figure 94, average failure load was 2722.7±192.8 N.
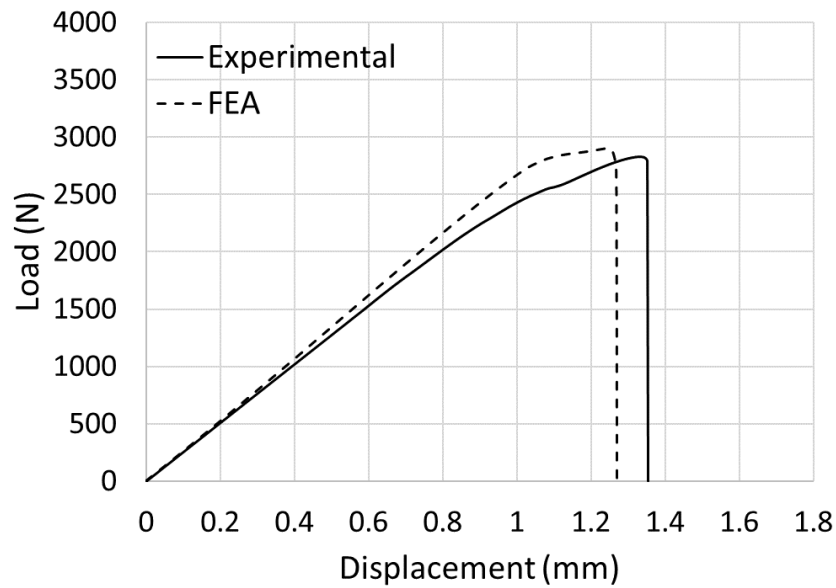
Figure 94: Representative experimental curve and FEA result for the bonded SLJ.

In Figure 95 the failure surface of a bonded SLJ is shown, where a mixed failure mechanism can be clearly observed.
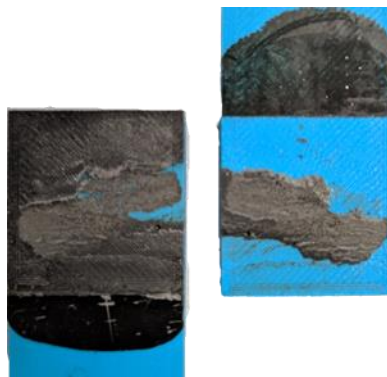
Figure 95: Typical failure surface for adhesively bonded SLJ, nominal bonding area is 25×25 mm^2.

Figure 94 also includes the result from the FEA analysis carried out using the cohesive law parameters obtained with the PLA adherends. A good correlation with the experimental values can be observed.

A representative load-displacement curve of the welded SLJ is reported in Figure 96, average failure load was 3830.3±177.9 N.
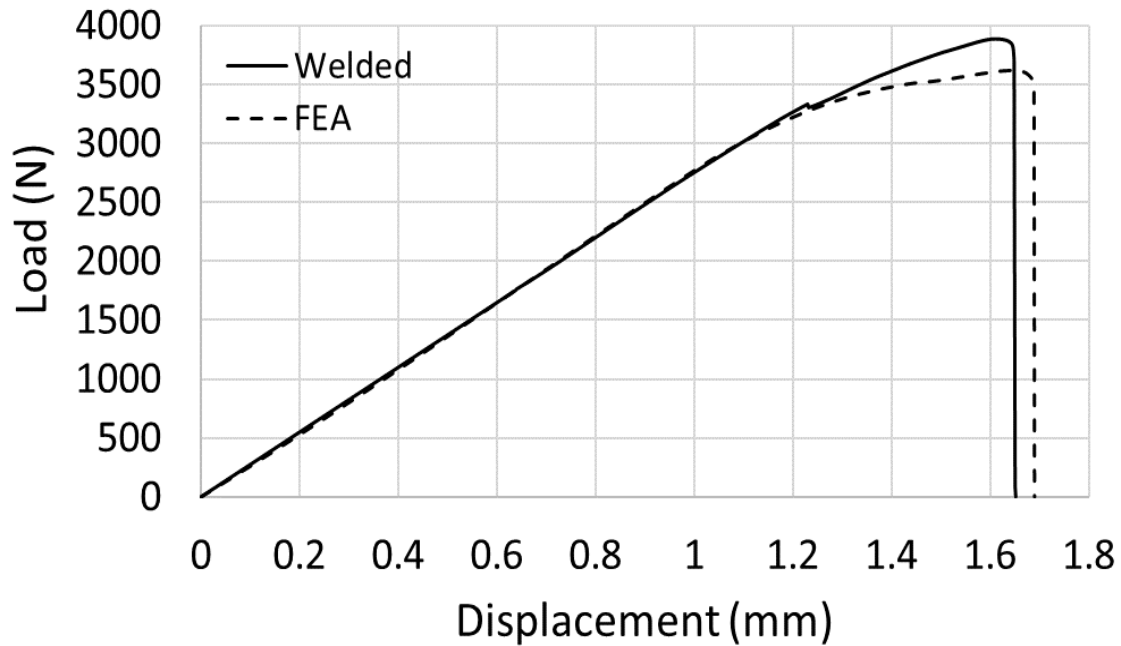
Figure 96: Representative experimental curve and FEA result for the welded SLJ.

In Figure 97 a failure surface for the welded SLJ is shown. It can be seen that failure is cohesive in the weld material.
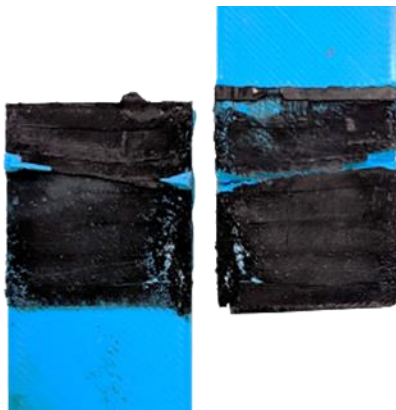
Figure 97: Typical failure surface for welded SLJ, nominal welding area is 25x25 mm.

In Figure 96 the load-displacement curve obtained with the FEA model is also reported. The cohesive law was fitted using the parameters ranges suggested in literature [229,230]. Good correlation was found by setting G_{IC} equal to 0.4 N/mm and G_{IIC} equal to 0.8 N/mm.

A representative load-displacement curve of the weld-bonded SLJ is reported in Figure 98 average failure load was 2777.5±232.9 N.
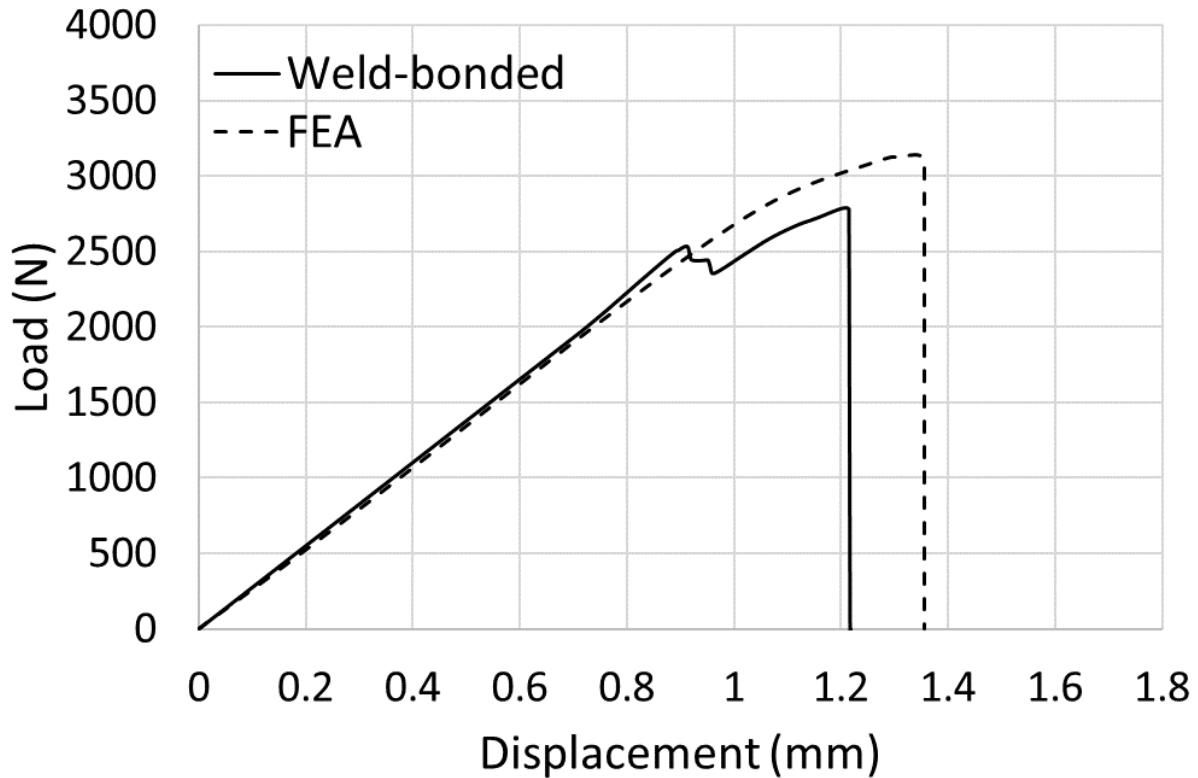
Figure 98: Representative experimental curve and FEA result s for the weld-bonded SLJ.

Observing the failure surface of an hybrid joint, shown in Figure 99, it can be seen as the adhesive is not affected by the different joint configuration, while the weld failure process is slightly different, suggesting that this process output is geometry dependent [218]
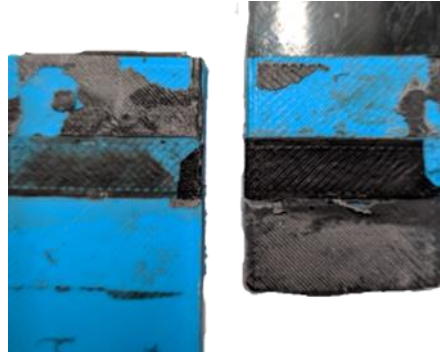
Figure 99: Typical failure surface for weld-bonded SLJ, nominal joining area is 25x25 mm^2.

The FEA model is implemented using the CZM laws validated for the bonded and welded SLJ configurations [231]. It can be observed that the model is able to provide a good agreement with the experimental data in the elastic portion of the curve, while, at failure, load and displacement are both overestimated.

A comparison of the experimental results for all the investigated configurations is shown in Figure 100 superimposing the representative curves
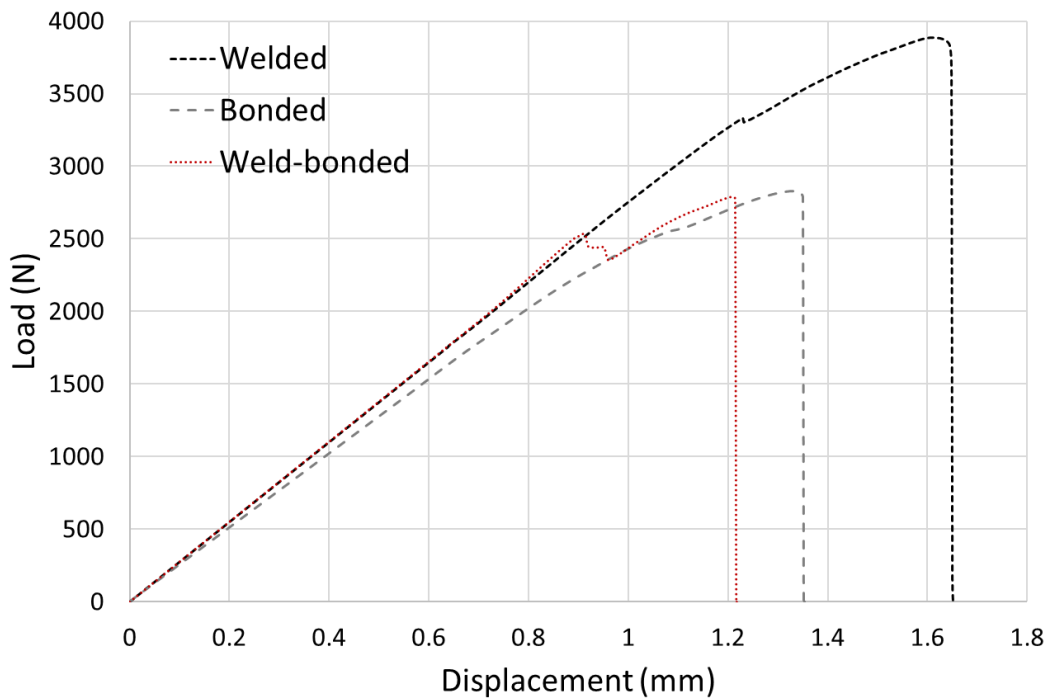
Figure 100: Comparison of the representative experimental curves of the investigated SLJ configurations.

It can be seen that in the explored configurations the welded SLJ has the best performance in terms of load and displacement, while the hybrid weld-bonded configuration has similar performance to the bonded joint in terms of maximum load.

6.5 Discussion and general remarks

In Chapter 6 an experimental study on three different joining solutions for AM materials was carried out, considering bonded, welded and weld-bonded joints. A dedicated set-up for the welding process was designed and a preliminary characterization process was performed to determine the process parameters that lead to cohesive failure of the joint. The effectiveness of the APP surface treatment, performed according to the results of Chapter 5, was assessed through surface energy measurement and this technique was used to improve the adhesion in bonded and weld-bonded joints. SLJs were mechanically tested for each joining solution and corresponding numerical models were developed in order to better understand the performance of each configuration under study.

Adhesive bonding of AM processed components is a challenging process due to the low surface energy of thermoplastic polymers and the peculiar morphology imprinted by the material deposition pattern. Thus, 3D printing parameters and component placement should be considered as major joint design factors, as assessed in Chapter 4. For the materials used in this work, weak adhesion was encountered even after APP surface treatment. This indicates that alternative surface treatment solutions, e.g. chemical etching, should be explored to enable structural applications of this joining process.

The technical feasibility of the hybrid weld-bonded joint using AM with a conductive thermoplastic polymer was assessed and a corresponding numerical model was created. This model was able to show good correlation with the experimental results. The investigated configuration, both in terms of materials and geometry, did not lead to a performance improvement. This was mainly a result of the low level of adhesion between the adhesive and the AM substrates. Hybrid weld-bonded joints and bonded joints with stiffness tailored bondline solutions were proven to be effective after geometry optimization and especially under dynamic loading conditions. The obtained results suggest that this joining solution, with further optimizations to the adhesion level, will be relevant for industrial applications for component manufactured with AM and composed of long fibre reinforced thermoplastic matrices.

The welding joining process was found to be a highly promising joining process for the assembly of AM components. No surface modification was required for the proposed configuration and, taking advantage of multi material AM process capability for direct printing of integrated circuits, it is entirely possible to design components ready to be assembled and with an optimized geometry of the welding area. It is worth noting that integrating welding setup in the component would ease the welding process, overcoming critical aspects such as the need for a fine control over the clamping distance. Theoretically, any polymer can be used with conductive particles and multi material AM can be used to create joints

Design for Additive Manufacturing and Multi Material Additive Manufacturing applied to joining processes

with tailored stiffness, achieved by varying the volumetric percentage of the reinforcements and the matrix polymers.

Finally, the results of this chapter suggest that locally controlled joule heating using AM with a conductive thermoplastic filament could be expanded to other joint designs, such as locally cured adhesives (using conductive pads at adherend-adhesive interface), or self-healing (placing conductive pads in critical area were delamination and damage could occur). Moreover this technique enables also the possibility to use localized heating for disassembly.

These features can all be implemented with the inclusion of dedicated embedded circuits in the bulk material, able to perform localized welding through the thickness.

Conclusions

Thesis conclusions

The presented work focused on providing an incipit to the development of a design method for AM joints. Ideally this methodology will combine the design for additive manufacturing to the current knowledge, at time of writing, on improving the joints performance, i.e. joint tailoring. This work begun (Chapter 1) with the testing methods for determination of the mechanical properties of the AM processed materials. Aim was to produce comparable data and to take advantage of the anisotropy caused by the AM processes, taking in account its effect on the AM adherends and, in general, on components durability.

At the same time, a review of tailoring methods proposed in research articles by several authors was performed (Chapter 2); the purpose was to provide an organized summary and to set a starting point for the development of a design method. Then, with a design benchmark, i.e. performing the redesign for AM of a robotic end effector (Chapter 3), it was possible to find out current challenges and the new design opportunities AM-enabled for components manufacturing. Consequently, different research lines were set according to different tailoring approaches: surface modifications and locally controlled material properties. Surface modifications were embedded in the AM process using dedicated combinations of printing parameters (Chapter 4) or performed through industrial methods, e.g. plasma treatment, (Chapter 5). Then feasibility of joints tailoring, i.e. hybrid joints, using multi-material AM was assessed (Chapter 6).

As a general remark, optimized performances of the 3D printed components can be achieved by including the AM process and its parameters into the design variables.

Moreover, while the effects of the print parameters are usually 3D printer specific and their characterization requires experimental testing, the effects of the AM process can be taken into account using the AM material models proposed in literature, e.g. for FFF by Croccolo et al. [232] and Casavola et al. [77].

A list of the main conclusions drawn from this work in terms of each task investigated is therefore presented.

Task 1 - Determination of mechanical properties of materials correlated to the 3D printing set-ups:

- **Quasi static testing:**
  - AM process confers to the materials anisotropic properties.
  - The anisotropy grade in AM materials depends on the printing setup and the material chemistry.
  - Sizing of AM components can be performed with methods originally designed for composite, with proper adaptation.
  - NIST organization provided a summary of standards on material testing that can be applied to characterize AM materials; however, dedicated modifications could be necessary.

- **Bonded joints Testing:**
  - At the time of writing dedicated standards for AM joints characterization do not exist.
  - A summary of testing methods proposed in the scientific literature, adapted for the scope and then validated, was produced.

- **Fatigue testing:**
  - Miniaturized AM specimens can be effectively used for plane-bending fatigue testing
  - Placement strongly affect the fatigue life of AM components.
  - Printing parameters, in particular deposition speed, are relevant for fatigue life and, in general, play a role in the detected defects.
  - AM morphology increases the scatter in fatigue results.

Task 2 - Study on design for additive manufacturing applied to adhesive bonding:

- **Adherends – through the thickness tailoring:**
  - Sub-surface structures are a promising approach because they are able to produce an optimized stress distribution without the necessity to modify the coupling surfaces.
  - Using sub-surface structures, it is possible to obtain enhanced energy absorption.
  - By optimizing the multi-material stacking it is possible to reduce peak stresses at overlap ends.

- **Adhesive tailoring:**
  - Using multi-material approach to deposit the adhesives, it is possible to ease the manufacturing of mixed-adhesive joints.
  - Using AM to deposit the adhesives it is possible to obtain namely flawless bond-line.

- **Surface tailoring:**
  - AM complexity-for-free enable to add surface features, e.g. structured patterns, to improve the joints performance.

Task 3 - Case of study, re-design for additive manufacturing of a robotic gripper:

- **DfAM:**
  - AM enables the embedding of the functionality in the shapes, therefore it is possible to achieve a dramatic reduction on parts and components.
  - AM materials anisotropy has to be taken into account for components sizing.
  - AM materials anisotropy can be used to achieve new design solutions for components optimization.

- **Adhesive bonding:**
  - Adhesive bonding, due to its improved stress distribution compared to fastening, allow to use components with extremely optimized design.
  - Thermoplastic materials typically used to manufacture AM components are difficult to be bonded.
  - Surface modifications have to be evaluated according to the specific application.

Task 4 - Appraisal of surface preparation in adhesive bonding of additive manufactured substrates:

- For wettability assessment static and dynamic contact angle measurements are needed due to the AM-generated roughness.
- Different plasma treatments have different output on joints performance also due to peculiar effects on the AM-generated morphology.
- Concerning industrial surface modifications, low pressure plasma is the most effective one.

Task 5 - 3D printing parameters as bonded joint design factors:

- It is possible to affect mechanical properties through the printing parameters.
- It is possible to optimize morphology and wettability using dedicated printing parameters.
- AM-adherends dedicated testing procedure for fracture toughness was proposed.
- AM surface roughness patterns can be used to manufacture ready-to-be-bonded components.

Task 6 - Weld-bonded joints using conductive thermoplastic filaments:

- Adhesive bonding of AM processed components is a challenging process.
- Multi-material AM with conductive filaments enabled the manufacturing of embedded through-the-thickness electrical circuits. These circuits can be used for structure monitoring, self-healing and disassembly.
- AM-controlled welding is a promising joining process that overcome the main drawbacks of welding using joule-heating.
- Hybrid weld-bonded joints are technically feasible but needs geometrical and materials optimizations.

Finally, even if a defined methodology for the design for additive manufacturing applied to joining processes does not currently exist at the time of writing, an effort towards that direction was made.

References

1.   Zolfagharian, A.; Kaynak, A.; Kouzani, A. Closed-loop 4D-printed soft robots. *Mater. Des.* **2020**, *188*, 108411, doi:10.1016/j.matdes.2019.108411.

2.   Zwick-Roell Zwick-Roell 3D printed robotic end effector for material testing Available online: https://www.zwickroell.com/en/automated-testing-systems/robotest-n-smart-light-weight-robot.

3.   Fantini, M.; De Crescenzio, F.; Brognara, L.; Baldini, N. Design and Rapid Manufacturing of a customized foot orthosis: a first methodological study. In; 2017; pp. 457–467.

4.   Fernandez-Vicente, M.; Escario Chust, A.; Conejero, A. Low cost digital fabrication approach for thumb orthoses. *Rapid Prototyp. J.* **2017**, *23*, 1020–1031, doi:10.1108/RPJ-12-2015-0187.

5.   Avalle, M.; Belotti, V.; Frascio, M.; Razzoli, R. Development of a wearable device for the early diagnosis of neurodegenerative diseases. *IOP Conf. Ser. Mater. Sci. Eng.* **2020**.

6.   Machado, J.J.M.; Gamarra, P.M.R.; Marques, E.A.S.; da Silva, L.F.M. Improvement in impact strength of composite joints for the automotive industry. *Compos. Part B Eng.* **2018**, *138*, 243–255, doi:10.1016/j.compositesb.2017.11.038.

7.   Gupta, C.; MB, P.; Shet, N.K.; Ghosh, A.K.; Bandyopadhyay, S.; Mukhopadhyay, P. Microstructure and mechanical performance examination of 3D printed acrylonitrile butadiene styrene thermoplastic parts. *Polym. Eng. Sci.* **2020**, *60*, 2770–2781, doi:10.1002/pen.25507.

8.   Razavykia, A.; Brusa, E.; Delprete, C.; Yavari, R. An Overview of Additive Manufacturing Technologies—A Review to Technical Synthesis in Numerical Study of Selective Laser Melting. *Materials (Basel).* **2020**, *13*, doi:10.3390/ma13173895.

9.   Haleem, A.; Javaid, M. Additive Manufacturing Applications in Industry 4.0: A Review. *J. Ind. Integr. Manag.* **2019**, *04*, 1930001, doi:10.1142/S2424862219300011.

10.   Difonzo, E.; Zappatore, G.; Mantriota, G.; Reina, G. Advances in Finger and Partial Hand Prosthetic Mechanisms. *Robotics* **2020**, *9*, 80, doi:10.3390/robotics9040080.

11.   Ramola, M.; Yadav, V.; Jain, R. On the adoption of additive manufacturing in healthcare: a literature review. *J. Manuf. Technol. Manag.* **2019**, *30*, 48–69, doi:10.1108/JMTM-03-2018-0094.

12.   Kumar, L.J.; Krishnadas Nair, C.G. Current Trends of Additive Manufacturing in the Aerospace Industry. In *Advances in 3D Printing & Additive Manufacturing Technologies*; Springer Singapore: Singapore, 2017; pp. 39–54.

13.   Huang, R.; Riddle, M.; Graziano, D.; Warren, J.; Das, S.; Nimbalkar, S.; Cresko, J.; Masanet, E. Energy and emissions saving potential of additive manufacturing: the case of lightweight aircraft

167

components. *J. Clean. Prod.* **2016**, *135*, 1559–1570, doi:10.1016/j.jclepro.2015.04.109.

14.   Yuan, S.; Shen, F.; Chua, C.K.; Zhou, K. Polymeric composites for powder-based additive manufacturing: Materials and applications. *Prog. Polym. Sci.* **2019**, *91*, 141–168, doi:10.1016/j.progpolymsci.2018.11.001.

15.   Friedrich, K.; Almajid, A.A. Manufacturing Aspects of Advanced Polymer Composites for Automotive Applications. *Appl. Compos. Mater.* **2013**, *20*, 107–128, doi:10.1007/s10443-012-9258-7.

16.   Petrie, E.M. *Handbook of Adhesives and Sealants*; 1996; Vol. 25; ISBN 9780071709811.

17.   *Handbook of Adhesion Technology*; da Silva, L.F.M., Öchsner, A., Adams, R.D., Eds.; Springer International Publishing: Cham, 2018; ISBN 978-3-319-55410-5.

18.   Song, P.; Fu, Z.; Liu, L.; Fu, C.-W. Printing 3D objects with interlocking parts. *Comput. Aided Geom. Des.* **2015**, *35–36*, 137–148, doi:10.1016/j.cagd.2015.03.020.

19.   Gibson, I.; Rosen, D.; Stucker, B. *Additive Manufacturing Technologies*; Springer New York: New York, NY, 2015; ISBN 978-1-4939-2112-6.

20.   Ali, M.H.; Batai, S.; Sarbassov, D. 3D printing: a critical review of current development and future prospects. *Rapid Prototyp. J.* **2019**, *25*, 1108–1126, doi:10.1108/RPJ-11-2018-0293.

21.   Spaggiari, A.; Denti, F. Mechanical strength of adhesively bonded joints using polymeric additive manufacturing. *Proc. Inst. Mech. Eng. Part C J. Mech. Eng. Sci.* **2019**, *0*, 1–9, doi:10.1177/0954406219850221.

22.   Garcia, R.; Prabhakar, P. Bond interface design for single lap joints using polymeric additive manufacturing. *Compos. Struct.* **2017**, *176*, 547–555, doi:10.1016/j.compstruct.2017.05.060.

23.   Bürenhaus, F.; Moritzer, E.; Hirsch, A. Adhesive bonding of FDM-manufactured parts made of ULTEM 9085 considering surface treatment, surface structure, and joint design. *Weld. World* **2019**, *63*, 1819–1832, doi:10.1007/s40194-019-00810-4.

24.   Cavalcanti, D.K.K.; Banea, M.D.; de Queiroz, H.F.M. Mechanical characterization of bonded joints made of additive manufactured adherends. *Ann. "Dunarea Jos" Univ. Galati, Fascicle XII, Weld. Equip. Technol.* **2019**, *30*, 27–33, doi:10.35219/awet.2019.04.

25.   Li, W.; Sang, L.; Jian, X.; Wang, J. Influence of sanding and plasma treatment on shear bond strength of 3D-printed PEI, PEEK and PEEK/CF. *Int. J. Adhes. Adhes.* **2020**, *100*, 102614, doi:10.1016/j.ijadhadh.2020.102614.

26.   Kovan, V.; Altan, G.; Topal, E.S.; Camurlu, H.E. Surface roughness effect on the 3D printed butt

joints strength. *Dedic. to 50th Anniv. Year Tribol. - Proc. 8th Int. Sci. Conf. BALTTRIB 2015* **2016**, 117–121, doi:10.15544/balttrib.2015.21.

27.   Kovan, V.; Altan, G.; Topal, E.S. Effect of layer thickness and print orientation on strength of 3D printed and adhesively bonded single lap joints. *J. Mech. Sci. Technol.* **2017**, *31*, 2197–2201, doi:10.1007/s12206-017-0415-7.

28.   Kariz, M.; Kuzman, M.K.; Sernek, M. Adhesive bonding of 3D-printed ABS parts and wood. *J. Adhes. Sci. Technol.* **2017**, *31*, 1683–1690, doi:10.1080/01694243.2016.1268414.

29.   Dugbenoo, E.; Arif, M.F.; Wardle, B.L.; Kumar, S. Enhanced Bonding via Additive Manufacturing-Enabled Surface Tailoring of 3D Printed Continuous-Fiber Composites. *Adv. Eng. Mater.* **2018**, *20*, 1800691, doi:10.1002/adem.201800691.

30.   García-Guzmán, L.; Távara, L.; Reinoso, J.; Justo, J.; París, F. Fracture resistance of 3D printed adhesively bonded DCB composite specimens using structured interfaces: Experimental and theoretical study. *Compos. Struct.* **2018**, *188*, 173–184, doi:10.1016/j.compstruct.2017.12.055.

31.   Yap, Y.L.; Toh, W.; Koneru, R.; Lin, R.; Chan, K.I.; Guang, H.; Chan, W.Y.B.; Teong, S.S.; Zheng, G.; Ng, T.Y. Evaluation of structural epoxy and cyanoacrylate adhesives on jointed 3D printed polymeric materials. *Int. J. Adhes. Adhes.* **2020**, *100*, 102602, doi:10.1016/j.ijadhadh.2020.102602.

32.   Schmidt, K.; Zimmermann, A. Evaluation of process and anisotropy of thermosetting adhesives with ultraviolet-assisted 3D dispensing. *Addit. Manuf.* **2020**, *34*, 101262, doi:10.1016/j.addma.2020.101262.

33.   Sekiguchi, Y.; Nakanouchi, M.; Haraga, K.; Takasaki, I.; Sato, C. Experimental investigation on strength of stepwise tailored single lap adhesive joint using second-generation acrylic adhesive via shear and low-cycle shear tests. *Int. J. Adhes. Adhes.* **2019**, *95*, 102438, doi:10.1016/j.ijadhadh.2019.102438.

34.   Morano, C.; Bruno, L.; Pagnotta, L.; Alfano, M. Analysis of crack trapping in 3D printed bio-inspired structural interfaces. *Procedia Struct. Integr.* **2018**, *12*, 561–566, doi:10.1016/j.prostr.2018.11.063.

35.   Morano, C.; Zavattieri, P.; Alfano, M. Tuning energy dissipation in damage tolerant bio-inspired interfaces. *J. Mech. Phys. Solids* **2020**, *141*, 103965, doi:10.1016/j.jmps.2020.103965.

36.   Alfano, M.; Morano, C.; Bruno, L.; Muzzupappa, M.; Pagnotta, L. Analysis of debonding in bio-inspired interfaces obtained by additive manufacturing. *Procedia Struct. Integr.* **2018**, *8*, 604–609, doi:10.1016/j.prostr.2017.12.059.

37.   Leicht, H.; Orf, L.; Hesselbach, J.; Vudugula, H.; Kraus, E.; Baudrit, B.; Hochrein, T.; Bastian, M.

169

Adhesive bonding of 3D-printed plastic components. *J. Adhes.* **2020**, *96*, 48–63, doi:10.1080/00218464.2019.1682561.

38. Fieger, T.; Nugara, D.; Huebner, J.; Witt, G. Optimization of adhesively joined laser-sintered parts. *Solid Free. Fabr. 2017 Proc. 28th Annu. Int. Solid Free. Fabr. Symp. - An Addit. Manuf. Conf. SFF 2017* **2017**, 567–577.

39. Arumaikkannu, G.; Vijayanand, R.; Sugavaneswaran, M. Experimental investigation on fracture resistance behavior of additive manufactured multimaterial structure with corrugated interface. *Proc. 2nd Int. Conf. Prog. Addit. Manuf. (Pro-AM 2016)* **2016**, *1*, 252–257.

40. Kumar, S.; Wardle, B.L.; Arif, M.F. Strength and performance enhancement of bonded joints by spatial tailoring of adhesive compliance via 3D printing. *ACS Appl. Mater. Interfaces* **2017**, *9*, 884–891, doi:10.1021/acsami.6b13038.

41. Kumar, S.; Wardle, B.L.; Arif, M.F.; Ubaid, J. Stress Reduction of 3D Printed Compliance-Tailored Multilayers. *Adv. Eng. Mater.* **2018**, *20*, 1–8, doi:10.1002/adem.201700883.

42. Khan, M.A.; Kumar, S.; Cantwell, W.J. Additively manufactured cylindrical systems with stiffness-tailored interface: Modeling and experiments. *Int. J. Solids Struct.* **2018**, *152–153*, 71–84, doi:10.1016/j.ijsolstr.2018.06.002.

43. Khan, M.A.; Kumar, S. Performance enhancement of tubular multilayers via compliance-tailoring: 3D printing, testing and modeling. *Int. J. Mech. Sci.* **2018**, *140*, 93–108, doi:10.1016/j.ijmecsci.2018.02.038.

44. Ubaid, J.; Wardle, B.L.; Kumar, S. Strength and Performance Enhancement of Multilayers by Spatial Tailoring of Adherend Compliance and Morphology via Multimaterial Jetting Additive Manufacturing. *Sci. Rep.* **2018**, *8*, 1–10, doi:10.1038/s41598-018-31819-2.

45. Udroiu, R.; Braga, I.; Nedelcu, A. Evaluating the Quality Surface Performance of Additive Manufacturing Systems: Methodology and a Material Jetting Case Study. *Materials (Basel).* **2019**, *12*, 995, doi:10.3390/ma12060995.

46. Ituarte, I.F.; Boddeti, N.; Hassani, V.; Dunn, M.L.; Rosen, D.W. Design and additive manufacture of functionally graded structures based on digital materials. *Addit. Manuf.* **2019**, *30*, 100839, doi:10.1016/j.addma.2019.100839.

47. Redmann, A.J.; Setter, R.N.; Dahmen, V.; Austermann, J.; Quintanilla, A.L.; Mecham, S.J.; Osswald, T.A. Additively manufactured B-stage epoxy for adhesive bonding in composite structures. In Proceedings of the CAMX 2018 - Composites and Advanced Materials Expo; 2018.

170

48. Dahmen, V.; Redmann, A.J.; Austermann, J.; Quintanilla, A.L.; Mecham, S.J.; Osswald, T.A. Fabrication of hybrid composite T-joints by co-curing with 3D printed dual cure epoxy. *Compos. Part B Eng.* **2020**, *183*, 107728, doi:10.1016/j.compositesb.2019.107728.

49. Urhal, P.; Weightman, A.; Diver, C.; Bartolo, P. Robot assisted additive manufacturing: A review. *Robot. Comput. Integr. Manuf.* **2019**, *59*, 335–345, doi:10.1016/j.rcim.2019.05.005.

50. Etienne, J.; Ray, N.; Panozzo, D.; Hornus, S.; Wang, C.C.L.; Martínez, J.; McMains, S.; Alexa, M.; Wyvill, B.; Lefebvre, S. CurviSlicer. *ACM Trans. Graph.* **2019**, *38*, 1–11, doi:10.1145/3306346.3323022.

51. Packham, D.E. Theories of fundamental adhesion. In *Handbook of Adhesion Technology: Second Edition*; 2018; Vol. 1–2, pp. 11–41 ISBN 9783319554112.

52. Frascio, M.; Avalle, M.; Monti, M. Fatigue strength of plastics components made in additive manufacturing: First experimental results. *Procedia Struct. Integr.* **2018**, *12*, 32–43, doi:10.1016/j.prostr.2018.11.109.

53. Shanmugam, V.; Das, O.; Babu, K.; Marimuthu, U.; Veerasimman, A.; Johnson, D.J.; Neisiany, R.E.; Hedenqvist, M.S.; Ramakrishna, S.; Berto, F. Fatigue behaviour of FDM-3D printed polymers, polymeric composites and architected cellular materials. *Int. J. Fatigue* **2021**, *143*, 106007, doi:10.1016/j.ijfatigue.2020.106007.

54. Primo, T.; Calabrese, M.; Del Prete, A.; Anglani, A. Additive manufacturing integration with topology optimization methodology for innovative product design. *Int. J. Adv. Manuf. Technol.* **2017**, *93*, 467–479, doi:10.1007/s00170-017-0112-9.

55. Dizon, J.R.C.; Espera, A.H.; Chen, Q.; Advincula, R.C. Mechanical characterization of 3D-printed polymers. *Addit. Manuf.* **2018**, *20*, 44–67, doi:10.1016/j.addma.2017.12.002.

56. Harris, M.; Potgieter, J.; Archer, R.; Arif, K.M. Effect of material and process specific factors on the strength of printed parts in fused filament fabrication: A review of recent developments. *Materials (Basel).* **2019**, *12*, doi:10.3390/ma12101664.

57. Baca, D.; Ahmad, R. The impact on the mechanical properties of multi-material polymers fabricated with a single mixing nozzle and multi-nozzle systems via fused deposition modeling. *Int. J. Adv. Manuf. Technol.* **2020**, *106*, 4509–4520, doi:10.1007/s00170-020-04937-3.

58. Stoia, D.I.; Marsavina, L.; Linul, E. Correlations between process parameters and outcome properties of laser-sintered polyamide. *Polymers (Basel).* **2019**, *11*, doi:10.3390/polym11111850.

59. García Galicia, J.A.; Benes, B. Improving printing orientation for Fused Deposition Modeling

171

printers by analyzing connected components. *Addit. Manuf.* **2018**, *22*, 720–728, doi:10.1016/j.addma.2018.06.007.

60.   Slotwinski, J.; Cooke, A.; Moylan, S. Mechanical properties testing for metal parts made via additive manufacturing: A review of the state of the art of mechanical property testing. *Addit. Manuf. Mater. Stand. Test. Appl.* **2015**, 1–20.

61.   Ning, H.; Lu, N.; Hassen, A.A.; Chawla, K.; Selim, M.; Pillay, S. A review of Long fibre thermoplastic (LFT) composites. *Int. Mater. Rev.* **2020**, *65*, 164–188, doi:10.1080/09506608.2019.1585004.

62.   Chacón, J.M.; Caminero, M.A.; Núñez, P.J.; García-Plaza, E.; García-Moreno, I.; Reverte, J.M. Additive manufacturing of continuous fibre reinforced thermoplastic composites using fused deposition modelling: Effect of process parameters on mechanical properties. *Compos. Sci. Technol.* **2019**, *181*, 107688, doi:10.1016/j.compscitech.2019.107688.

63.   Forster, A.M. Materials testing standards for additive manufacturing of polymer materials: State of the art and standards applicability. *Addit. Manuf. Mater. Stand. Test. Appl.* **2015**, 67–123.

64.   Yang, L.; Harrysson, O.; West, H.; Cormier, D. Mechanical properties of 3D re-entrant honeycomb auxetic structures realized via additive manufacturing. *Int. J. Solids Struct.* **2015**, *69–70*, 475–490, doi:https://doi.org/10.1016/j.ijsolstr.2015.05.005.

65.   Wang, B.; Sun, L.; Pan, B. Mapping internal deformation fields in 3D printed porous structure with digital volume correlation. *Polym. Test.* **2019**, *78*, 105945, doi:10.1016/j.polymertesting.2019.105945.

66.   Andrew, J.J.; Ubaid, J.; Hafeez, F.; Schiffer, A.; Kumar, S. Impact performance enhancement of honeycombs through additive manufacturing-enabled geometrical tailoring. *Int. J. Impact Eng.* **2019**, *134*, 103360, doi:10.1016/j.ijimpeng.2019.103360.

67.   Li, L.; Sun, Q.; Bellehumeur, C.; Gu, P. Composite modeling and analysis for fabrication of FDM prototypes with locally controlled properties. *J. Manuf. Process.* **2002**, *4*, 129–141, doi:10.1016/S1526-6125(02)70139-4.

68.   Ravoori, D.; Alba, L.; Prajapati, H.; Jain, A. Investigation of process-structure-property relationships in polymer extrusion based additive manufacturing through in situ high speed imaging and thermal conductivity measurements. *Addit. Manuf.* **2018**, *23*, 132–139, doi:10.1016/j.addma.2018.07.011.

69.   Allum, J.; Gleadall, A.; Silberschmidt, V. V. Fracture of 3D-printed polymers: Crucial role of filament-scale geometric features. *Eng. Fract. Mech.* **2020**, *224*, 106818, doi:10.1016/j.engfracmech.2019.106818.

172

References

70.   Kumar Mishra, P.; P, S. Prediction of in-plane stiffness of multi-material 3D printed laminate parts fabricated by FDM process using CLT and its mechanical behaviour under tensile load. *Mater. Today Commun.* **2020**, *23*, 100955, doi:10.1016/j.mtcomm.2020.100955.

71.   Liao, Y.; Liu, C.; Coppola, B.; Barra, G.; Di Maio, L.; Incarnato, L.; Lafdi, K. Effect of porosity and crystallinity on 3D printed PLA properties. *Polymers (Basel).* **2019**, *11*, 1–14, doi:10.3390/polym11091487.

72.   Cantrell, J.; Rohde, S.; Damiani, D.; Gurnani, R.; Di Sandro, L.; Anton, J.; Young, A.; Jerez, A.; Steinbach, D.; Kroese, C.; et al. Experimental characterization of the mechanical properties of 3D printed ABS and polycarbonate parts. *Conf. Proc. Soc. Exp. Mech. Ser.* **2017**, *3*, 89–105, doi:10.1007/978-3-319-41600-7_11.

73.   Fernandez-Vicente, M.; Calle, W.; Ferrandiz, S.; Conejero, A. Effect of Infill Parameters on Tensile Mechanical Behavior in Desktop 3D Printing. *3D Print. Addit. Manuf.* **2016**, *3*, 183–192, doi:10.1089/3dp.2015.0036.

74.   Corbett, T.; Kok, T.; Lee, C.; Smith, S.; Villarraga, H.; Tarbutton, J. Identification of Mechanical and Fatigue Characteristics of Polymers Fabricated by additive Manufacturing Process. *SPRING Top. Meet.* **2014**, *57*.

75.   Abbott, A.C.; Tandon, G.P.; Bradford, R.L.; Koerner, H.; Baur, J.W. Process-structure-property effects on ABS bond strength in fused filament fabrication. *Addit. Manuf.* **2018**, *19*, 29–38, doi:10.1016/j.addma.2017.11.002.

76.   S., S.; R.M., T.; H., A. Numerical investigation of stiffness properties ofFDM parts as a function of raster orientation. *Proc. ofthe 28th Annu. Int. Solid Free. Fabr. Symp.* **2017**.

77.   Casavola, C.; Cazzato, A.; Moramarco, V.; Pappalettere, C. Orthotropic mechanical properties of fused deposition modelling parts described by classical laminate theory. *Mater. Des.* **2016**, *90*, 453–458, doi:10.1016/j.matdes.2015.11.009.

78.   Lopes, L.R.; Silva, A.F.; Carneiro, O.S. Multi-material 3D printing: The relevance of materials affinity on the boundary interface performance. *Addit. Manuf.* **2018**, *23*, 45–52, doi:10.1016/j.addma.2018.06.027.

79.   Lumpe, T.S.; Mueller, J.; Shea, K. Tensile properties of multi-material interfaces in 3D printed parts. *Mater. Des.* **2019**, *162*, 1–9, doi:10.1016/j.matdes.2018.11.024.

80.   Yin, J.; Lu, C.; Fu, J.; Huang, Y.; Zheng, Y. Interfacial bonding during multi-material fused deposition modeling (FDM) process due to inter-molecular diffusion. *Mater. Des.* **2018**, *150*, 104–112,

References

doi:10.1016/j.matdes.2018.04.029.

81. Watschke, H.; Waalkes, L.; Schumacher, C.; Vietor, T. Development of novel test specimens for characterization of multi-material parts manufactured by material extrusion. *Appl. Sci.* **2018**, *8*, doi:10.3390/app8081220.

82. Tamburrino, F.; Graziosi, S.; Bordegoni, M. The influence of slicing parameters on the multi-material adhesion mechanisms of FDM printed parts: an exploratory study. *Virtual Phys. Prototyp.* **2019**, *14*, 316–332, doi:10.1080/17452759.2019.1607758.

83. Rafiee, M.; Farahani, R.D.; Therriault, D. Multi-Material 3D and 4D Printing : A Survey. **2020**, *1902307*, 1–26, doi:10.1002/advs.201902307.

84. Stano, G.; Di Nisio, A.; Lanzolla, A.; Percoco, G. Additive manufacturing and characterization of a load cell with embedded strain gauges. *Precis. Eng.* **2020**, *62*, 113–120, doi:10.1016/j.precisioneng.2019.11.019.

85. Sánchez-Romate, X.F.; Sbarufatti, C.; Sánchez, M.; Bernasconi, A.; Scaccabarozzi, D.; Libonati, F.; Cinquemani, S.; Güemes, A.; Ureña, A. Fatigue crack growth identification in bonded joints by using carbon nanotube doped adhesive films. *Smart Mater. Struct.* **2020**, *29*, 35032, doi:10.1088/1361-665x/ab7109.

86. Ikeda, S.; Yamada, S. Magnetic particle composite materials for magnetic sensor made by fused deposition method. *2019 13th Int. Conf. Sens. Technol.* **2020**, 1–4, doi:10.1109/icst46873.2019.9047742.

87. Mora, A.; Verma, P.; Kumar, S. Electrical conductivity of CNT/polymer composites: 3D printing, measurements and modeling. *Compos. Part B Eng.* **2020**, *183*, 107600, doi:10.1016/j.compositesb.2019.107600.

88. Nicoletto, G. Efficient determination of influence factors in fatigue of additive manufactured metals. *Procedia Struct. Integr.* **2018**, *8*, 184–191, doi:10.1016/j.prostr.2017.12.020.

89. Nicoletto, G. Directional and notch effects on the fatigue behavior of as-built DMLS Ti6Al4V. *Int. J. Fatigue* **2018**, *106*, 124–131, doi:10.1016/j.ijfatigue.2017.10.004.

90. Nicoletto, G. A novel test method for the fatigue characterization of metal powder bed fused alloys. *Procedia Struct. Integr.* **2017**, *7*, 67–74, doi:10.1016/j.prostr.2017.11.062.

91. Gomez-Gras, G.; Jerez-Mesa, R.; Travieso-Rodriguez, J.A.; Lluma-Fuentes, J. Fatigue performance of fused filament fabrication PLA specimens. *Mater. Des.* **2018**, *140*, 278–285, doi:10.1016/j.matdes.2017.11.072.

174

92. Letcher, T.; Waytashek, M. Material Property Testing of 3D-Printed Specimen in PLA on an Entry-Level 3D Printer. In Proceedings of the Volume 2A: Advanced Manufacturing; American Society of Mechanical Engineers, 2014.

93. Senatov, F.S.; Niaza, K.V.; Stepashkin, A.A.; Kaloshkin, S.D. Low-cycle fatigue behavior of 3d-printed PLA-based porous scaffolds. *Compos. Part B Eng.* **2016**, *97*, 193–200, doi:10.1016/j.compositesb.2016.04.067.

94. Moore, J.P.; Williams, C.B. Fatigue properties of parts printed by PolyJet material jetting. *Rapid Prototyp. J.* **2015**, *21*, 675–685, doi:10.1108/RPJ-03-2014-0031.

95. Fischer, M.; Schöppner, V. Fatigue Behavior of FDM Parts Manufactured with Ultem 9085. *JOM* **2017**, *69*, 563–568, doi:10.1007/s11837-016-2197-2.

96. Carutasu, N.; Simion, I.; Carutasu, G. Experimental Test for Elastic and Mechanical Evaluation of ABS Plastic Used in 3D Printing. *Mater. Plast.* **2015**, *52*, 397–401.

97. Dawoud, M.; Taha, I.; Ebeid, S.J. Mechanical behaviour of ABS: An experimental study using FDM and injection moulding techniques. *J. Manuf. Process.* **2016**, *21*, 39–45, doi:10.1016/j.jmapro.2015.11.002.

98. Torrado, A.R.; Shemelya, C.M.; English, J.D.; Lin, Y.; Wicker, R.B.; Roberson, D.A. Characterizing the effect of additives to ABS on the mechanical property anisotropy of specimens fabricated by material extrusion 3D printing. *Addit. Manuf.* **2015**, *6*, 16–29, doi:10.1016/j.addma.2015.02.001.

99. Ziemian, C.; Sharma, M.; Ziemi, S. Anisotropic Mechanical Properties of ABS Parts Fabricated by Fused Deposition Modelling. In *Mechanical Engineering*; InTech, 2012.

100. Hart, K.R.; Wetzel, E.D. Fracture behavior of additively manufactured acrylonitrile butadiene styrene (ABS) materials. *Eng. Fract. Mech.* **2017**, *177*, 1–13, doi:10.1016/j.engfracmech.2017.03.028.

101. Gribbins, C., Steinhauer, H.M. Experimental analysis on an additively manufactured ABS living hinge. *25th Annu. Int. Solid Free. Fabr. Symp. Austin* **2014**.

102. Ziemian, C.W.; Ziemian, R.D.; Haile, K.V. Characterization of stiffness degradation caused by fatigue damage of additive manufactured parts. *Mater. Des.* **2016**, *109*, 209–218, doi:10.1016/j.matdes.2016.07.080.

103. Padzi, M.M.; Bazin, M.M.; Muhamad, W.M.W. Fatigue Characteristics of 3D Printed Acrylonitrile Butadiene Styrene (ABS). *IOP Conf. Ser. Mater. Sci. Eng.* **2017**, *269*, 012060, doi:10.1088/1757-899X/269/1/012060.

References

104. Lee, J.; Huang, A. Fatigue analysis of FDM materials. *Rapid Prototyp. J.* **2013**, *19*, 291–299, doi:10.1108/13552541311323290.

105. Zhang, H.; Cai, L.; Golub, M.; Zhang, Y.; Yang, X.; Schlarman, K.; Zhang, J. Tensile, Creep, and Fatigue Behaviors of 3D-Printed Acrylonitrile Butadiene Styrene. *J. Mater. Eng. Perform.* **2018**, *27*, 57–62, doi:10.1007/s11665-017-2961-7.

106. Bai, J.; Yuan, S.; Shen, F.; Zhang, B.; Chua, C.K.; Zhou, K.; Wei, J. Toughening of polyamide 11 with carbon nanotubes for additive manufacturing. *Virtual Phys. Prototyp.* **2017**, *12*, 235–240, doi:10.1080/17452759.2017.1315146.

107. Frascio, M.; Marques, E.A. de S.; Carbas, R.J.C.; da Silva, L.F.M.; Monti, M.; Avalle, M. Review of Tailoring Methods for Joints with Additively Manufactured Adherends and Adhesives. *Materials (Basel).* **2020**, *13*, 3949, doi:10.3390/ma13183949.

108. Monzón, M.D.; Ortega, Z.; Martínez, A.; Ortega, F. Standardization in additive manufacturing: activities carried out by international organizations and projects. *Int. J. Adv. Manuf. Technol.* **2014**, *76*, 1111–1121, doi:10.1007/s00170-014-6334-1.

109. Thompson, M.K.; Moroni, G.; Vaneker, T.; Fadel, G.; Campbell, R.I.; Gibson, I.; Bernard, A.; Schulz, J.; Graf, P.; Ahuja, B.; et al. Design for Additive Manufacturing: Trends, opportunities, considerations, and constraints. *CIRP Ann. - Manuf. Technol.* **2016**, *65*, 737–760, doi:10.1016/j.cirp.2016.05.004.

110. Huang, J.; Chen, Q.; Jiang, H.; Zou, B.; Li, L.; Liu, J.; Yu, H. A survey of design methods for material extrusion polymer 3D printing. *Virtual Phys. Prototyp.* **2020**, *0*, 1–15, doi:10.1080/17452759.2019.1708027.

111. Ulu, E.; Gecer Ulu, N.; Hsiao, W.; Nelaturi, S. Manufacturability Oriented Model Correction and Build Direction Optimization for Additive Manufacturing. *J. Mech. Des.* **2020**, *142*, doi:10.1115/1.4045107.

112. Popescu, D.; Zapciu, A.; Amza, C.; Baciu, F.; Marinescu, R. FDM process parameters influence over the mechanical properties of polymer specimens: A review. *Polym. Test.* **2018**, *69*, 157–166, doi:10.1016/j.polymertesting.2018.05.020.

113. Polenz, S.; Oettel, M.; López, E.; Leyens, C. Hybrid Process Chain from Die Casting and Additive Manufacturing. *Light. Des. Worldw.* **2019**, *12*, 44–49, doi:10.1007/s41777-019-0021-8.

114. Espalin, D.; Arcaute, K.; Anchondo, E.; Adame, A.; Medina, F.; Winker, R.; Hoppe, T.; Wicker, R. Analysis of bonding methods for FDM-manufactured parts. *21st Annu. Int. Solid Free. Fabr. Symp.*

176

- An Addit. Manuf. Conf. SFF 2010 **2010**, 37–47.

115. Arenas, J.M.; Alía, C.; Blaya, F.; Sanz, A. Multi-criteria selection of structural adhesives to bond ABS parts obtained by rapid prototyping. *Int. J. Adhes. Adhes.* **2012**, *33*, 67–74, doi:10.1016/j.ijadhadh.2011.11.005.

116. Falck, R.; Goushegir, S.M.; dos Santos, J.F.; Amancio-Filho, S.T. AddJoining: A novel additive manufacturing approach for layered metal-polymer hybrid structures. *Mater. Lett.* **2018**, *217*, 211–214, doi:10.1016/j.matlet.2018.01.021.

117. Richter, A.; Kessing, D.; Fischer, F.; Pelzer, L.; Dilger, K. Print-on strategies to bond injection molded parts with structures produced by fused-deposition-modeling. *Proc. Int. Conf. Eng. Des. ICED* **2019**, *2019-Augus*, 819–828, doi:10.1017/dsi.2019.86.

118. Pei, E.; Loh, G.H. Technological considerations for 4D printing: an overview. *Prog. Addit. Manuf.* **2018**, *3*, 95–107, doi:10.1007/s40964-018-0047-1.

119. da Silva, L.F.M.; Marques, E.A.S.; Campilho, R.D.S.G. Design Rules and Methods to Improve Joint Strength. In *Handbook of Adhesion Technology*; da Silva, L.F.M., Öchsner, A., Adams, R.D., Eds.; Springer International Publishing: Cham, 2018; pp. 773–810 ISBN 978-3-319-55411-2.

120. Tong, L.; Luo, Q. Analytical Approach to Joint Design. In *Handbook of Adhesion Technology*; da Silva, L.F.M., Öchsner, A., Adams, R.D., Eds.; Springer Berlin Heidelberg: Berlin, Heidelberg, 2011; pp. 597–627 ISBN 978-3-642-01169-6.

121. da Silva, L.F.M.; Rodrigues, T.N.S.S.; Figueiredo, M.A. V; de Moura, M.F.S.F.; Chousal, J.A.G. Effect of Adhesive Type and Thickness on the Lap Shear Strength. *J. Adhes.* **2006**, *82*, 1091–1115, doi:10.1080/00218460600948511.

122. Marques, J.B.; Barbosa, A.Q.; da Silva, C.I.; Carbas, R.J.C.; da Silva, L.F.M. An overview of manufacturing functionally graded adhesives–Challenges and prospects. *J. Adhes.* **2019**, *0*, 1–35, doi:10.1080/00218464.2019.1646647.

123. Shang, X.; Marques, E.A.S.; Machado, J.J.M.; Carbas, R.J.C.; Jiang, D.; da Silva, L.F.M. Review on techniques to improve the strength of adhesive joints with composite adherends. *Compos. Part B Eng.* **2019**, *177*, 107363, doi:10.1016/j.compositesb.2019.107363.

124. Boss, J.N.; Ganesh, V.K.; Lim, C.T. Modulus grading versus geometrical grading of composite adherends in single-lap bonded joints. *Compos. Struct.* **2003**, *62*, 113–121, doi:10.1016/S0263-8223(03)00097-7.

125. Khan, M.A.; Kumar, S.; Reddy, J.N. Material-tailored adhesively bonded multilayers: A theoretical

177

analysis. *Int. J. Mech. Sci.* **2018**, *148*, 246–262, doi:10.1016/j.ijmecsci.2018.08.017.

126. Hiller, J.; Lipson, H. Tunable digital material properties for 3D voxel printers. *Rapid Prototyp. J.* **2010**, *16*, 241–247, doi:10.1108/13552541011049252.

127. Kumar, S.; Khan, M.A. An elastic solution for adhesive stresses in multi-material cylindrical joints. *Int. J. Adhes. Adhes.* **2016**, *64*, 142–152, doi:10.1016/j.ijadhadh.2015.10.009.

128. Wang, S.; Ma, Y.; Deng, Z.; Zhang, S.; Cai, J. Effects of fused deposition modeling process parameters on tensile, dynamic mechanical properties of 3D printed polylactic acid materials. *Polym. Test.* **2020**, *86*, 106483, doi:https://doi.org/10.1016/j.polymertesting.2020.106483.

129. Loh, G.H.; Pei, E.; Harrison, D.; Monzón, M.D. An overview of functionally graded additive manufacturing. *Addit. Manuf.* **2018**, *23*, 34–44, doi:10.1016/j.addma.2018.06.023.

130. Ritchie, R.O. The conflicts between strength and toughness. *Nat. Mater.* **2011**, *10*, 817–822, doi:10.1038/nmat3115.

131. Kolednik, O.; Predan, J.; Fischer, F.D.; Fratzl, P. Bioinspired design criteria for damage-resistant materials with periodically varying microstructure. *Adv. Funct. Mater.* **2011**, *21*, 3634–3641, doi:10.1002/adfm.201100443.

132. Afferrante, L.; Carbone, G. Biomimetic surfaces with controlled direction-dependent adhesion. *J. R. Soc. Interface* **2012**, *9*, 3359–3365, doi:10.1098/rsif.2012.0452.

133. Niese, B.; Stichel, T.; Amend, P.; Urmoneit, U.; Roth, S.; Schmidt, M. Manufacturing of conductive circuits for embedding stereolithography by means of conductive adhesive and laser sintering. *Phys. Procedia* **2014**, *56*, 336–344, doi:10.1016/j.phpro.2014.08.179.

134. Nakanouchi, M.; Sato, C.; Sekiguchi, Y.; Haraga, K.; Uno, H. Development of application method for fabricating functionally graded adhesive joints by two-component acrylic adhesives with different elastic moduli. *J. Adhes.* **2019**, *95*, 529–542, doi:10.1080/00218464.2019.1583562.

135. Revelo, C.F.; Colorado, H.A. 3D printing of kaolinite clay ceramics using the Direct Ink Writing (DIW) technique. *Ceram. Int.* **2018**, *44*, 5673–5682, doi:10.1016/j.ceramint.2017.12.219.

136. Samyn, P.; Biesalski, M.; Prucker, O.; Rühe, J. Dewetting and photochemical crosslinking of adhesive pads onto lithographically patterned surfaces. *J. Appl. Polym. Sci.* **2019**, *136*, 1–13, doi:10.1002/app.47321.

137. Sarantinos, N.; Tsantzalis, S.; Ucsnik, S.; Kostopoulos, V. Review of through-the-thickness reinforced composites in joints. *Compos. Struct.* **2019**, *229*, 111404, doi:10.1016/j.compstruct.2019.111404.

References

138. Benzeggagh, M.L.; Kenane, M. Measurement of mixed-mode delamination fracture toughness of unidirectional glass/epoxy composites with mixed-mode bending apparatus. *Compos. Sci. Technol.* **1996**, *56*, 439–449, doi:10.1016/0266-3538(96)00005-X.

139. DIN EN 1465: 2009-07 Adhesives Determination of tensile lap-shear strength of bonded assemblies.

140. Jilich, M.; Frascio, M.; Avalle, M.; Zoppi, M. Development of a gripper for garment handling designed for additive manufacturing. *Proc. Inst. Mech. Eng. Part C J. Mech. Eng. Sci.* **2019**, *0*, 1–12, doi:10.1177/0954406219857763.

141. Frascio, M.; Jilich, M.; Pizzorni, M.; Monti, M.; Avalle, M.; Zoppi, M. The use of low pressure plasma surface modification for bonded joints to assembly a robotic gripper designed to be additive manufactured. *Procedia Struct. Integr.* **2019**, *24*, 204–212, doi:10.1016/j.prostr.2020.02.017.

142. Rossing, L.; Scharff, R.B.N.; Chömpff, B.; Wang, C.C.L.; Doubrovski, E.L. Bonding between silicones and thermoplastics using 3D printed mechanical interlocking. *Mater. Des.* **2020**, *186*, 108254, doi:10.1016/j.matdes.2019.108254.

143. Arikan, E.; Holtmannspötter, J.; Zimmer, F.; Hofmann, T.; Gudladt, H.J. The role of chemical surface modification for structural adhesive bonding on polymers - Washability of chemical functionalization without reducing adhesion. *Int. J. Adhes. Adhes.* **2019**, *95*, 102409, doi:10.1016/j.ijadhadh.2019.102409.

144. Rietz, U.; Lerche, D.; Hielscher, S.; Beck, U. Centrifugal Adhesion Testing Technology (CATT)- A Valuable Tool for Strength Determination. *J. Adhes. Soc. Japan* **2015**, *51*, 293–297, doi:10.11618/adhesion.51.293.

145. DIN EN 15870 Adhesives - Determination of tensile strength of butt joints. *Kleb. der Zugfestigkeit von Stumpfklebungen (ISO 6922 1987modifiziert)* 2009.

146. Standard GBT 33334 Test method for strength properties of adhesives in shear by tension.

147. ASTM D5868 - 01(2014) Bonding, Standard Test Method for Lap Shear Adhesion for Fiber Reinforced Plastic (FRP).

148. ASTM D3163 - 01(2014) Standard Test Method for Determining Strength of Adhesively Bonded Rigid Plastic Lap-Shear Joints in Shear by Tension Loading.

149. ASTM D1002 - 10(2019) Standard Test Method for Apparent Shear Strength of Single-Lap-Joint Adhesively Bonded Metal Specimens by Tension Loading (Metal-to-Metal).

150. Frascio, M.; Bergonzi, L.; Jilich, M.; Moroni, F.; Avalle, M.; Pirondi, A.; Monti, M.; Vettori, M.

179

Additive manufacturing process parameter influence on mechanical strength of adhesive joints, preliminary activities. *Acta Polytech. CTU Proc.* **2019**, *25*, 41–47, doi:10.14311/APP.2091.25.0041.

151. Turner, B.N.; Strong, R.; Gold, S.A. A review of melt extrusion additive manufacturing processes: I. Process design and modeling. *Rapid Prototyp. J.* **2014**, *20*, 192–204, doi:10.1108/RPJ-01-2013-0012.

152. Alsoufi, M.S.; Elsayed, A.E. Surface Roughness Quality and Dimensional Accuracy—A Comprehensive Analysis of 100% Infill Printed Parts Fabricated by a Personal/Desktop Cost-Effective FDM 3D Printer. *Mater. Sci. Appl.* **2018**, *09*, 11–40, doi:10.4236/msa.2018.91002.

153. Turner, B.N.; Gold, S.A. A review of melt extrusion additive manufacturing processes: II. Materials, dimensional accuracy, and surface roughness. *Rapid Prototyp. J.* **2015**, *21*, 250–261, doi:10.1108/RPJ-02-2013-0017.

154. ASTM D3165-07(2014) Standard Test Method for Strength Properties of Adhesives in Shear by Tension Loading of Single-Lap-Joint Laminated Assemblies.

155. ASTM D2094 - 00(2014) Standard Practice for Preparation of Bar and Rod Specimens for Adhesion Tests.

156. EN 205:2003 Adhesives - Wood adhesives for non-structural applications - Determination of tensile shear strength of lap joints.

157. Le, T.-H.-L.; Jilich, M.; Landini, A.; Zoppi, M.; Zlatanov, D.; Molfino, R. On the Development of a Specialized Flexible Gripper for Garment Handling. *J. Autom. Control Eng.* **2013**, *1*, 255–259, doi:10.12720/joace.1.3.255-259.

158. Le, L.; Zoppi, M.; Jilich, M.; Bo, H.; Zlatanov, D.; Molfino, R. Application of a Biphasic Actuator in the Design of a Robot Gripper for Garment Handling. In Proceedings of the Volume 5B: 38th Mechanisms and Robotics Conference; American Society of Mechanical Engineers, 2014.

159. Adam, G.A.O.; Zimmer, D. Design for Additive Manufacturing—Element transitions and aggregated structures. *CIRP J. Manuf. Sci. Technol.* **2014**, *7*, 20–28, doi:10.1016/j.cirpj.2013.10.001.

160. Maloch, J.; Hnátková, E.; Žaludek, M.; Krátký, P. Effect of Processing Parameters on Mechanical Properties of 3D Printed Samples. *Mater. Sci. Forum* **2018**, *919*, 230–235, doi:10.4028/www.scientific.net/MSF.919.230.

161. Attoye, S.; Malekipour, E.; El-Mounayri, H. Correlation Between Process Parameters and Mechanical Properties in Parts Printed by the Fused Deposition Modeling Process. In; 2019; pp. 35–41.

References

162. Lee, B.H.; Abdullah, J.; Khan, Z.A. Optimization of rapid prototyping parameters for production of flexible ABS object. *J. Mater. Process. Technol.* **2005**, *169*, 54–61, doi:10.1016/j.jmatprotec.2005.02.259.

163. Casavola, C.; Cazzato, A.; Moramarco, V.; Renna, G. Mechanical behaviour of ABS-Fused Filament Fabrication compounds under impact tensile loadings. *Materials (Basel).* **2019**, *12*, doi:10.3390/ma12081295.

164. Mallik, P.K. *Fiber-Reinforced Composites: Materials, Manufacturing, and Design*; 2008; ISBN 0849342058, 9780849342059.

165. Frascio, M.; Avalle, M.; Monti, M. Fatigue strength of plastics components made in additive manufacturing: First experimental results. In Proceedings of the Procedia Structural Integrity; 2018; Vol. 12, pp. 32–43.

166. Bergonzi, L.; Pirondi, A.; Moroni, F.; Frascio, M.; Avalle, M. A study on Fused Filament Fabrication (FFF) parameters as bonded joint design factors. *J. Adhes.* **2021**.

167. Butt, J.; Bhaskar, R. Investigating the effects of annealing on the mechanical properties of FFF-printed thermoplastics. *J. Manuf. Mater. Process.* **2020**, *4*, 1–20, doi:10.3390/jmmp4020038.

168. Kuznetsov, V.E.; Solonin, A.N.; Tavitov, A.; Urzhumtsev, O.; Vakulik, A. Increasing strength of FFF three-dimensional printed parts by influencing on temperature-related parameters of the process. *Rapid Prototyp. J.* **2020**, *26*, 107–121, doi:10.1108/RPJ-01-2019-0017.

169. Kandananond, K. Optimization of fused filament fabrication system by response surface method. *Int. J. Metrol. Qual. Eng.* **2020**, *11*, 4, doi:10.1051/ijmqe/2020002.

170. Montgomery, D.C. *Design and Analysis of Experiments, 8th Edition*; John Wiley & Sons, Incorporated, 2012; ISBN 9781118214718.

171. Kubiak, K.J.; Wilson, M.C.T.; Mathia, T.G.; Carval, P. Wettability versus roughness of engineering surfaces. *Wear* **2011**, *271*, 523–528, doi:10.1016/j.wear.2010.03.029.

172. Vaes, D.; Coppens, M.; Goderis, B.; Zoetelief, W.; Van Puyvelde, P. Assessment of Crystallinity Development during Fused Filament Fabrication through Fast Scanning Chip Calorimetry. *Appl. Sci.* **2019**, *9*, 2676, doi:10.3390/app9132676.

173. Srinivas, V.; van Hooy-Corstjens, C.S.J.; Harings, J.A.W. Correlating molecular and crystallization dynamics to macroscopic fusion and thermodynamic stability in fused deposition modeling. *Polymer (Guildf).* **2018**, *142*, 348–355, doi:10.1016/j.polymer.2018.03.063.

174. Antony, J.; Kaye, M. *Experimental Quality*; Springer US: Boston, MA, 2000; ISBN 978-1-4613-7415-

181

2.

175. Taguchi, G. *Taguchi methods : orthogonal arrays and linear graphs. Tools for quality engineering*; American Supplier Institute: Dearborn, Michigan, 1987; ISBN 0-941243-01-X.

176. Antony, J.; Kaye, M. *Experimental quality: a strategic approach to achieve and improve quality*; Springer Science & Business Media, 2012;

177. Frascati, J. Effects Of Position, Orientation, And Infiltrating Material On Three Dimensional Printing Models.; 2007.

178. Gajdo\vs, I.; Slota, J. Influence of printing conditions on structure in FDM prototypes. *Teh. Vjesn. Gaz.* **2013**, *20*, 231–236.

179. Ahn, S.; Montero, M.; Odell, D.; Roundy, S.; Wright, P.K. Anisotropic material properties of fused deposition modeling ABS. *Rapid Prototyp. J.* **2002**, *8*, 248–257, doi:10.1108/13552540210441166.

180. Chaves, F.J.P.; da Silva, L.F.M.; de Moura, M.F.S.F.; Dillard, D.A.; Esteves, V.H.C. Fracture Mechanics Tests in Adhesively Bonded Joints: A Literature Review. *J. Adhes.* **2014**, *90*, 955–992, doi:10.1080/00218464.2013.859075.

181. de Moura, M.F.S.F.; Campilho, R.D.S.G.; Gonçalves, J.P.M. Crack equivalent concept applied to the fracture characterization of bonded joints under pure mode I loading. *Compos. Sci. Technol.* **2008**, *68*, 2224–2230, doi:10.1016/j.compscitech.2008.04.003.

182. de Moura, M.F.S.F.; Morais, J.J.L.; Dourado, N. A new data reduction scheme for mode I wood fracture characterization using the double cantilever beam test. *Eng. Fract. Mech.* **2008**, *75*, 3852–3865, doi:10.1016/j.engfracmech.2008.02.006.

183. Frascio, M.; Mandolfino, C.; Moroni, F.; Jilich, M.; Lagazzo, A.; Pizzorni, M.; Bergonzi, L.; Morano, C.; Alfano, M.; Avalle, M. Appraisal of surface preparation in adhesive bonding of additive manufactured substrates. *Int. J. Adhes. Adhes.* **2021**, 102802, doi:10.1016/j.ijadhadh.2020.102802.

184. Packham, D.E. Surface energy , surface topography and adhesion. *Int. J. Adhes. Adhes.* **2003**, *23*, 437–448, doi:10.1016/S0143-7496(03)00068-X.

185. Spaggiari, A.; Dragoni, E. Effect of mechanical surface treatment on the static strength of adhesive lap joints. *J. Adhes.* **2013**, *89*, 677–696, doi:10.1080/00218464.2012.751526.

186. Liston, E.M. Plasma treatment for improved bonding: A review. *J. Adhes.* **1989**, *30*, 199–218, doi:10.1080/00218468908048206.

187. Wolf, R.; Sparavigna, A.C. Role of Plasma Surface Treatments on Wetting and Adhesion. *Engineering* **2010**, *02*, 397–402, doi:10.4236/eng.2010.26052.

188. Ku, J.H.; Jung, I.H.; Rhee, K.Y.; Park, S.J. Atmospheric pressure plasma treatment of polypropylene to improve the bonding strength of polypropylene/aluminum composites. *Compos. Part B Eng.* **2013**, *45*, 1282–1287, doi:10.1016/j.compositesb.2012.06.016.

189. Abenojar, J.; Torregrosa-coque, R.; Martinez, M.A.; Martin-martinez, J.M. Surface modifications of polycarbonate (PC) and acrylonitrile butadiene styrene (ABS) copolymer by treatment with atmospheric plasma. *Surf. Coat. Technol.* **2009**, *203*, 2173–2180, doi:10.1016/j.surfcoat.2009.01.037.

190. Noeske, M.; Degenhardt, J.; Strudthoff, S.; Lommatzsch, U. Plasma jet treatment of five polymers at atmospheric pressure: Surface modifications and the relevance for adhesion. *Int. J. Adhes. Adhes.* **2004**, *24*, 171–177, doi:10.1016/j.ijadhadh.2003.09.006.

191. Mandolfino, C.; Lertora, E.; Gambaro, C. Influence of cold plasma treatment parameters on the mechanical properties of polyamide homogeneous bonded joints. *Surf. Coatings Technol.* **2017**, *313*, 222–229, doi:10.1016/j.surfcoat.2017.01.071.

192. Chlupova, S.; Kelar, J.; Slavícek, P. Changing the surface properties of ABS plastic by plasma. *22nd Symp. Phys. Switch. Arc* **2017**, *2017-Septe*, 32–35, doi:10.14311/ppt.2017.1.32.

193. Bagiatis, V.; Critchlow, G.W.; Price, D.; Wang, S. The effect of atmospheric pressure plasma treatment (APPT) on the adhesive bonding of poly(methyl methacrylate) (PMMA)-to-glass using a polydimethylsiloxane (PDMS)-based adhesive. *Int. J. Adhes. Adhes.* **2019**, *95*, 102405, doi:10.1016/j.ijadhadh.2019.102405.

194. Kinloch, A.J. *Adhesion and Adhesives*; Springer Netherlands: Dordrecht, 1987; ISBN 978-90-481-4003-9.

195. David, R.; Neumann, A.W. Contact Angle Hysteresis on Randomly Rough Surfaces: A Computational Study. *Langmuir* **2013**, *29*, 4551–4558, doi:10.1021/la400294t.

196. Meiron, T.S.; Marmur, A.; Saguy, I.S. Contact angle measurement on rough surfaces. *J. Colloid Interface Sci.* **2004**, *274*, 637–644, doi:10.1016/j.jcis.2004.02.036.

197. Frascio, M.; Moroni, F.; Marques, E.; Carbas, R.J.C.; dos Reis, M.Q.; Monti, M.; Avalle, M.; da Silva, L.F.M. Feasibility study on hybrid weld-bonded joints using additive manufacturing and conductive thermoplastic filament. *J. Adv. Join. Process.* **2021**, 1.

198. Han, D.; Lee, H. Recent advances in multi-material additive manufacturing: methods and applications. *Curr. Opin. Chem. Eng.* **2020**, *28*, 158–166, doi:10.1016/j.coche.2020.03.004.

199. Tan, L.J.; Zhu, W.; Zhou, K. Recent Progress on Polymer Materials for Additive Manufacturing. *Adv.*

References

Funct. Mater. **2020**, *30*, 2003062, doi:10.1002/adfm.202003062.

200.   Arif, M.F.; Alhashmi, H.; Varadarajan, K.M.; Koo, J.H.; Hart, A.J.; Kumar, S. Multifunctional performance of carbon nanotubes and graphene nanoplatelets reinforced PEEK composites enabled via FFF additive manufacturing. *Compos. Part B Eng.* **2020**, *184*, 107625, doi:10.1016/j.compositesb.2019.107625.

201.   van de Werken, N.; Tekinalp, H.; Khanbolouki, P.; Ozcan, S.; Williams, A.; Tehrani, M. Additively manufactured carbon fiber-reinforced composites: State of the art and perspective. *Addit. Manuf.* **2020**, *31*, 100962, doi:10.1016/j.addma.2019.100962.

202.   Ghomi, E.R.; Khosravi, F.; Neisiany, R.E.; Singh, S.; Ramakrishna, S. Future of Additive Manufacturing in Healthcare. *Curr. Opin. Biomed. Eng.* **2020**, 100255, doi:10.1016/j.cobme.2020.100255.

203.   Kaur, M.; Kim, W.S. Toward a Smart Compliant Robotic Gripper Equipped with 3D-Designed Cellular Fingers. *Adv. Intell. Syst.* **2019**, *1*, 1900019, doi:10.1002/aisy.201900019.

204.   Zaharia, S.M.; Enescu, L.A.; Pop, M.A. Mechanical Performances of Lightweight Sandwich Structures Produced by Material Extrusion-Based Additive Manufacturing. *Polymers (Basel).* **2020**, *12*, 1740, doi:10.3390/polym12081740.

205.   Özen, İ.; Çava, K.; Gedikli, H.; Alver, Ü.; Aslan, M. Low-energy impact response of composite sandwich panels with thermoplastic honeycomb and reentrant cores. *Thin-Walled Struct.* **2020**, *156*, 106989, doi:10.1016/j.tws.2020.106989.

206.   Mao, Y.; Wu, L.; Yan, D.M.; Guo, J.; Chen, C.W.; Chen, B. Generating hybrid interior structure for 3D printing. *Comput. Aided Geom. Des.* **2018**, *62*, 63–72, doi:10.1016/j.cagd.2018.03.015.

207.   de Lima, C.R.; Paulino, G.H. Auxetic structure design using compliant mechanisms: A topology optimization approach with polygonal finite elements. *Adv. Eng. Softw.* **2019**, *129*, 69–80, doi:10.1016/j.advengsoft.2018.12.002.

208.   Ahmed, K.; Shiblee, M.N.I.; Khosla, A.; Nagahara, L.; Thundat, T.; Furukawa, H. Review—Recent Progresses in 4D Printing of Gel Materials. *J. Electrochem. Soc.* **2020**, *167*, 037563, doi:10.1149/1945-7111/ab6e60.

209.   Alfaify, A.; Saleh, M.; Abdullah, F.M.; Al-Ahmari, A.M. Design for Additive Manufacturing: A Systematic Review. *Sustainability* **2020**, *12*, 7936, doi:10.3390/su12197936.

210.   Wood, B.M. *Design and Manufacture for Multifunctionality - 5 Multifunctionality in Additive Manufacturing*; Elsevier Inc., 2016; ISBN 9780323340618.

184

211. Wang, J.; Mubarak, S.; Dhamodharan, D.; Divakaran, N.; Wu, L.; Zhang, X. Fabrication of thermoplastic functionally gradient composite parts with anisotropic thermal conductive properties based on multicomponent fused deposition modeling 3D printing. *Compos. Commun.* **2020**, *19*, 142–146, doi:10.1016/j.coco.2020.03.012.

212. Bardiya, S.; Jerald, J.; Satheeshkumar, V. Effect of process parameters on the impact strength of fused filament fabricated (FFF) polylactic acid (PLA) parts. *Mater. Today Proc.* **2020**, doi:10.1016/j.matpr.2020.08.066.

213. Kiendl, J.; Gao, C. Controlling toughness and strength of FDM 3D-printed PLA components through the raster layup. *Compos. Part B Eng.* **2020**, *180*, 107562, doi:10.1016/j.compositesb.2019.107562.

214. Ahmed, T.J.; Stavrov, D.; Bersee, H.E.N.; Beukers, A. Induction welding of thermoplastic composites—an overview. *Compos. Part A Appl. Sci. Manuf.* **2006**, *37*, 1638–1651, doi:10.1016/j.compositesa.2005.10.009.

215. Kwok, S.W.; Goh, K.H.H.; Tan, Z.D.; Tan, S.T.M.; Tjiu, W.W.; Soh, J.Y.; Ng, Z.J.G.; Chan, Y.Z.; Hui, H.K.; Goh, K.E.J. Electrically conductive filament for 3D-printed circuits and sensors. *Appl. Mater. Today* **2017**, *9*, 167–175, doi:10.1016/j.apmt.2017.07.001.

216. Flowers, P.F.; Reyes, C.; Ye, S.; Kim, M.J.; Wiley, B.J. 3D printing electronic components and circuits with conductive thermoplastic filament. *Addit. Manuf.* **2017**, *18*, 156–163, doi:10.1016/j.addma.2017.10.002.

217. Stano, G.; Di Nisio, A.; Lanzolla, A.; Percoco, G. Additive manufacturing and characterization of a load cell with embedded strain gauges. *Precis. Eng.* **2020**, *62*, 113–120, doi:10.1016/j.precisioneng.2019.11.019.

218. Brassard, D.; Dubé, M.; Tavares, J.R. Modelling resistance welding of thermoplastic composites with a nanocomposite heating element. *J. Compos. Mater.* **2020**, doi:10.1177/0021998320957055.

219. Banea, M.D.; Da Silva, L.F.M. Adhesively bonded joints in composite materials: An overview. *Proc. Inst. Mech. Eng. Part L J. Mater. Des. Appl.* **2009**, *223*, 1–18, doi:10.1243/14644207JMDA219.

220. Braga, D.F.O.; De Sousa, L.M.C.; Infante, V.; Da Silva, L.F.M.; Moreira, P.M.G.P. Aluminium friction-stir weld-bonded joints. *J. Adhes.* **2016**, *92*, 665–678, doi:10.1080/00218464.2015.1085860.

221. Gordon, I.R.F. III. An essay on the cohesion of fluids. *Philos. Trans. R. Soc. London* **1805**, *95*, 65–87, doi:10.1098/rstl.1805.0005.

222. Owens, D.K.; Wendt, R.C. Estimation of the surface free energy of polymers. *J. Appl. Polym. Sci.* **1969**, *13*, 1741–1747, doi:10.1002/app.1969.070130815.

References

223. Dantas, M.A.; Carbas, R.J.; Marques, E.A.S.; Kushner, D.; Silva, L.F.M. Flexible tubular metal-polymer adhesive joints under torsion loading. *Int. J. Adhes. Adhes.* **2021**, 104–125.

224. Jordá-Vilaplana, A.; Fombuena, V.; García-García, D.; Samper, M.D.; Sánchez-Nácher, L. Surface modification of polylactic acid (PLA) by air atmospheric plasma treatment. *Eur. Polym. J.* **2014**, *58*, 23–33, doi:10.1016/j.eurpolymj.2014.06.002.

225. Hou, M.; Ye, L.; Mai, Y.W. An Experimental Study of Resistance Welding of Carbon Fibre Fabric Reinforced Polyetherimide (CF Fabric/PEI) Composite Material. *Appl. Compos. Mater.* **1999**, *6*, 35–49, doi:10.1023/A:1008879402267.

226. Vanaei, H.R.; Shirinbayan, M.; Costa, S.F.; Duarte, F.M.; Covas, J.A.; Deligant, M.; Khelladi, S.; Tcharkhtchi, A. Experimental study of PLA thermal behavior during fused filament fabrication. *J. Appl. Polym. Sci.* **2021**, *138*, 1–7, doi:10.1002/app.49747.

227. Rane, A. V.; Kanny, K.; Mathew, A.; Mohan, T.P.; Thomas, S. Comparative Analysis of Processing Techniques' Effect on the Strength of Carbon Black (N220)-Filled Poly (Lactic Acid) Composites. *Strength Mater.* **2019**, *51*, 476–489, doi:10.1007/s11223-019-00093-6.

228. Kolisnyk, R.; Korab, M.; Iurzhenko, M.; Masiuchok, O.; Shadrin, A.; Mamunya, Y.; Pruvost, S.; Demchenko, V. Conductive Polymer Nanocomposites for Novel Heating Elements. In; 2019; pp. 215–224.

229. Spoerk, M.; Arbeiter, F.; Cajner, H.; Sapkota, J.; Holzer, C. Parametric optimization of intra- and inter-layer strengths in parts produced by extrusion-based additive manufacturing of poly(lactic acid). *J. Appl. Polym. Sci.* **2017**, *134*, 45401, doi:10.1002/app.45401.

230. Khan, A.S.; Ali, A.; Hussain, G.; Ilyas, M. An experimental study on interfacial fracture toughness of 3-D printed ABS/CF-PLA composite under mode I, II, and mixed-mode loading. *J. Thermoplast. Compos. Mater.* **2019**, 089270571987486, doi:10.1177/0892705719874860.

231. Moroni, F.; Carboni, M.; Pirondi, A. Cohesive zone modelling of 6022-t4 aluminium alloy usmwbonded hybrid joints quasi-static failure. In Proceedings of the Proc. 18th European Conference on Fracture (ECF18); 2010; pp. 1–8.

232. Croccolo, D.; De Agostinis, M.; Olmi, G. Experimental characterization and analytical modelling of the mechanical behaviour of fused deposition processed parts made of ABS-M30. *Comput. Mater. Sci.* **2013**, *79*, 506–518, doi:10.1016/j.commatsci.2013.06.041.